

Surface-sensitive magnetic imaging of
polycrystalline and epitaxial ultrathin cobalt
films with a perpendicular magnetic anisotropy

Dissertation
zur Erlangung des Doktorgrades
an der Fakultät für Mathematik, Informatik und Naturwissenschaften
Fachbereich Physik
der Universität Hamburg

vorgelegt von
Susanne Kuhrau

Hamburg
2019

Gutachter/innen der Dissertation:

Prof. Dr. Hans Peter Oepen
Universität Hamburg

Prof. Dr. Ralf Röhlsberger
Universität Hamburg

Zusammensetzung der Prüfungskommission:

Prof. Dr. Hans Peter Oepen
Universität Hamburg

Prof. Dr. Ralf Röhlsberger
Universität Hamburg

Prof. Dr. Caren Hagner
Universität Hamburg

Prof. Dr. Robert Blick
Universität Hamburg

Prof. Dr. Michael Thorwart
Universität Hamburg

Vorsitzende/r der Prüfungskommission:

Prof. Dr. Caren Hagner

Datum der Disputation:

24.09.2019

Vorsitzender Fach-Promotionsausschusses PHYSIK:

Prof. Dr. Michael Potthoff

Leiter des Fachbereiches PHYSIK:

Prof Dr. Wolfgang Hansen

Dekan der Fakultät MIN:

Prof. Dr. Heinrich Graener

Abstract

This PhD thesis presents a study on magnetic domains and domain walls in cobalt-based thin film systems, carried out via scanning electron microscopy with polarization analysis (SEMPA). The first part addresses the process of taking a spin detector that uses an electrostatic beam deflector—and thus is sensitive to the perpendicular component of the magnetization—back into operation, and optimizing the performance of the corresponding SEMPA setup. Minimizing disturbances like mechanical vibrations and electrical noise resulted in a spatial resolution of $2\sigma = (16.2 \pm 0.6)$ nm at a primary beam current of 3 nA. In the following the design of a novel spin detector, customized for this setup, is presented. It is based on low-energy electron diffraction at a monolayer (ML) of gold on an iridium (001) surface and promises an increased sensitivity. Besides modeling the detector via computer-aided-design (CAD) software, also the electron trajectories of the electrons have been simulated and the corresponding potentials of the electrodes have been derived.

The second part of this thesis starts with the experimental investigation of domains and domain walls in an epitaxial cobalt film of varied thickness, grown in-situ on a Pt(111) single crystal. The onset of ferromagnetism is observed at a cobalt thickness of 1.5 ML. Up to a thickness of about 7 ML, the magnetization points perpendicular to the film plane; at higher thicknesses the spin-reorientation transition sets in and the magnetization changes into the film plane. The investigation of the domain walls at 7 ML Co/Pt(111) reveals an exclusive Néel-character and that all walls show a fixed sense of rotation. This observation is ascribed to the strong influence of the Dzyaloshinskii-Moriya interaction present in this system, which is further analyzed based on a domain-size model. Finally, the influence of a non-magnetic cap layer on the magnetic contrast observed in SEMPA is studied on polycrystalline (Pt/Co/Ir) double layers. The samples are prepared ex situ via sputter deposition and are terminated with a Pt-cap layer that is prepared as a wedge with thicknesses ranging from 0 to 2 nm. An energy-dispersive X-ray (EDX) analysis revealed that Pt-cap layers with a thickness above 1.1 nm protect the underlying Co film from oxidation. At this cap-layer thickness a magnetic contrast that is equal to 25 % of the one of a clean uncapped Co film is found which allows the direct investigation of these systems via SEMPA.

Zusammenfassung

Im Rahmen dieser Doktorarbeit werden magnetische Domänenstrukturen in kobaltbasierten Dünnschichtsystemen mittels Rasterelektronenmikroskopie mit Polarisationsanalyse (SEMPA) untersucht. Der erste Teil der Arbeit beschäftigt sich mit der Wiederinbetriebnahme eines Spindetektors, der durch die Verwendung eines Strahlumlenkers auf die senkrechte Magnetisierungskomponente empfindlich gemacht wurde, sowie mit der Optimierung des zugehörigen SEMPA Aufbaus. Durch die Minimierung von elektrischen Störeinflüssen sowie von mechanischen Schwingungen wurde bei einem Primärstrahlstrom von 3 nA eine Ortsauflösung von $2\sigma = (16,2 \pm 0,6)$ nm erreicht. Zudem wird ein neuartiger, für diesen Aufbau zugeschnittener Spindetektor vorgestellt, der auf der Beugung niederenergetischer Elektronen an einer Gold-Monolage auf der (001) Oberfläche eines Iridium-Einkristalls beruht. Neben der Erstellung der technischen Zeichnungen für den Detektorentwurf wurden die Flugbahnen der Elektronen simuliert und daraus die optimalen Elektrodenpotentiale bestimmt.

Im zweiten Teil dieser Arbeit wird eine experimentelle Untersuchung der schicht-dickenabhängigen Eigenschaften der Domänen und Domänenwände in einem Kobaltfilm dargestellt, welcher in-situ epitaktisch auf einer Pt(111)-Oberfläche aufgewachsen wurde. Bei einer Co-Schichtdicke von 1,5 Monolagen (ML) wurde das Einsetzen der ferromagnetischen Ordnung beobachtet. Die Magnetisierung weist bis zu einer Schichtdicke von etwa 7 ML eine Orientierung senkrecht zur Filmebene auf, oberhalb setzt der Spinreorientierungsübergang in die Ebene ein. Eine genauere Untersuchung der Domänenwände des 7 ML Co/Pt(111) Systems weist flächendeckend Néel Wände auf, die alle denselben Drehsinn der Magnetisierungskomponente in der Ebene zeigen. Diese Beobachtung wird auf den starken Einfluss der Dzyaloshinskii-Moriya Wechselwirkung in diesem System zurückgeführt, welche anschließend mit Hilfe eines Domänengrößenmodells analysiert wird. Abschließend wurde anhand von polykristallinen (Pt/Co/Ir)-Doppellagen der Einfluss einer nicht magnetischen Deckschicht auf den in SEMPA beobachtbaren magnetischen Kontrast untersucht. Zu diesem Zweck wurde die oberste Pt-Schicht als Keil mit einer Dicke von 0 bis 2 nm präpariert. Mittels energiedispersiver Röntgenanalyse konnte gezeigt werden, dass ab einer Pt-Schichtdicke von 1,1 nm die darunter liegende Co Schicht effektiv vor Oxidation geschützt ist. Diese Deckschichtdicke erlaubt es 25 % des magnetischen Kontrastes eines sauberen, nichtabgedeckten Co Films zu erhalten, und ermöglicht damit erstmals auch die direkte Untersuchung solcher Systeme mittels SEMPA.

Contents

1	Motivation	1
2	Scanning electron microscopy with polarization analysis	7
2.1	Introduction to the SEMPA technique	7
2.2	Interaction of the primary electron beam with the sample	8
2.3	Spin polarization of the secondary electrons	10
2.4	Spin-polarized LEED detector	11
2.4.1	Spin-orbit coupling	12
2.4.2	Detection scheme	12
2.4.3	Characteristic values describing the detector performance	14
2.5	Classification among magnetic imaging techniques	14
3	Basics of Micromagnetism	19
3.1	Exchange energy	19
3.2	Magnetostatic energy	20
3.3	Magnetic anisotropy	21
3.3.1	Magnetocrystalline volume anisotropy	22
3.3.2	Interface anisotropy	22
3.3.3	Effective magnetic anisotropy	23
3.4	Dzyaloshinskii-Moriya Interaction	23
3.5	Interlayer exchange coupling	24
3.6	Magnetic domains in thin films with PMA	26
3.6.1	Origin of domains and domain walls	26
3.6.2	Bloch and Néel walls	27

4	Experimental aspects	29
4.1	Basic introduction to the in-plane SEMPA setup	29
4.1.1	Facilities for sample preparation	30
4.1.2	Detection of the in-plane magnetization	31
4.2	Specifics and performance of the out-of-plane SEMPA setup . . .	32
4.2.1	Introduction to the out-of-plane setup	33
4.2.2	Facilities for sample preparation	35
4.2.3	The transfer optics of the spin detector	38
4.2.4	Detection unit	42
4.2.5	Voltages at the channeltrons and signal processing	44
4.2.6	Preparation of the W(001) crystal	48
4.2.7	Spatial resolution	49
4.2.8	Optimizing lateral image stability and minimizing signal noise	50
4.2.9	Formation of the magnetization images	52
5	New spin-detector design based on a pseudomorphic Au mono- layer on Ir(001)	55
5.1	Preliminary considerations	56
5.2	Preparation of the Au/Ir(001) target	59
5.3	Detector design	62
5.3.1	Crystal-holder tube	63
5.3.2	Detection unit	65
5.3.3	Au evaporator	67
5.3.4	Assembly	68
5.4	Field and electron-trajectory simulations	69
5.5	Summary and Outlook	72
6	Magnetic domains and domain walls in an epitaxially grown Co/Pt(111) film	75
6.1	The need of determining the DMI of the single Co/Pt interface . .	76
6.2	Preparation of the Co wedge on Pt(111)	78
6.3	Detecting the perpendicular magnetization in an in-plane sensitive SEMPA	81
6.4	Domain size in dependence of Co thickness	82
6.5	Néel-like walls with fixed anticlockwise sense of rotation	85
6.6	Discussion of the DMI strength based on a domain-size model . .	86
6.7	Summary	95

6.8	Outlook	96
7	Cap-layer-dependent oxidation and magnetic contrast in SEMPA of ultrathin Co films	99
7.1	Ex-situ preparation via sputter deposition	100
7.1.1	Preparation techniques	100
7.1.2	Sample preparation	102
7.1.3	Calibration via X-ray reflectometry	104
7.2	Cap-layer-thickness dependent Co oxidation and its influence on the magnetic contrast	105
7.2.1	EDX analysis of the [Pt/Co/Ir] ₂ samples	105
7.2.2	Quantitative analysis of the polarization contrast	107
7.2.3	The dependence of the magnetic contrast on the Pt thickness	108
7.2.4	Tuning the interlayer coupling from ferro- to antiferromag- netic	112
7.2.5	Investigation of the Co oxidation	113
7.3	Summary	117
7.4	Outlook	118
	References	122
	Acknowledgements	143
	Publications	145
	Eidesstattliche Erklärung/ Declaration of oath	149

Motivation

"Data is the new oil"—this quote, which is accredited to the mathematician Clive Humby, has been used in the last decade various times in articles or presentations on data mining, machine learning or data storage technologies. Within the explanation of his analogy, Humby points out that, just like oil, data has to be "refined", namely analyzed, to unfold its intrinsic value. His attention-getting comparison between data and oil itself is actually misleading in some points, as for example oil is a finite resource whose quantity reduces when used— data on the other hand is inexhaustible and can even be reused infinite times. Thus, the quote resonates well with nowadays technologically empowered society. It grasps the spirit of a time in which transformative technologies like artificial intelligence, automation or predictive analytics become a part of everyday life. The huge variety of different data users, may they be industry, researchers or private persons, have one issue in common: They need storage space for their data.

This universal demand for non-volatile memory (NVM), meaning the memory device is not in need of constant power to retain the data, has triggered the evolution of digital data storage technologies over the last hundred years. Starting with punched cards in the 20th century¹, higher areal densities and read-out speeds were reached at the end of the century, e.g. by the invention of floppy disks (storage capacity 1.44 MB, IBM (1986) [2]). Back then, it was unimaginable for society that even higher areal densities will ever be needed. The quickly advancing digital revolution proved them wrong. Nowadays, most large-scale

¹The first documented usage of punched cards goes actually further back in time to the 18th century when a loom was partially operated by a paper tape with punched holes [1].

secondary storage² devices are magnetic hard disk drives (HDDs), which have storage-densities up to about 1.3 TB/in² [3]. HDDs are magnetic storage devices providing long retention times and high endurance, meaning a high number of program/erase cycles that the device can sustain, at comparatively low costs. The second class of widespread non-volatile memory devices currently in use are solid-state drives (SSDs), which are based on flash technology³. While SSDs provide higher data-access and -transfer rates, and allow for higher areal densities, they are accompanied by the disadvantage of a higher price (in the range of a factor 10 per GB in comparison to HDDs) which makes their usage uneconomical for extensive application in industry or data centers [4, 5]. Due to the high price, even in private applications it is common to find only 128 GB to 512 GB SSD units as primary hard drives [6]. While for now the cheaper HDDs are still dominating the secondary storage market in comparison to SSDs, the era of HDDs will at some point come to an end, as the superparamagnetic limit⁴ will start to restrict further miniaturization in the near future.

Research is highly motivated to explore possibilities for new data storage technologies to fulfill the desire for devices with even higher densities, higher speed, and lower power consumption. The ideas for future storage devices are manifold and include, among many others, optical storage arrays that make use of nanophotonics [7], heat-assisted magnetic recording [8], or spin-transfer-torque magnetic random access memory [9]. A comparatively new approach that is still in its infancy arises around the so-called interfacial Dzyaloshinskii-Moriya Interaction (DMI) which is an antisymmetric exchange interaction that arises due to the absence of inversion symmetry at the interface between a ferromagnetic and a non-magnetic layer [10]. This latter approach arouses great interest in the research community that investigates thin magnetic films with perpendicular magnetic anisotropy. On the one hand, in such thin magnetic films the DMI stabilizes Néel walls with a fixed sense of rotation that can be moved more effectively than Bloch walls via the spin-transfer torque (STT) effect [11], and that can be used, e.g., in a so-called racetrack memory [12]. On the other hand, the

²Secondary storage devices are often also referred to as secondary or external memory. In contrast to primary storage which holds memory for the time a computer is running (volatile memory) and is directly accessible by the central processing unit (CPU), secondary storage devices store data until erased or overwritten.

³Flash memory is based on silicon chips that can be electrically programmed/erased.

⁴Decreasing the size of the magnetic region (bit) used to store the information leads to an increased probability of uncontrolled thermally activated switching. For an appropriate long term stability as required by industry standards, a ratio of 60 between the product of anisotropy K and volume V of the bit, and the thermal energy $k_B T$ is required.

DMI can lead to topologically protected states called skyrmions [13], which are magnetic spin structures on the nanometer scale (in the order of 10 nm [14]) and move like particles [13]. To empower scientists to engineer future data storage devices (or other technologies), regardless whether they make use of magnetic, electrical or optical mechanisms, a fundamental understanding of the underlying interactions is indispensable, which requires extensive basic research.

In this thesis, special emphasis lies on scanning electron microscopy with polarization analysis (SEMPA), a surface-sensitive measurement technique that provides the possibility to image two components of the magnetization simultaneously. SEMPA is a powerful magnetic-imaging technique as it combines a spatial resolution down to 3 nm [15] with a large magnification range that allows for image sizes in the millimeter range, as well as down to the nanometer scale. Not only bulk samples but also ultrathin films can be investigated; furthermore it provides the possibility to study polycrystalline systems that have been prepared *ex situ*, e.g. via sputter deposition, as well as epitaxial samples that were grown *in situ* on single-crystal substrates. The combined investigation of both, polycrystalline and epitaxial systems, is crucial to gain a fundamental understanding of the magnetic interactions in a specific material system. The interfaces in epitaxial films are as ideal as possible and thus allow for a direct comparison to theoretical calculations. Such comparisons empower researchers not only to improve the theoretical description of magnetic systems, they also lead to an optimization of preparation methods and an understanding of the influence of preparation parameters on the magnetic behavior. For industrial applications, epitaxially grown magnetic films are uneconomical. The time-consuming preparation and the need for single crystalline substrates results in high production costs. In contrast, polycrystalline films prepared via sputter deposition allow for the fabrication of large numbers of magnetic (multilayer) samples with identical parameters at low costs. The interfaces between the sputter-deposited layers are, in contrast to epitaxial systems, non-ideal and suffer from roughening and intermixing. Obviously, the magnetic interactions present in such polycrystalline (multi)layers must vary from the corresponding epitaxial system. By studying both, epitaxial and polycrystalline films of the same materials, an overarching understanding of the physics lying behind becomes accessible. It grants the opportunity to control and manipulate specific growth parameters in a way that ensures to obtain the desired, customized magnetic behavior for various applications, such as magnetic sensors, actuators, or data storage devices.

As stated above, SEMPA is not restricted to study *in-situ* grown magnetic sur-

faces, however, ex-situ prepared magnetic films are in the need of a non-magnetic protection layer preventing oxidation at air. Closed films of these so-called cap layers usually have a thickness of several nanometers and impede the detection of the magnetic signal via SEMPA. To circumvent this issue, it is common to either coat the cap layer with a magnetic thin film to reestablish the magnetic contrast, or to remove the cap layer via ion sputtering before the measurement. Both methods alter the original sample, either by adding another interface as well as changing the magnetic volume, or by causing roughening and intermixing of the topmost layers, respectively. A new approach that allows the investigation of samples prepared ex-situ via sputter deposition without modifying the as-grown sample is thus highly desirable, as it allows for the direct comparison between epitaxial and polycrystalline samples in SEMPA.

Within this thesis, a SEMPA setup that is sensitive to the out-of-plane component of the magnetization has been brought back into operation and its working conditions have been optimized. Due to its out-of-plane sensitivity, it is predestined for the investigation of ultrathin film systems with a perpendicular magnetic anisotropy.

The structure of the thesis is given in the following: The basics of the SEMPA technique and the working principle of the used spin detector that is based on low-energy electron diffraction (LEED) will be introduced in **Chapter 2**.

The basics of micromagnetism that are needed within this thesis are laid out briefly in **Chapter 3**.

In **Chapter 4**, the experimental aspects of the two used SEMPA setups are explained. The short introduction to the features of the "in-plane SEMPA", which is designed for the simultaneous detection of both in-plane components of the magnetization, is given. In contrast, the discussion of the optimization of the working parameters and the setup itself are presented in more detail for the "out-of-plane SEMPA", which allows to detect the perpendicular as well as one in-plane component of the magnetization simultaneously.

In view of improving the future detection efficiency of the spin contrast, a new design for a Au/Ir(001)-based LEED detector for SEMPA is presented in **Chapter 5**. In contrast to the currently used W(001)-based detector, an up to four times higher figure of merit is expected and the lifetime of the Au/Ir(001) target in ultra-high vacuum is expected to equal about 6 month, while the W(001) crystal needs a heat treatment via flashing once per hour. Besides presenting the preliminary considerations used to decide on a working point, the computer aided design of the detector and the functionality of the components will be pre-

sented. Simulations of the trajectories of the electrons within the detector were used to correctly dimension the electrode potentials.

In **Chapter 6**, an investigation of the domain size and domain walls in epitaxially grown Co on Pt(111), a system known for its strong DMI, is presented. In the presented thickness range between 0 and 7 monolayers (ML) of Co, a perpendicular magnetic anisotropy is present. It is shown that at Co thicknesses as high as 7 ML still Néel walls with a fixed anticlockwise sense of rotation exist. Furthermore, a lower bound of the DMI strength present in the ideal Co/Pt(111) system is derived.

Finally, in **Chapter 7** the oxidation of ultrathin Co films in dependence of the cap-layer thickness is investigated together with the according magnetic contrast in SEMPA. The ultrathin Co films are prepared via sputter deposition and capped with a wedged, non-magnetic material—namely Pt—and the oxidation is studied via quantitative energy-dispersive X-ray spectroscopy (EDX) as well as atomic force microscopy (AFM) measurements. A cap-layer thickness that prevents the oxidation of the Co film, but at the same time still ensures a sufficiently strong magnetic contrast, will be derived.

Scanning electron microscopy with polarization analysis

In this chapter, the primarily used measurement technique, scanning electron microscopy with polarization analysis (SEMPA), will be introduced by giving a general overview of the basic setup and the functional principle. It includes a short introduction to the interaction of the primary electron beam with the sample and will then focus on secondary electrons (SE), their spin polarization and how they are used in a low-energy electron diffraction (LEED) detector to image the magnetization. Finally, the SEMPA technique will be classified in comparison with other magnetic imaging methods.

2.1 Introduction to the SEMPA technique

SEMPA is a vectorial magnetic imaging technique with a surface sensitivity of less than five monolayers [16] and thus requires an ultra-high-vacuum (UHV) environment to circumvent surface contamination. The technique provides the possibility to image two components of the magnetization simultaneously with a spatial resolution down to 3 nm [15]. It allows to investigate thin films as well as bulk samples.

A sketch of a SEMPA setup is given in Figure 2.1 and will be used to introduce the operation principle. To perform SEMPA measurements, an electron beam, shown in cyan in Figure 2.1, is generated in the column of a scanning electron microscope (SEM), usually by a field-emission cathode of the Schottky type [17]. This unpolarized primary electron (PE) beam is focused and accelerated onto a magnetic sample (purple), and scanned across its surface. Thus SE, shown in red, are emitted point by point from the latter. The spin-polarized SE are

accelerated into a spin detector where they undergo spin-dependent low-energy electron diffraction (LEED) at a W(001) crystal¹. The spin-dependent intensities of the (2,0) spots are detected via channel electron multipliers.

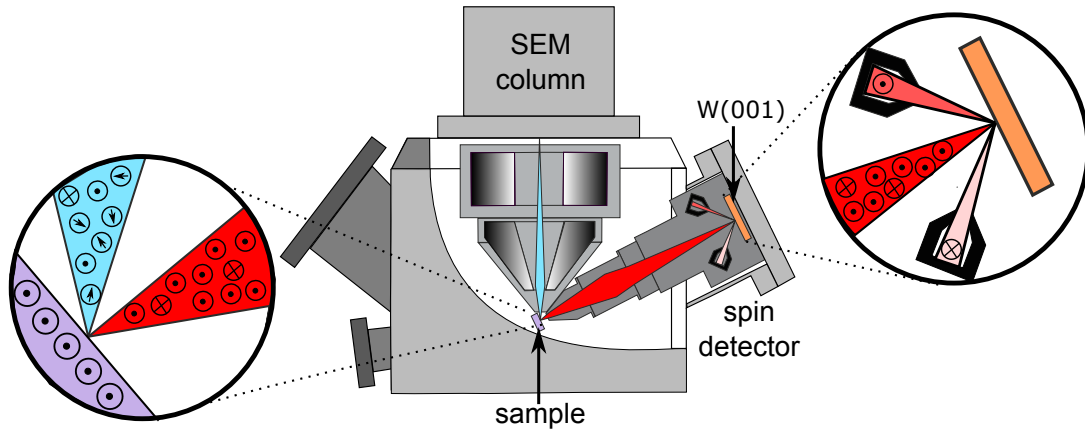


Figure 2.1: Sketch of the general operation principle of SEMPA. An SEM column generates an unpolarized primary electron beam (blue) that scans over the magnetic sample (purple). This leads to the creation of spin-polarized secondary electrons (red) which are accelerated onto a W(001) crystal to undergo LEED at normal incidence. The circles filled with a cross \otimes and a dot \odot represent the spin direction of the electrons inwards and outwards of the image plane, respectively. Thus, the magnetization of the sample lies in plane and points towards the reader. Graphic adapted from [18].

2.2 Interaction of the primary electron beam with the sample

The first key requirement for establishing a SEMPA instrument is a UHV compatible SEM. The first SEM has been built in 1937 by Manfred von Ardenne [19], though the foundations for electron microscopy have been laid six years before by M. Knoll, who built the first transmission electron microscope (TEM) [20]. In an SEM, an electron beam is focused onto the sample and scans over its surface. Due to the interaction of this primary electron (PE) beam with the atoms in the sample, various types of signals emerge, such as backscattered electrons (BSE), secondary electrons (SE), Auger electrons, cathodoluminescence or X-rays. SE result from inelastic scattering of the primary electrons with electrons of the

¹Besides the LEED detector used in our SEMPA instruments, several other types of detectors have been developed to determine the spin polarization. More information on these will be given in Section 2.4.

2.2. Interaction of the primary electron beam with the sample

atoms in the sample. They have energies below 50 eV and the secondary electron energy distribution shows a peak at low energies around 2 – 3 eV [21, 22]. As the SE originate directly from a sample area close to the sample surface, they carry the spin information of the latter, meaning they are spin polarized. BSE are electrons from the primary beam which have been reflected at the sample and may have been involved in processes of energy loss. Thus, they are unpolarized and do not provide any spin information. Though BSE are defined to have energies above 50 eV, more specifically their energy corresponds to approximately 90 % of the initial energy of the PE [23]. As SE are used for SEMPA, the following discussion will be limited to the latter.

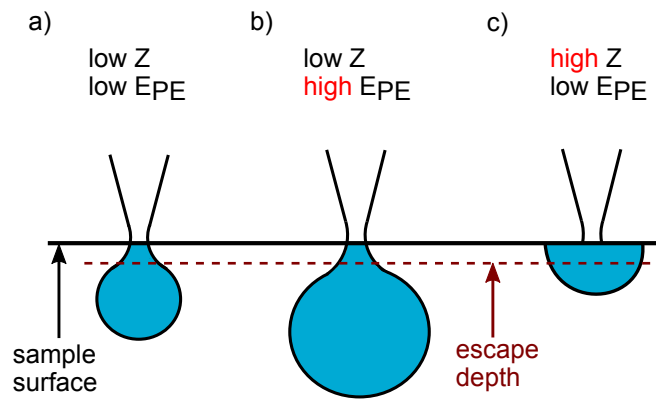


Figure 2.2: Interaction volume for different atomic numbers Z of the sample and energies E_{PE} of the primary electron beam. In low- Z materials the interaction volume takes the shape of a bulb whose depth increases with the electron energy, see a) and b). Increasing Z at constant E_{PE} leads to a less deep but laterally broader interaction volume due to increased absorption and scattering as seen in c). The escape depth, which gives the distance normal to the surface at which the probability that an electron escapes reduces to e^{-1} of its original value, is indicated as red dashed line.

The interaction of the PE with the sample takes place within the so-called interaction volume, the size of which depends on the kinetic energy of the PE beam as well as on the atomic number Z of the sample material. Figure 2.2 shows the changes in size and shape of the interaction volume with the energy of the primary electrons E_{PE} and the atomic number Z . With increasing electron energy, the interaction volume grows as the PE penetrate deeper into the sample. In contrast, at high- Z and low energies the interaction volume changes its shape from a bulb to a flat hemispheric area below the surface. Due to the increased atomic number Z more electrons are scattered or absorbed right after entering the sample. It has to be kept in mind that although SE are created in the whole

interaction volume, only those which emerge close to the surface can leave the sample. SE of the subjacent regions will be absorbed by the sample² before reaching the surface. To describe this "sampling" depth, the so-called escape depth has been defined. It gives the distance normal to the surface at which the probability, that an electron escapes, reduces to e^{-1} (36.8%) of its original value [24]. For SE in metals the escape depth is in the order of 3 – 5 nm [25, 26], but it should be kept in mind that the spin information measured in SEMPA is determined in the most upper monolayers.

2.3 Spin polarization of the secondary electrons

Walter Gerlach and Otto Stern performed in 1922 [27] a momentous experiment as they demonstrated the quantization of the spatial orientation of the angular momentum of electrons. Three years later, the quantum mechanical property spin has been postulated as an intrinsic angular momentum by Samuel Goudsmith and George Uhlenbeck [28], giving an explanation for the previous observation. The spin of a free electron relates to the magnetic moment $\vec{\mu}_s$ via

$$\vec{\mu}_s = -g_e \mu_B \frac{\vec{s}}{\hbar} \quad \text{with} \quad \mu_B := \frac{eh}{2mc}, \quad (2.1)$$

where $g_e \simeq -2.002$ is the gyromagnetic factor, also called Landé factor, of an electron, μ_B the Bohr magneton, \vec{s} the spin of the electron, h and \hbar the Planck constant and the reduced Planck constant, respectively, m the mass of the charged particle (in this case the electron mass) and c the speed of light. As can be seen from Equation 2.1, the magnetic moment of an electron is aligned antiparallel to its spin \vec{s} . The SE emitted from the sample surface thus carry the magnetic information and provide the magnetic information directly.

The spin \vec{s} is an intrinsic form of angular momentum and is described by a quantum mechanical observable³ which relates to the Pauli spin matrices $\boldsymbol{\sigma} = (\sigma_x, \sigma_y, \sigma_z)$ via $\vec{s} = (s_x, s_y, s_z) = \frac{\hbar}{2} \boldsymbol{\sigma}$. Assuming an electron beam along the z-axis, the spin states pointing along the x-axis are given by the spin function χ :

$$\chi = a |\alpha\rangle + b |\beta\rangle = a \begin{pmatrix} 1 \\ 0 \end{pmatrix} + b \begin{pmatrix} 0 \\ 1 \end{pmatrix} \quad (2.2)$$

²The SE loose kinetic energy due to elastic scattering and are thus not able to overcome the work function.

³The quantum mechanical observable \vec{s} fulfills the commutation rules and is a self-adjoint operator on a Hilbert space.

2.4. Spin-polarized LEED detector

with the eigenstates $|\alpha\rangle$ and $|\beta\rangle$ of σ_x . The spin function χ is a normalized vector in Hilbert space and describes the state of the system in which the observable \vec{s} is measured. Thus, the expectation value of the spin operator \vec{s} is given by $\langle\chi|\sigma_x|\chi\rangle$. The spin polarization is defined by the degree of alignment that the spin orientations of the particles show along a certain direction. This degree of polarization is a scalar and is defined in respect to a certain axis, e.g. the x-axis, via [29, 30]

$$P_x = \frac{\langle\chi|\sigma_x|\chi\rangle}{\langle\chi|\chi\rangle} = \frac{|a|^2 - |b|^2}{|a|^2 + |b|^2}. \quad (2.3)$$

Thus, the degree of polarization of an electron beam which is polarized along the x-axis is obtained via

$$P_x = \frac{N_{\leftarrow} - N_{\rightarrow}}{N_{\leftarrow} + N_{\rightarrow}}, \quad (2.4)$$

with N_{\rightarrow} and N_{\leftarrow} giving the number of electrons with a spin orientation parallel and antiparallel to the x-axis, respectively.

2.4 Spin-polarized LEED detector

There are three different types of detectors used in SEMPA to measure the spin polarization: Mott detectors [31], low-energy diffuse scattering (LEDS) detectors [32] and LEED detectors [33]. The Mott detector accelerates the electrons to high energies of 20 – 100 keV before scattering them at thin film targets with high Z , for example gold ($Z=79$) or thorium ($Z=90$) [34]. The usage of high energies is accompanied with the demerit of requiring voltage standoffs leading to a large detector size ($\sim 1 \text{ m}^3$). As the Mott analysis chamber usually floats on the high potential, special shielding arrangements have to be considered [35].

In a LEDS detector electrons of low energy ($\sim 150 \text{ eV}$) undergo diffuse scattering from a high Z evaporated polycrystalline film [36]. This technique allows a handy design concerning the detector size, minimizing it to the order of magnitude of a fist. Due to the diffuse scattering, the signal scattered into a particular direction is weak. The detection issue resulting from this small signal is circumvented by providing a detector with a large angular acceptance.

The LEED detector is based on the diffraction of low energetic electrons at a single crystal. Until now, only a LEED detector based on diffraction at a W(001) crystal has been reported. In our SEMPA instruments, such LEED detectors are used to analyze the spin polarization of the SE emitted from the sample. Thus, a more detailed introduction to the concept of a LEED detector will be given in the following.

2.4.1 Spin-orbit coupling

All of the above-mentioned detector types exploit the spin-orbit interaction of high- Z materials as a way to study spin polarization⁴. The spin-polarized electron moves towards the target, thus flying into the electric field of the atomic nuclei. In the rest frame of the electron, the electric field is experienced by the electron as a magnetic field \vec{B} affecting the spin. Assuming that the electron movement takes place in a central field, the potential energy of the electron may be denoted as $U(r)$ and the energy resulting from the spin magnetic moment and the magnetic field is given by [29]

$$V_{\text{SOC}} = -\vec{\mu}_s \cdot \vec{B} = \frac{1}{2m^2c^2} \frac{1}{r} \frac{dU(r)}{dr} (\vec{s} \cdot \vec{l}) \quad (2.5)$$

with m the electrons rest mass, c the speed of light, r the distance between the incident electron with spin \vec{s} and angular momentum \vec{l} and the atomic nucleus. To solve Equation 2.5, a hydrogen-like potential $U(r) = Ze^2/4\pi\epsilon_0 r$ is assumed and following proportionality is found:

$$V_{\text{SOC}} \propto Z \cdot \frac{1}{r^3} \cdot (\vec{s} \cdot \vec{l}). \quad (2.6)$$

Evaluating the expectation value of $1/r^3$ under the assumptions made above, the proportionality to Z^3 is found, leading in total to $V_{\text{SOC}} \propto Z^4$ [38]. This dependence makes high- Z materials like W, Au or Pt appealing for the detection of the spin polarization.

2.4.2 Detection scheme

Historically, the fundamental discovery that enabled the development of spin detectors was made by Nevill F. Mott in 1929. He developed a theory on the scattering of electrons at atomic nuclei and pointed out that the corresponding scattering angles of the electrons depend on their spin [39]. Due to the spin-orbit coupling (SOC) introduced above, high- Z materials like for instance W are appealing for the application in spin detectors to investigate the spin polarization of electrons. In the LEED detector presented in the following, electrons are diffracted at 104.5 eV on a W(001) crystal and the intensities of the (2,0) beams are analyzed [40, 41]. An exemplary LEED pattern of W(001) [42] is shown in Figure 2.3a) and the four (2,0) beams are marked by red circles. Figure 2.3b)

⁴In contrast, also the exchange interaction gives rise to spin-dependent scattering amplitudes. This mechanism was e.g. used by Escher *et al.* who developed the FERRUM [37] detector in which SE are exchange scattered at a Fe(100)-p(1x1)O layer prepared on W(001).

2.4. Spin-polarized LEED detector

shows a scheme of the diffraction of the polarized SE at the W(001) which takes places at perpendicular incidence. The intensities of the four (2,0) beams of the resulting LEED pattern are then measured by single-electron counters to determine the spin polarization according to Equation 2.7.

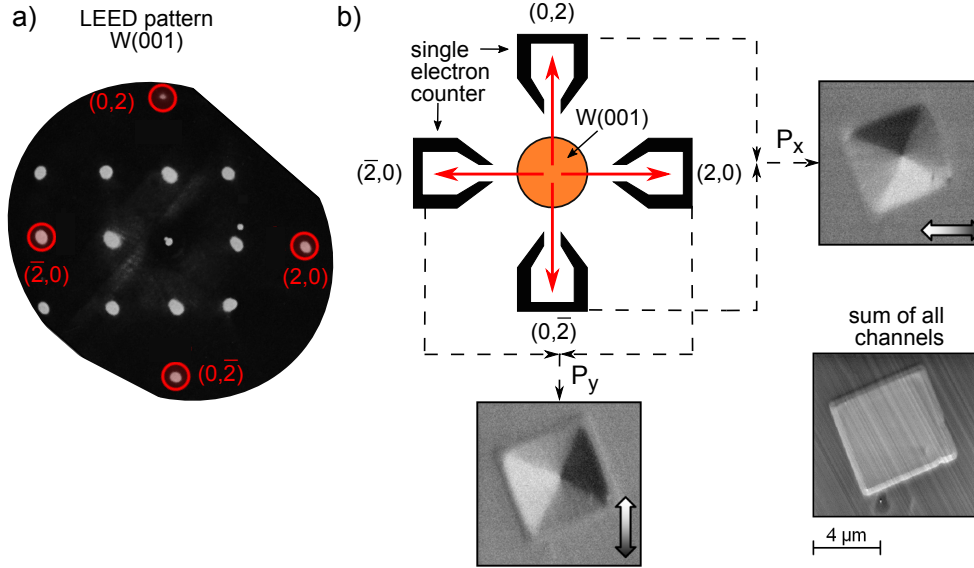


Figure 2.3: a) Exemplary LEED pattern of W(001) [42]. The four (2,0) beams are highlighted with red circles. b) The incoming spin-polarized secondary electrons undergo diffraction (red arrows) at the W(001) single crystal. Four single electron counters are positioned to measure the intensities of the four (2,0)-beams. The spin polarization P is obtained from the normalized intensity differences (asymmetries) of opposite channels according to Equation 2.7. Adding up the detected signals of the four channels results in a SE image without any magnetic information. The three exemplary grayscale images have been taken by S. Rößler during his PhD [43].

Spin detectors which rely on spin-orbit coupling for the analysis are sensitive to the electron polarization normal to the scattering plane⁵. Therefore, in a SEMPA as sketched in Figure 2.1, where the sample surface is aligned parallel to the surface of the W(001) crystal, the two in-plane components of the magnetization are accessible. In the detection scheme in Figure 2.3b) the resulting magnetization along the x- and y-direction for a small square patterned into $\text{Ni}_{180}\text{Fe}_{20}$ is shown exemplarily [43, 44]. A Landau state is observed which contains four in-plane magnetic domains forming a flux-closed structure to minimize the total energy. While the obtained gray-scale images for the two polarization directions

⁵To avoid a common misunderstanding it may be pointed out that the scattering plane is not defined by the plane of the crystal surface. Instead, the scattering plane is formed by the incoming beam and the scattered beam.

represent the magnetic information of the structure, the sum of all four detection channels gives a SE image showing solely the surface topography.

2.4.3 Characteristic values describing the detector performance

Prof. Jürgen Kirschner showed that for a W(001) based LEED detector a convenient operation point exists at an electron energy of 104.5 eV [30] which results in a high value for the so-called figure of merit (FOM). The FOM is equal to $2RS^2$ and is a measure for the detector efficiency. It is given via the Sherman function $S(E)$ describing the energy-dependent spin sensitivity of a scattering system and the ratio of elastically scattered electrons to incoming electrons of the primary beam, called reflectivity $R(E)$. A stable minimum of the Sherman function of $S = -0.27$ around 104.5 eV and a rather high reflectivity of 1.1 % at the same value result in a FOM of $1.6 \cdot 10^{-4}$. The asymmetry $A = PS$ which is measured by the spin detector is determined by both, the spin polarization from the sample and the Sherman function of the detector. For a fully polarized beam with $P=1$, the asymmetry is equal to the Sherman function:

$$A_x = \frac{N(0, 2) - N(0, \bar{2})}{N(0, 2) + N(0, \bar{2})}. \quad (2.7)$$

The intensity detected in the electron counters during a fixed dwell time is governed by Poisson statistics. The resulting statistical error for the polarization measurement is given by $\Delta P = 1/\sqrt{N \cdot S^2}$, with N , the sum of the number of detected electrons in both channels. The signal-to-noise ratio (SNR) can thus easily be determined by dividing the polarization P by its error

$$\text{SNR} = \frac{P}{\Delta P} = \frac{A/S}{\sqrt{1/(NS^2)}} = A \cdot \sqrt{N}. \quad (2.8)$$

2.5 Classification among magnetic imaging techniques

Several tools have been developed to explore magnetic properties and phenomena and allow for imaging magnetic domains and microstructures. In the following short overview, microscopy techniques comparable to SEMPA will be briefly introduced and a classification based upon their specifications will be given. The advantage of microscopy-based techniques in the field of studying magnetism lies within the fact that not only thin layers can be studied but mostly also bulk

2.5. Classification among magnetic imaging techniques

materials. An overview of the different technical approaches is given in Table 2.1, grouped by microscopy type, ranging from optical microscopes, over electron microscopes and scanning probe microscopes to soft x-ray microscopes.

Scanning Kerr microscopy (SKM) [45, 46] is chosen as representative for the optical microscopes. The magneto-optic Kerr effect (MOKE) uses changes in the polarization and the intensity of light reflected from a magnetized sample surface. Its information depth is given by the penetration depth of the used light, while the spatial resolution is limited by the wavelength of the latter. Time resolved studies allow investigations on the femtosecond timescale [47]. The size of the observed areas is given by the objective lens used in the light microscope. It may be noted that besides SKM also wide-field Kerr microscopy with a time resolution of about 20 ps [48] is an established technique.

The second group lists electron microscopy techniques, such as SEMPA, Lorentz microscopy [49], spin-polarized low-energy electron microscopy (SP-LEEM) [50] and electron holography [51]. While SEMPA and SP-LEEM are highly surface sensitive techniques, Lorentz microscopy and electron holography are transmission techniques and thus the obtained magnetic information is averaged over the electron trajectory through the sample. The spatial resolution of the electron based microscopes are in the same order of magnitude, the time resolution on the other hand varies from 700 ps (SEMPA) [52] over 700 fs (Lorentz microscopy) [53] up to 1 s for SP-LEEM⁶ [54]. An advantage of electron microscopes is their broad magnification range resulting in image sizes of several mm down to a few nm.

Exemplary scanning probe microscopy techniques are summarized in the third group. While magnetic force microscopy (MFM) [55] and nitrogen-vacancy (NV) magnetometry [56] detect the stray field of the sample, SP-STM (spin-polarized scanning tunneling microscopy) [55] uses spin-dependent tunneling to image domains. NV magnetometry is a rather new technique with a spatial resolution of 20 nm [57]. In this respect, it is comparable to MFM, while SP-STM offers atomic resolution.

Finally, techniques based on X-ray microscopy are listed, which all employ magnetic circular dichroisms (MCD) [58, 59]. The information depth of X-ray photoemission electron microscopy (X-PEEM) is determined by the used energy of the X-rays and ranges from a few ML to nm [60]. Scanning transmission X-ray microscopy (STXM) as well as X-ray holographic microscopy (XHM) use the resonant X-ray absorption as contrast mechanism, and thus the detected magnetic

⁶For SP-LEEM no pump-probe based time resolved setup exists. The time resolution here results from the measurement time needed to take one image.

Chapter 2. Scanning electron microscopy with polarization analysis

information has been averaged over the sample thickness. A time resolution in the lower picosecond range is currently feasible for these techniques. Nowadays, the time resolution of X-ray techniques lies in the ns to fs time regime [61] and is mostly limited by the length of the probe pulse provided by the used beamline.

Table 2.1: Comparison of microscopy techniques for magnetic imaging. Group 1: optical microscopy, group 2: electron microscopy, group 3: scanning probe microscopy, group 4: soft X-ray microscopy. From left to right the columns give details on the name of the technique, the physical effect that the technique is based on, the type of depth information (surface based SB or transmission T), the information depth itself, and spatial and temporal resolution.

★ The time resolution for the X-ray based microscopy techniques is mostly determined by the length of the probe pulse at the beamline, not by the experiment itself.

	technique	employed effect\quantity	inf. type	information depth	resolution spatial\temp.
opti.	scanning Kerr microscopy	MOKE	SB	5-10 nm	125 nm [47] \ 100 fs [47]
electron	SEMPA	spin-dependent LEED	SB	<5 ML [16]	3 nm [15] \ 700 ps [52]
	Lorentz microscopy	lorentz force	T	<100 nm [60]	< 10nm [62] \ 700 fs [53]
	e ⁻ holography	interference	T	<100 nm	5 nm [63] \ several μ s [64]
	SP-LEEM	spin-dependent scattering	SB	<1 nm [60]	< 10 nm \ 1 s [54]
scanning probe	MFM	stray field	SB	<2 μ m [60]	10 - 100 nm [55] \ —
	SP-STM	spin-dependent tunneling	SB	<0.2 nm [60]	atomic \ 120 ps [65]
	NV-magnetometer	stray field	SB	<2 μ m	20 nm [57] \ 100 ps [66]
X-ray	X-PEEM	MCD	SB	<5 nm [60]	2 nm [67] \ ns-fs [61] ★
	STXM		T	<500 nm	12 nm [68] \ ns-fs [61] ★
	XHM		T	<500 nm	12 nm [69] \ ns-fs [61] ★

2.5. Classification among magnetic imaging techniques

As all techniques presented here are complementary concerning their characteristics a broad spectrum of possible samples can be studied. Further details as the acquisition time, sensitivity to applied magnetic fields, the possibility to obtain depth selective information or the maximum field of view are not compared in the table, but can be found in the respective literature mentioned above or in further reading [54, 60, 70, 71].

Basics of Micromagnetism

In the following, a short introduction to micromagnetism and its terminology is given. Micromagnetism is a continuum theory that describes the magnetic behavior at the length scale between 1-1000 nm [72]. It is the connecting theory between quantum theory, which deals with the magnetism observed at the atomic scale, and domain theory, which applies to magnetic systems on the length scales between 1-1000 μm [72]. This overview is not intended to be all encompassing, for greater detail further reading is recommended as, e.g., in references [72–77]. The magnetic state of a ferromagnet is defined by several energy contributions which result in a specific local orientation of the magnetic moments. The total energy E_{tot} can be written as

$$E_{\text{tot}} = E_{\text{ex}} + E_{\text{d}} + E_{\text{ani}} + E_{\text{Z}} + E_{\text{DMI}} + E_{\text{IEC}}, \quad (3.1)$$

where E_{ex} describes the exchange energy, E_{d} the demagnetization energy, E_{ani} the anisotropy energy, E_{Z} the Zeeman energy, E_{DMI} the energy associated with the Dzyaloshinskii-Moriya interaction and E_{IEC} the interlayer exchange energy (in multilayers). These energy contributions are discussed individually in the following.

3.1 Exchange energy

The exchange energy is the origin of the macroscopically observed long-range magnetic order in a ferromagnet, though the interaction itself is short ranged [73, 74]. It is a quantum-mechanical effect resulting from the Coulomb interaction between electrons obeying the Pauli exclusion principle. The exchange energy can be expressed as a Hamiltonian H_{ex} in the Heisenberg model (atom-

istic approximation) [73, 74]:

$$H_{\text{ex}} = - \sum_{i \neq j} J_{ij} (\vec{S}_i \cdot \vec{S}_j) \quad (3.2)$$

The parameter $\vec{S}_{i,j}$ describes the spin of the atom i or j , while the exchange integral J_{ij} results from the wave function overlap of two electrons. A collective spin arrangement is preferred in systems with $J_{ij} \neq 0$, as it minimizes the total energy. For ferromagnetic materials is $J_{ij} > 0$ so that neighboring spins align parallel, for antiferromagnetic systems is $J_{ij} < 0$ which results in an antiparallel spin orientation.

In the micromagnetic approximation a transition from discrete to continuous variables is performed, replacing summations by integrals. For example the saturation magnetization M_S is introduced as the average density of magnetic moments replacing the spin. The exchange energy of a sample with volume V can thus be written as [75]

$$E_{\text{ex}} = A_{\text{ex}} \int_V \left(\nabla \frac{\vec{M}}{M_S} \right)^2 dV. \quad (3.3)$$

Here, \vec{M} is the magnetization and A_{ex} represents the exchange stiffness. Exemplarily, the exchange stiffness for bulk hcp Co at room temperature is $A_{\text{ex, Co}} = 30 \frac{\text{pJ}}{\text{m}}$ [78, 79].

3.2 Magnetostatic energy

The interaction of the magnetization \vec{M} with magnetic fields leads to two kinds of energy contributions, which add up to the magnetostatic energy. On the one hand, the Zeeman energy E_Z is the potential energy resulting from the interaction of the magnetization with an external magnetic field \vec{H}_{ext} [73]:

$$E_Z = -\mu_0 \int_V \vec{M} \cdot \vec{H}_{\text{ext}} dV \quad (3.4)$$

The dipolar energy E_d on the other hand is connected with the internal magnetic field \vec{H}_d . The latter field is generated by the magnetic body itself and called demagnetizing field or magnetic dipolar field. Applying the second Maxwell equation, the stray field is defined via

$$\text{div}(\vec{H}_d) = -\mu_0 \text{div}(\vec{M}) \quad (3.5)$$

3.3. Magnetic anisotropy

and arises if $\text{div}(\vec{M}) \neq 0$, meaning if sinks and sources of the magnetization exist. Examples for the latter are sample edges as well as domain walls. The stray-field energy is then given via [73]

$$E_d = -\frac{\mu_0}{2} \int_V \vec{M} \cdot \vec{H}_d dV. \quad (3.6)$$

As the magnetization \vec{M} is zero outside of the magnetic system, the integral in Equation 3.6 is taken over the volume V of the magnetic body. The analytical determination of \vec{E}_d is only possible for some limiting cases in which \vec{H}_d and \vec{M} are constant over the sample. One exceptional case is the homogeneously magnetized ellipsoid where the demagnetization field is defined by the demagnetization factor \overleftarrow{N} and the magnetization \overleftarrow{M} via [77]

$$\vec{H}_d = -\overleftarrow{N} \cdot \vec{M}. \quad (3.7)$$

For thin films, where the half-axes a, b, c of the ellipsoid fulfill $a = b \rightarrow \infty$ and $c \ll a$, the second-rank tensor \overleftarrow{N} equals [80]

$$\overleftarrow{N} = \begin{pmatrix} 0 & 0 & 0 \\ 0 & 0 & 0 \\ 0 & 0 & 1 \end{pmatrix}. \quad (3.8)$$

Thus, the term for the demagnetizing field can be expressed as $\vec{H}_d = -M_S \cos \theta$ and the stray-field-energy density $(E/V)_d$ equals

$$\left(\frac{E}{V}\right)_d = \frac{\mu_0}{2} M_S^2 \cos^2 \theta \quad (3.9)$$

with the angle θ between the film normal and the magnetization \vec{M} . The demagnetizing field and the correlated energy vanish in systems where the magnetization lies in the film plane ($\theta = 90^\circ$), and reaches its maximum value in case of complete perpendicular magnetization ($\theta = 0^\circ$). The difference of the stray-field-energy densities between these hard and easy directions of magnetizability is given by the shape anisotropy $K_d = -(\mu_0/2)M_S^2$, which originates from the dipole-dipole interaction, as derived above. For Co films, which exhibit a saturation magnetization of $M_S = 1.44 \text{ MA/m}$ at RT [81], the shape anisotropy amounts to $K_d = -1.30 \text{ MJ/m}^3$.

3.3 Magnetic anisotropy

Anisotropy energies result from spin-orbit interactions (SOI) and are the origin of the directional dependence of magnetic properties [72]. The magnetic

anisotropies arise from the undisturbed crystal lattice itself as well as from induced deviations to the crystal structure. The aforementioned shape anisotropy differs from these anisotropy terms, as it is not caused by the SOI but solely by the shape of the ferromagnet and the corresponding stray field. In the following, the discussion will be limited to the magnetocrystalline volume and surface anisotropies, which are of relevance for this thesis. Information on further anisotropy contributions due to roughening, interdiffusion or lattice strain can be found, e.g., in references [82–86].

3.3.1 Magnetocrystalline volume anisotropy

The magnetocrystalline volume anisotropy is a consequence of the SOC between the electron spin \vec{S} and the orbital momentum \vec{L} , which is linked to the crystal lattice. For crystal lattices that exhibit a uniaxial anisotropy, meaning that only one easy axis of magnetization exists, the energy density is a function of the angle θ between the magnetization \vec{M} and the c -axis of the crystal. This uniaxial energy density can be expanded into a power series giving [74]

$$\left(\frac{E}{V}\right)_{\text{MC,V}} = K_{1\text{V}} \sin^2 \theta + K_{2\text{V}} \sin^4 \theta + \mathcal{O}(\sin^6 \theta). \quad (3.10)$$

This expansion is usually terminated after the second order, as for higher order terms $K_i \gg K_{(i+1)}$ is found [74]. The coefficients $K_{1\text{V}}$ and $K_{2\text{V}}$ are the magnetocrystalline anisotropy constants of first and second order. These coefficient are often not reported separately, but as sum $K_{\text{V}} = K_{1\text{V}} + K_{2\text{V}}$. For bulk hcp Co, literature reports a value of $K_{\text{V}} = 0.5 \frac{\text{MJ}}{\text{m}^3}$ [81].

Including the shape anisotropy K_{d} , an effective volume anisotropy can be defined. For thin films, in which the magnetization points along the c -axis of the crystal, this effective volume anisotropy is given by $K_{\text{V,eff}} = K_{\text{V}} - (\mu_0/2)M_{\text{S}}^2$.

3.3.2 Interface anisotropy

Interfaces as well as surfaces represent a strong distortion to the translational symmetry of the crystal lattice and thus result in an interface anisotropy contribution K_{S} . The energy density $(E/V)_{\text{MC,S}}$ arising from this symmetry breaking was already predicted by Néel [87] and has been first observed by Gradmann and Müller [88]. In contrast to the volume anisotropy, the energy contribution originating from the surface/interface scales inversely with the film thickness t [89]:

$$\left(\frac{E}{V}\right)_{\text{MC,S}} = \frac{2K_{\text{S}} \sin^2(\theta)}{t} \quad (3.11)$$

3.4. Dzyaloshinskii-Moriya Interaction

The angle θ represents the angle between the film normal and the magnetization. A prefactor of two arises due to the fact that a film is bounded by interfaces on both sides. In systems where the contribution from the interface anisotropy is larger than the effective volume anisotropy, an out-of-plane easy axis of the magnetization is observed. Such a perpendicular magnetic anisotropy (PMA) occurs for ultrathin films as long as the film thickness is below a certain value $t_{\text{SRT}} = -2K_{\text{S}}/K_{\text{V,eff}}$. Exemplary Co-based systems with PMA are Co/Pt [90, 91], Co/Ir [91] or Co/Au [91–93]. Values for K_{S} in Co/Pt systems lie in the range of $K_{\text{S}} = (0.59 - 1.29) \frac{\text{mJ}}{\text{m}^2}$ [86, 94].

3.3.3 Effective magnetic anisotropy

Limited by the experimental possibilities of disentangling the contributions of the volume, surface, and shape anisotropy, literature often reports values for the effective magnetic anisotropy K_{eff} . In thin films with a PMA, the following expression is obtained:

$$K_{\text{eff}} = \underbrace{K_{\text{V}} - \frac{\mu_0}{2} M_{\text{S}}^2}_{K_{\text{V,eff}}} + \frac{2K_{\text{S}}}{t} \quad (3.12)$$

3.4 Dzyaloshinskii-Moriya Interaction

The Dzyaloshinskii-Moriya Interaction (DMI) [95, 96], which is a contribution to the exchange interaction and prefers adjacent spins to be canted, was first postulated by Igor Dzyaloshinskii in 1958 [97]. The theory has been refined by Toru Moriya in 1960 by finding that the SOC is the microscopic mechanism behind this interaction [96].

In recent years, the DMI has gained large attention in the field of thin magnetic films with perpendicular magnetic anisotropy. In these systems, the DMI is caused by SOC in the presence of a broken inversion symmetry at the interface between a ferromagnetic and a non-magnetic layer [10]. The DMI is an antisymmetric exchange interaction that supports a noncollinear order and leads to new magnetic states, such as magnetic skyrmions [13]. The Hamiltonian describing this interaction in ultrathin films between two ferromagnetic atomic spins \vec{S}_1 and \vec{S}_2 and a neighboring non-magnetic atom with large SOC is given by

$$H_{\text{DMI}} = -\vec{D}_{12} \cdot (\vec{S}_1 \times \vec{S}_2) \quad (3.13)$$

with the DMI vector \vec{D}_{12} . The DMI vector points perpendicular to the plane that is defined by the triangle of the three atoms, as seen in Figure 3.1.

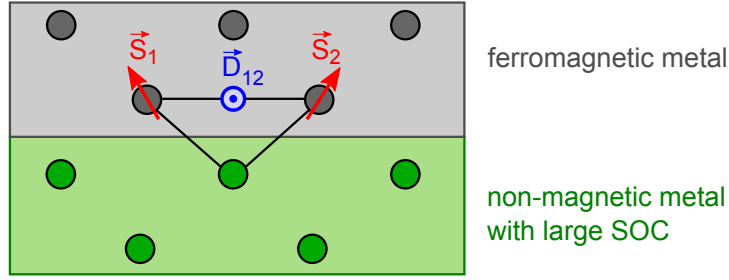


Figure 3.1: Schematic of the interfacial DMI. The ferromagnetic metal, shown in gray, contains the two atoms with the spins \vec{S}_1 and \vec{S}_2 , represented in red, which interact with an atom from a non-magnetic metal with large SOC, shown in green. The resulting DMI vector \vec{D}_{12} , shown in blue, is perpendicular to the plane defined by the triangle of the two ferromagnetic atoms and the atom with large SOC.

3.5 Interlayer exchange coupling

In 1986 several experiments [98–100] showed that two ferromagnetic layers, which are separated by a non-magnetic spacer layer, are coupled to each other by an exchange interaction. The intensive study of this interlayer exchange coupling (IEC) effect - experimentally as well as theoretically - was motivated by numerous discoveries, like in 1990 the giant magnetoresistance effect [101]. It was found that the IEC is able to stabilize a collinear alignment of the magnetization (parallel or antiparallel) as well as a non-collinear one [102].

In its simplest form, the energy per area of the IEC is given for a system of two magnetic layers by

$$\left(\frac{E}{A}\right)_{\text{IEC}} = -J_{\text{IEC}} \vec{M}_1 \cdot \vec{M}_2, \quad (3.14)$$

with the coupling constant J_{IEC} and the direction of magnetization of the two magnetic layers $\vec{M}_{1,2}$. Equation 3.14 neglects an additional biquadratic term, which is said to be related to the roughness of the interfaces or interdiffusion [103]. Often, the greater interest lies in the study of the bilinear term, which accounts for the collinear alignment, as given here. For coupling constants $J_{\text{IEC}} > 0$ a parallel alignment of the magnetizations between the layers exists, while for $J_{\text{IEC}} < 0$ an antiparallel alignment is favored. The value and sign of J_{IEC} oscillates with the thickness of the non-magnetic interlayer. Several theoretical approaches have been proposed to describe the IEC, which are, e.g., based on the Ruderman-Kittel-Kasuya-Yosida (RKKY) theory [104], quantum confinement [105] or a free-electron model [106, 107]. In 1993, all these models have been unified into

3.5. Interlayer exchange coupling

a theoretical description using quantum-well states [108, 109]. In brief, free electrons reflect from the interface between the ferromagnetic and non-magnetic layer, which acts as a spin-dependent step in the potential, and interfere with each other. Constructive interference leads to resonances and bound states that are referred to as quantum well states. The quantum well states experience a shift in energy as soon as the thickness of the non-magnetic interlayer is varied. The oscillations in the IEC take place whenever a quantum well resonance crosses the Fermi energy of the non-magnetic interlayer material. For further reading concerning the theory of quantum well states to describe the IEC reference [110] is recommended.

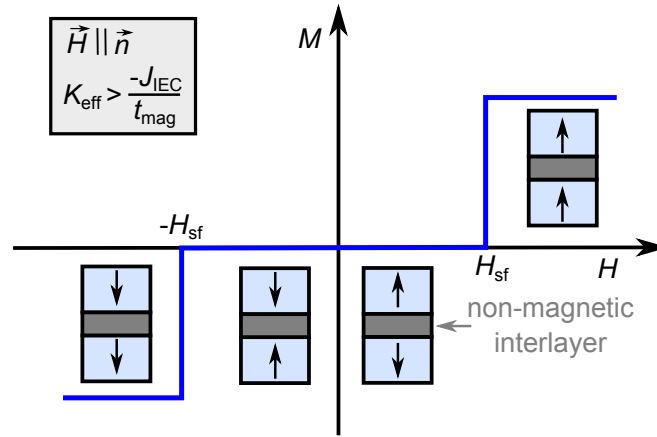


Figure 3.2: Theoretically expected magnetization curve for a system of two identical antiferromagnetically-coupled ferromagnetic layers (bright blue) that exhibits a strong PMA and fulfills $K_{\text{eff}} > -J_{\text{IEC}}/t_{\text{mag}}$. The sample is subjected to a magnetic field which points along the film normal \vec{n} . For magnetic fields greater than a certain field strength H_{sf} , the so-called switching field, the magnetization of both layers is aligned along the direction given by the external magnetic field \vec{H} . Decreasing the field strength leads to a switching of one of the two layers at H_{sf} , which results in an antiparallel alignment of the two layers. This antiparallel alignment exists also at zero field. A further reduction of the magnetic field below $-H_{\text{sf}}$ leads to the switching of the second magnetic layer so that the magnetization of both layers again points into the direction of the applied field.

Figure 3.2 shows the theoretically expected hysteresis curve for a system with strong PMA and two identical ferromagnetic layers fulfilling $K_{\text{eff}} > -J_{\text{IEC}}/t_{\text{mag}}$, with J_{IEC} the coupling constant and t_{mag} the thickness of each of the magnetic layers. The magnetic field is applied along the easy axis of the system, meaning along the normal of the sample surface \vec{n} . The magnetization curve shows, besides the two plateaus where the magnetization of both magnetic layers points

into the same direction, a third plateau around zero field. In this range, one of the two layers has switched due to the applied magnetic field at a certain switching-field strength H_{sf} , which results in an antiparallel alignment of the magnetization in the layers. By determining the switching field, the strength of the coupling constant for the case of $K_{eff} > -J_{IEC}/t_{mag}$ can be derived via [111]

$$J_{IEC} = -\mu_0 M_S t_{mag} H_{sf}. \quad (3.15)$$

It may be noted that in literature, sometimes an additional factor of 0.5 is found for Equation 3.15. This deviation results from a different definition of Equation 3.14, which includes an additional factor of 2 [111]. Furthermore, Equation 3.15 assumes that the system shows no coercivity, which would result in a deviation of the switching fields observed in the forward and backward sweep of the magnetization curve. In such cases, it is common to average the values of both switching fields, though it is known that this handling does not always give the correct results [111].

3.6 Magnetic domains in thin films with PMA

In contrast to the so far considered homogeneous magnetization distribution in a sample, in general only small regions of uniform magnetization exist in ferromagnetic materials. These so-called magnetic domains result in a net inhomogeneous magnetization distribution thereby reducing the demagnetizing field in order to achieve lower total energy. Two domains are separated by a domain wall (DW) in which the magnetization rotates gradually over several (hundreds of) atoms. The following discussion will be restricted to thin-film systems where the easy axis of magnetization points perpendicular to the sample surface. The origin of these magnetic domains and the different types of domain walls in thin films with PMA will be introduced.

3.6.1 Origin of domains and domain walls

In order to minimize their total energy, ferromagnetic systems will form domains. In a homogeneously magnetized ferromagnet the demagnetization energy E_d is maximized, see Equation 3.9. By creating domains with opposite magnetization directions, meaning the magnetization direction changes by 180° , the extension of the stray field outside the sample is reduced as the magnetic flux closes its loop within the domains in the sample which leads to a decrease of the demagnetization energy. Inside a domain, the magnetization is homogeneous and the

3.6. Magnetic domains in thin films with PMA

exchange energy E_{ex} is minimized.

Splitting into two domains on the other hand also requires energy to build the domain wall between the neighboring magnetization regimes as the rotation of the magnetization within the wall is favored neither by the exchange nor by the anisotropy. As long as the corresponding reduction of the stray-field energy surpasses the energy needed for the domain-wall creation, the implementation of a domain wall is energetically favorable. A stable domain size is reached when these two energy terms outweigh each other, meaning the minimum of the total energy has been reached. Between the domains, domain walls are formed in which a gradual rotation of the magnetization takes place over several (hundreds of) atomic spins. The explicit width of a domain wall is determined by the interplay between the anisotropy and the exchange energy as both terms seek for minimizing their energy contribution. The anisotropy energy reduces when the spins are aligned along the easy axis and thus with decreasing width of the domain wall. Contrarily, broader domain walls lower the energy contribution of the exchange energy, as the exchange prefers an alignment in which the angle between adjacent spins is as small as possible.

3.6.2 Bloch and Néel walls

In thin films with PMA, the magnetization direction in adjacent domains changes by 180° . The corresponding domain-wall types, namely the Bloch and the Néel wall, will be introduced qualitatively¹. Both domain-wall types are sketched in Figure 3.3 for a system with PMA. In a Bloch wall, the magnetization rotates around the axis given by the direction of the DW and thus within the plane of the domain wall. Bloch walls are favored in bulk materials and thick films where the magnetization lies in plane, as in this case only a negligible amount of surface charges but no volume charges arise. In contrast, Néel walls generate volume charges in in-plane systems while the film surface stays free of charges. The magnetization rotates in a plane perpendicular to the domain wall, along the domain wall direction. As can be seen from Figure 3.3, in systems with PMA both wall types result in a local reduction of the surface charges. While in the case of the Bloch wall also no volume charges arise, Néel walls insert volume charges into the system. Nevertheless, Néel walls are observed in certain thin film systems with PMA due to the influence of the DMI. The DMI adds to the domain-wall energy in such a way that Néel walls of a given sense of rotation

¹A quantitative description of the domain wall is not needed within this thesis, but can be found in literature, for example in reference [72].

become energetically favorable over the magnetostatically favored Bloch walls [112–114]. When the DMI is not strong enough to enforce a pure Néel wall, "tilted" Néel walls with a Bloch contribution arise. Furthermore, the existence of pure Néel walls or Néel-like domain walls with a Bloch contribution can be used to derive values for the DMI strength [115, 116].

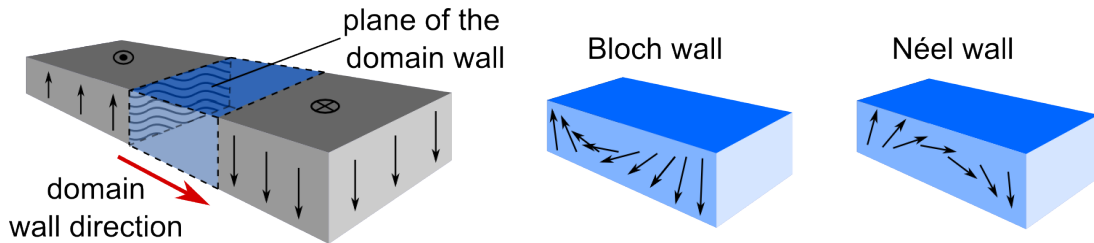


Figure 3.3: Schematic for a Bloch and Néel domain wall in a perpendicular magnetized sample. The plane of the domain wall and its direction are marked with a wave pattern and a red arrow, respectively. In a Bloch wall, the magnetization rotates in a plane parallel to the domain-wall plane, and thus around the domain-wall direction. In a Néel wall, the magnetization rotates in a plane perpendicular to the domain-wall plane, meaning along the domain-wall direction.

Experimental aspects

In this chapter, the two SEMPA instruments used within this thesis will be introduced and experimental details specific for the setups will be discussed. At first, the key features of the in-plane SEMPA, which allows to detect both in-plane components of the magnetization, will be presented briefly. The investigations on Co/Pt(111), given in Chapter 6, have been performed with this setup. In the second part, the characteristics of the out-of-plane SEMPA, which was brought back into operation within this thesis, is discussed in detail. The Pt-cap-layer-thickness-dependent study on Pt/Co/Ir presented in Chapter 7 has been performed on this machine. Furthermore, the design of a new Au/Ir(001)-based spin detector, presented in Chapter 5, is tailored for this specific instrument.

4.1 Basic introduction to the in-plane SEMPA setup

The in-plane SEMPA instrument which allows the detection of both in-plane components of the magnetization is the established SEMPA setup in the work group 'Grenz- und Oberflächenphysik'. It has been in use for over a decade and the setup has been constantly optimized ever since. In the following, only a brief introduction to this setup and its specifics will be given. The interested reader is referred to publications and theses providing detailed information on this instrument, e.g. references [44, 52, 117, 118].

The current state of the UHV setup is shown in Figure 4.1. The schematic drawing illustrates the equipment of the different chambers, which is discussed separately in Section 4.1.1 as well as the detection of the in-plane components of the magnetization, on which remarks are given in Section 4.1.2.

4.1.1 Facilities for sample preparation

The in-plane SEMPA setup consists of three chambers: the load lock, the SEMPA chamber and a preparation chamber. Due to the latter, the setup allows for the study of in-situ grown ultrathin films.

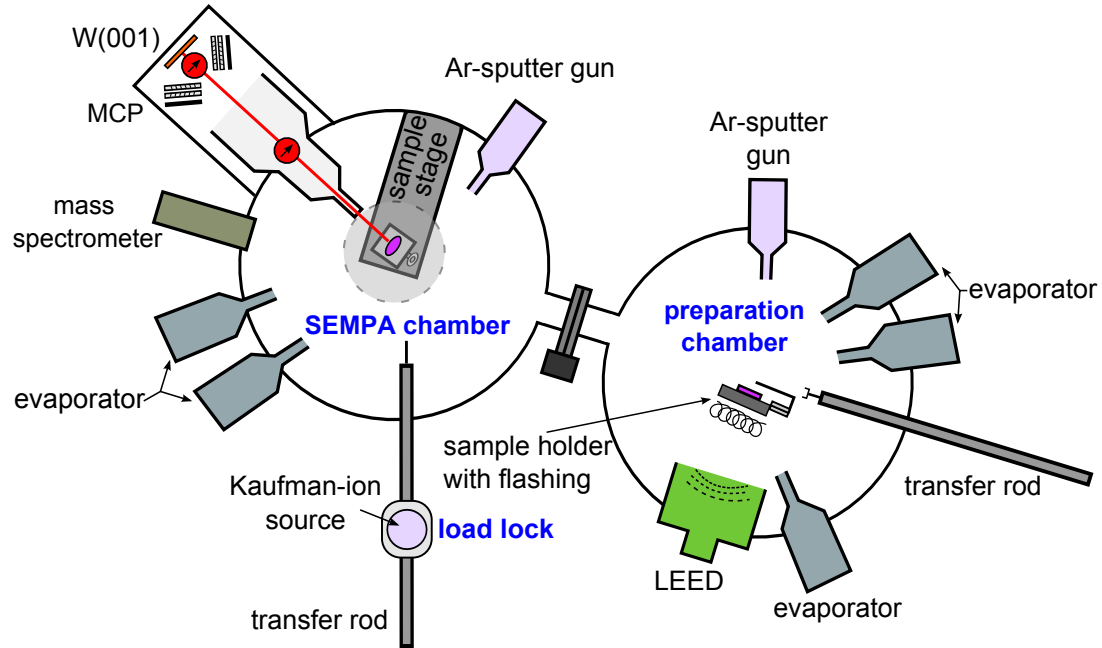


Figure 4.1: Top view sketch of the in-plane SEMPA instrument. Via a load lock, on which a Kaufman-ion source is attached, the samples are transferred into the SEMPA chamber. The sample stage is equipped with a manipulator with five degrees of freedom which ensures to adjust the sample position in respect to all three components of translation, to rotate about the z-axis, as well as to tilt it. Aligning the sample surface parallel to the W(001) crystal allows the detection of both in-plane components of the magnetization. Four micro-channel plate (MCP) based detectors are used for single-electron counting of the (2,0) LEED beams scattered at the tungsten surface. In the SEMPA chamber, the sample can be sputtered with Ar^+ ions and decorated with magnetic material (Co, Fe) to enhance the magnetic contrast. A UHV preparation chamber, which is directly attached to the SEMPA chamber, allows the investigation of in-situ prepared samples. The sample holder of the preparation chamber is equipped with an electron-beam heater which allows for flash heating and annealing of the samples. Well-defined surfaces of single crystals can thus be prepared by cycles of flashing and Ar^+ -ion sputtering. Several evaporators attached to the preparation chamber give the possibility of depositing single layers or multilayers of various materials onto the substrate. The quality of the surface of the cleaned crystal as well as the growth of evaporated material can be checked via a rear-view LEED instrument.

4.1. Basic introduction to the in-plane SEMPA setup

The preparation chamber with a base pressure of 10^{-10} mbar, seen on the right of Figure 4.1, allows for a heat treatment of samples via an electron-beam heater integrated in the sample holder. By dosing pure oxygen into the UHV chamber, a hot oxygen treatment of the samples is realized to remove carbon contaminants. Alternating the heat treatment with Ar^+ -sputtering allows to obtain clean and crystallographically ordered surfaces of single-crystalline samples.

The multitude of water-cooled e-beam evaporators attached to the preparation chamber offers a variety of materials to be deposited on the sample. Besides the ferromagnetic materials Co, Fe and Ni, which are favorable for SEMPA, it is amongst others equipped with Au, Pt and Ir. A rear-view LEED instrument is used to evaluate the quality of the cleaned single crystals as well as the growth of the deposited layer.

An Ar^+ -sputter gun and two evaporators, equipped with Fe and Co, ensure a basic sample treatment in the SEMPA chamber ($p \simeq 5 \cdot 10^{-11}$ mbar). These evaporators are used to enhance the magnetic contrast by dusting ferromagnetic material on top of the sample, often after short sputtering [119–121]. Such a decorating treatment is among others needed for the study of ex-situ prepared samples. In those the magnetic film is usually protected by a cap layer which has to be removed by sputtering. The sputter gun attached to the SEMPA chamber is designed for a material removal with ions of medium kinetic energy (acceleration voltage in the order of 1 – 2 kV). It results in an roughening of the surface as well as in an intermixing of ultrathin layers, and is thus not the appropriate tool to remove cap layers of several nm thickness. Instead, the Kaufman ion source (Kaufman & Robinson, KDC10) mounted to the load lock ($p = 10^{-8}$ mbar) offers the method of choice, as the low energy of the used ions (acceleration voltage about 100 – 200 V) results in less intermixing.

4.1.2 Detection of the in-plane magnetization

The SE are accelerated towards the spin detector via a transfer optic whose first lens generates a potential gradient and thus attracts the electrons emitted from the sample. The spin detector used in the in-plane SEMPA contains, besides the W(001) crystal biased at +102 V, four micro-channel plate (MCP) based detectors (MCPs in chevron stacking) which detect the spin-dependent scattered SE. A single electron arriving at the MCP generates an electrical pulse of a few nanoseconds length, which is then further processed via a counter card and a measurement computer. Defocussing electrodes in front of the MCP stacks broaden the electron beam and thus lead to a more uniform wear of the micro

channels. The W(001) crystal is cleaned by flash heating from its rear via electron bombardment from a hot filament.

The detection of both in-plane components of the magnetization is accomplished by aligning the sample surface parallel to the surface of the W(001) crystal. As pointed out in Section 2.4.2, the spin dependent diffraction is solely sensitive to the spin component normal to the scattering plane. Thus, both in-plane components are detected when the sample is aligned parallel to the W(001) crystal. In contrast, slight tilting of the sample and thus misaligning the sample surface in respect to the W(001) crystal leads to detecting a projection of the out-of-plane component (if present) in one of the in-plane channels. This effect is exploited in the study of Co/Pt(111) presented in Chapter 6.

The in-plane SEMPA setup allows not only to perform static studies of magnetic systems, but also offers the possibility for investigating the dynamics in magnetic samples. Details concerning this time-resolved imaging of the in-plane magnetization with the in-plane SEMPA can be found in references [52, 122].

4.2 Specifics and performance of the out-of-plane SEMPA setup

The following section focuses on the experimental implementation at the out-of-plane SEMPA instrument which detects, besides one in-plane component, the out-of-plane component of the magnetization. Thus, the out-of-plane SEMPA is ideally suited for the surface-sensitive investigation of magnetic thin films with a perpendicular anisotropy. The basic assembly of the out-of-plane SEMPA was implemented before the beginning of this PhD work and had reached a state in which the basic operation was proven on a Fe whisker [123]. While the general functionality of the transfer and the spin-dependent diffraction of the electrons were demonstrated, the resulting magnetization images were unsatisfactory as they lacked spatial resolution. This issue resulted from the used SEM gun Hitachi S-800. F. Lofink reports in [123] of using this setup with a cold cathode¹ for the creation of the PE beam which provided at an acceleration voltage of 10 keV only a very low electron current in the range of ≈ 0.6 nA. Removing of the aperture behind the objective lens increased the PE current to 3 nA [123] but was accompanied by diminishing spatial resolution to roughly 200 nm [123] at

¹The cold cathode was prior to Lofinks work temporarily customized into a heated cathode as the cold cathode provided an unstable electron current [124]. Lofink did not report on such current instabilities in his thesis.

4.2. Specifics and performance of the out-of-plane SEMPA setup

the used working parameters for SEMPA investigations which prohibited the detailed investigation of recent scientific topics on the lower-nm length scale. In the first part of this PhD work, the performance of the setup was optimized. A crucial initial step was to exchange the Hitachi S-800 with an UHV Gemini electron column (Scienta Omicron). The latter is equipped with a Schottky field emitter ensuring a stable and sufficiently high PE current. Furthermore, the emitted PE are formed into an electron beam with smaller diameter, and result thus in an increase of the spatial resolution. After a general introduction to the experimental implementation in Section 4.2.1, the preparation possibilities within the in-plane SEMPA setup are covered in Section 4.2.2. The key feature of this SEMPA, the deflection of the SE beam in order to access the out-of-plane component of the magnetization, is presented in Section 4.2.3. The Sections 4.2.4–4.2.6 present details on the technical implementation of the used spin detector, optimizing its performance by choosing a modified set of voltages and determining the characteristics of the W(001) crystal itself. The obtained spatial resolution and measures to ensure noise cancelling are discussed in Sections 4.2.7 and 4.2.8. Finally, the steps of the magnetic image formation are visualized in Section 4.2.9.

4.2.1 Introduction to the out-of-plane setup

Before specific details of the out-of-plane SEMPA are discussed, a general introduction to the setup is given in the following. The sample transfer into the microscope chamber is performed via a load lock chamber, seen in the lower left of the sketch in Figure 4.2. An ECR type Ar⁺-ion sputter gun for low-energy operation, attached to the load lock chamber, allows for sample preparation before transferring the specimen into the sample stage of the microscope chamber. The sample stage is equipped with a stack of three piezoelectric actuators² for x- and y-movement (5 mm travel range) as well as for rotation about the z-axis ($\hat{=}$ normal of the sample surface), see Figure 4.3. On top of this stack of piezoelectric actuators, the sample is positioned on a sample holder. The resulting working distance used for investigations via SEMPA equals 10 mm. The surface normal of the sample points into the entrance optics of the spin-detector arm and forms an angle of 64° with the primary beam of the SEM column. It is further more possible to sputter clean the sample with Ar⁺ ions or to evaporate iron. A residual gas analysis can be performed by using a mass spectrometer

²Piezoelectric actuators by AttoCube: ANP x 101-91 for the two linear stepper positioner and ANR-200-D5 as the rotary stepper positioner.

(Quadstar, Balzers). The microscope chamber as well as the spin-detection arm are equipped with ion gauges for pressure reading, confirming a base pressure in the range of 10^{-11} mbar.

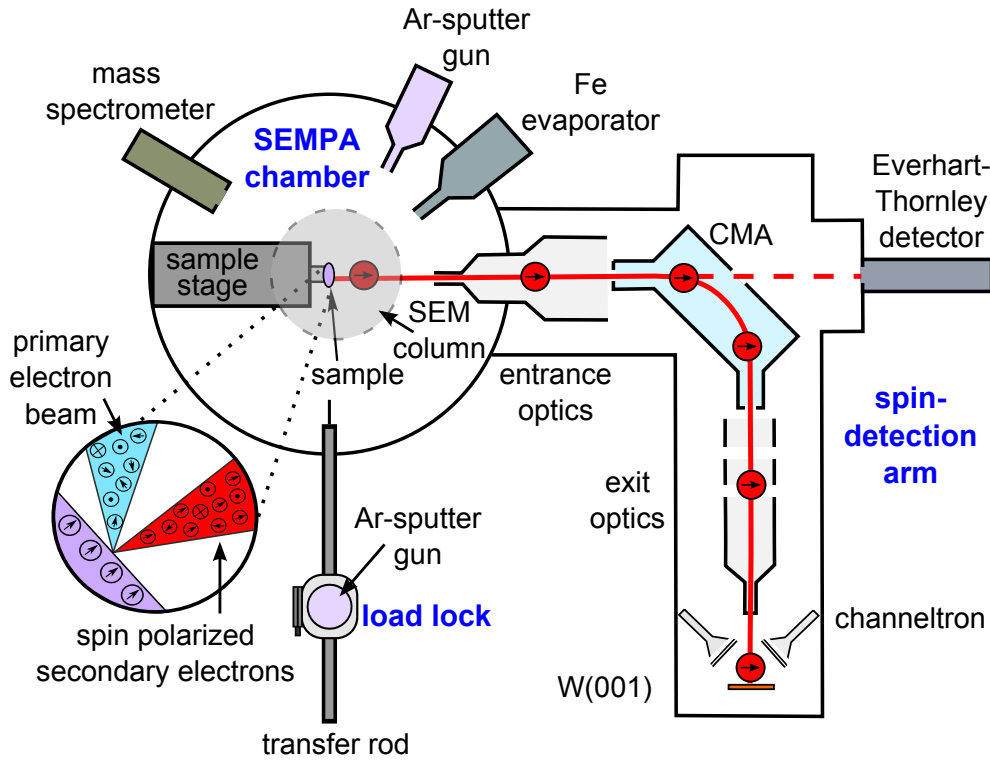


Figure 4.2: Top view schematic of the out-of-plane SEMPA setup. The individual components of the SEMPA chamber (round, left) and the spin-detection arm (L-shaped, right) as well as the trajectory of a spin-polarized electron (red) is shown. While the load lock includes an ECR Ar^+ -ion sputter gun for sputtering at low energies, a scanning Ar^+ -ion sputter gun designed for high-energy sputtering is attached directly to the SEMPA chamber. An Fe evaporator and a quadrupole mass spectrometer are available for preparation and analysis purposes. The SEM column, indicated by a semitransparent circle in this top view, accelerates the unpolarized PE beam (blue in the zoom in on the left) onto the magnetic sample (purple), which induces the emission of spin-polarized SE (red). The SE are attracted by the entrance optics and accelerated into the CMA, which bends the trajectory of the SE beam by 90° without affecting the orientation of the spin. This process is illustrated for electrons originating from an out-of-plane magnetized sample region. The exit optics accelerates the SE onto the W(001) crystal to undergo LEED.

To perform a SEMPA measurement, a Gemini SEM column (indicated by a gray semitransparent circle with dashed outline, side-view geometry as in Figure 2.1 on page 8) is used to locally emit SE from the sample. Those are at-

4.2. Specifics and performance of the out-of-plane SEMPA setup

tracted by the first stage of electrodes, the so-called entrance optics, accelerated into the detector chamber, and steered and focused by quadrupoles. After passing the entrance optics, the electrons enter a cylindrical mirror analyzer (CMA) which is used in this instrument to bend the trajectory of the SE by 90° . At the chosen potentials, the energy dispersive features of the CMA do not impair the transmission of the SE as will be shown in Section 4.2.3.

In the second stage of electrodes, the so-called exit optic, the SE are then accelerated onto the W(001) crystal where they undergo LEED. The diffracted electrons of the (2,0)-reflexes are then detected by channeltrons. The red circles with black arrows in Figure 4.2 represent electrons with a spin orientation normal to the sample surface and visualize the working principle of the out-of-plane measurements: For electrons with nonrelativistic velocities as present here, the electrostatic field rotates the velocity vectors of the electrons but does not affect their spins, so that a longitudinal polarization is translated into a transverse one [29]. Thus, it becomes possible to measure the out-of-plane component of the sample magnetization. Besides the out-of-plane component, the y-component of the in-plane magnetization is measured simultaneously. The corresponding x-component is accessible by rotating the sample by 90° about the z-axis (normal of the sample surface) via a piezoelectric actuator.

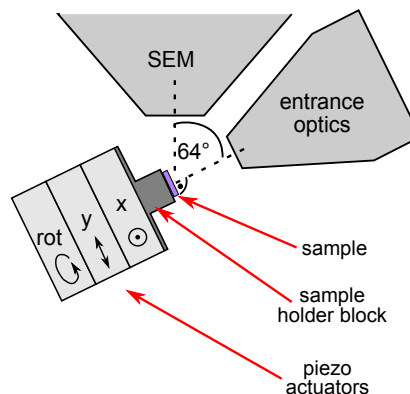


Figure 4.3: The sample is positioned on a stack of three piezoelectric actuators which allow for movement in the x- and y-direction of the sample plane as well as rotation around the normal of the sample surface. Its surface normal points directly into the entrance optics of the spin-detector arm and forms an angle of 64° with the primary beam of the SEM column.

4.2.2 Facilities for sample preparation

In contrast to the in-plane SEMPA described in Section 4.1, no dedicated preparation chamber is attached to the out-of-plane setup. Nevertheless, to a lesser extent sample treatment is possible by means of sputter cleaning or metal evaporation. Both processes have been characterized and will be introduced in the following.

The transfer chamber, which is pumped via a turbo-molecular pump down to a pressure of $9 \cdot 10^{-8}$ mbar, is equipped with an Ar^+ -sputter gun (IonEtch, Tectra). The latter is a filamentless ion source which is based on a microwave plasma discharge, employs the electron cyclotron resonance (ECR) effect and works on an argon pressure of $p_{\text{Ar}} = 6 \cdot 10^{-5}$ mbar. It is designed to work at energies as low as 25 eV to ensure a smooth and even removal of material layers without causing too much intermixing. The divergence of ion beams and the beam profile are known to depend on the acceleration voltage, in general for increasing acceleration the beam becomes more convergent [125, 126]. Thus, the homogeneity of the profile of the resulting Ar^+ -beam is expected to be influenced by the used anode voltage. For evaluating the homogeneity of the sputtering process, well defined platinum films on Si_3N_4 have been sputtered with different settings. An optical ellipsometer (SENpro, SENTECH Instruments) has been used to measure the Pt-film thickness before sputtering and to detect the thickness profile across the sample after the Ar treatment.

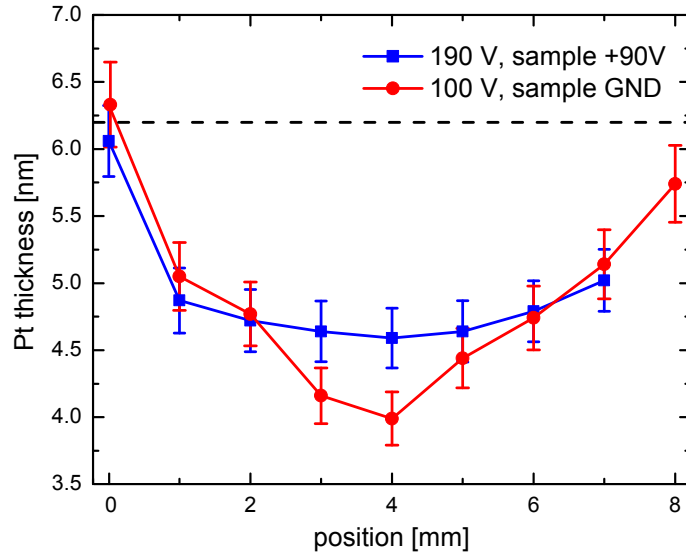


Figure 4.4: ECR-sputtered profiles of two originally 6.2 nm thick platinum layers (black dashed line) on Si_3N_4 , both sputtered at a kinetic ion energy of 100 eV. The red curve shows the obtained profile of the sample sputtered at an anode voltage of 100 V with the sample at ground. In contrast, the blue profile has been obtained by sputtering at an anode voltage of 190 V with the sample biased at +90 V. These different modi can be used either for homogeneous sputtering or for a specifically inhomogeneous material removal to obtain a depth profile.

The sputtering profiles for two settings leading to a homogeneous and an inhomogeneous material removal are presented in Figure 4.4. In both cases, an effective

4.2. Specifics and performance of the out-of-plane SEMPA setup

ion energy of 100 eV has been used. While for the red curve the sample was at ground potential and an anode voltage of 100 V was applied, a sample potential of +90 V and an anode voltage of 190 V was used for the blue curve. The black dashed line in the graph indicates the original thickness of the platinum layer of 6.2 nm. Adhesive copper foil was used to fix the sample on the holder and to cover a small part of the sample surface (see x-axis at 0 mm) to check the consistency of the thickness determination. Thus, at the sample position of 0 mm, the measured layer thickness is identical to the one of the unspattered system. While the blue curve describes a rather homogeneous removal of the platinum layer, the red profile indicates an uneven material removal with the highest sputter rate in the center of the sample. For an anode voltage of 190 V, an Ar⁺-beam is formed which yields a rather position-independent flux of Ar⁺-ions over the sample area (about 1 cm²). In contrast, for the case of an anode voltage of 100 V, a density gradient of the provided Ar⁺-ions exists across the surface of the sample. These two operation modi in the low energy regime can thus either be used for a homogeneous material removal such as a capping layer, or for the purposeful inhomogeneous removal for depth profiling of multilayer samples.

Within the SEMPA chamber, an Ar⁺-sputter gun as well as an e-beam evaporator are available. Enhancing the spin contrast in a SEMPA measurement can be achieved by dusting the sample with Fe from the evaporator (EFM 3, Focus). A deposition rate³ of 0.38 nm/min has been used for such purposes.

The scanning Ar⁺-sputter gun (IQE 12/38, Leybold) next to the evaporator accelerates the used Ar⁺-ions to kinetic energies in the range of 1 – 5 keV and leads to an increased surface roughness upon sputtering. This also results in intermixing of layers making this sputter gun not applicable for the preparation of delicate ultrathin magnetic multilayers. For sputtering with the maximum scan area (10 mm x 10 mm) at 2 keV a removal rate⁴ of 3.12 nm gold/h (0.052 nm gold/min) was determined. When reducing the sputtered area, the sputter rate increases accordingly. The desired area can be chosen by adjusting the range at the scanning unit and checking the sample-current-based imaging readout, see Figure 4.5. The latter imaging mode is based on the fact that the sample current depends on the position of the ion beam on the sample, as the SE emission depends on the local material composition and surface topology.

³The settings for this deposition rate are $U = 1$ kV, $I_{\text{emis}} = 12$ mA, $I_{\text{flux}} = 1$ nA and $I_{\text{fil}} = 2.1$ nA

⁴Used parameters: $U_{\text{energy}} = 2000$ V, $U_{\text{extractor}} = 1871$ V, $I_{\text{emission}} = 3$ mA, $U_{\text{foc1}} = 1594$ V and $U_{\text{foc2}} = 1536$ V

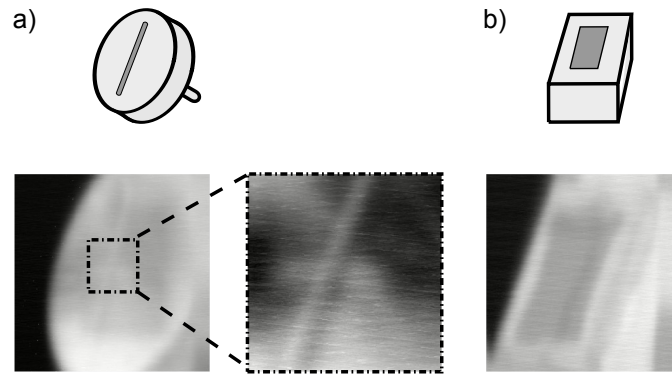


Figure 4.5: Sample-current images obtained with the scanning-sputter gun from two different samples at 2 keV. a) The sketch shows an Fe whisker that is glued with conductive silver onto an SEM sample stub. Below, the corresponding full-range (10 mm x 10 mm) sputter image and a zoom onto the whisker is shown. b) Sketch and sample-current image of a cuboid sample holder block with a Au/Si₃N₄ sample on top. The Si₃N₄ wafer is clearly recognizable in the current image, which allows to adjust the beam deflection in such a way that only selected regions can be purposely sputtered.

4.2.3 The transfer optics of the spin detector

For detecting the spin polarization of the SE emitted from the sample, they are accelerated into the spin-detection arm. First, they fly through the entrance optics, which collects the SE from the SEMPA chamber and focuses them into a CMA to bend their trajectory by 90°. After exiting the CMA they pass the *exit optics* to finally undergo LEED on a W(001) crystal. A sketch of these three stages, which will be described in detail in the following, can be seen on the right-hand side in Figure 4.2, depicting their mutual orientation. The spin-detection arm is shielded with a μ -metal foil that is wrapped around it on the outside to minimize detrimental magnetic stray fields.

Entrance optics

The entrance optics acts as the transition from the SEMPA chamber to the spin-detection arm. This optics consists of six electrostatic lenses, among which two are built as quadrupoles for beam steering. Figure 4.6 shows the CAD (computer-aided design) sketch indicating the positions of the lenses. Quadrupole #1 extends into the SEMPA chamber as can be seen in Figure 4.2. It creates a gradient of an electric potential to attract the SE. The following lenses parallelize the elec-

4.2. Specifics and performance of the out-of-plane SEMPA setup

tron beam before the latter is focused into the entrance of the CMA by a second quadrupole (#4) and the final lenses.

An Everhart-Thornley detector has been mounted on the spin-detection arm (after the CMA, see Figure 4.2) in a straight line along the axis of the entrance optics. A small opening in the outer cylinder and shielding of the CMA is matched with this line to let the electrons pass when inner and outer cylinder are held at the same potential. This allows to optimize the potentials of the lenses and quadrupoles, so that the path of the focused electron beam is aligned with the entrance axis of the CMA. While the optimized lens potentials vary slightly in dependence of the sample position, the following values can be used as reference/starting point:

quad. #1	lens #2	lens #3	quad. #4	lens #5	lens #6
2.5 kV	1.0 kV	3.0 kV	2.5 kV	2.8 kV	inner CMA potential

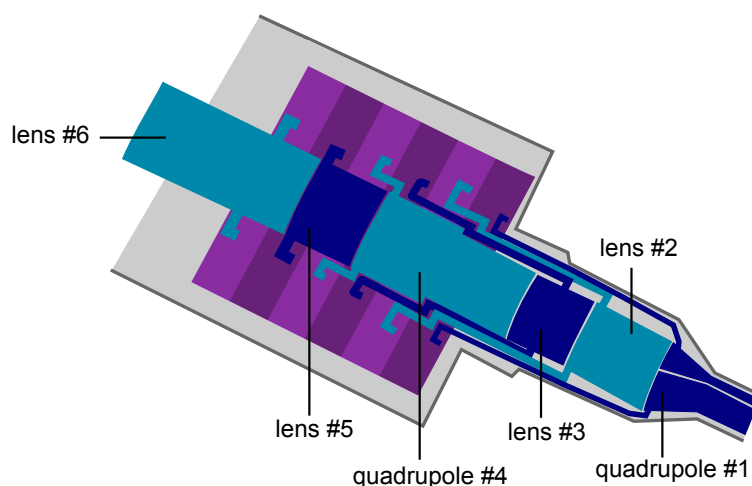


Figure 4.6: Sequence of electrostatic lenses and quadrupoles making up the entrance optics. They are assigned to attract the SE emitted from the sample, allowing their analysis in the LEED detector.

Cylindrical mirror analyzer

Electron analyzers are generally used in spectroscopy to sort electrons by their kinetic energy. In this SEMPA instrument, a CMA is used exploiting the fact that it bends the trajectory of the SE by 90° . Figure 4.7 shows a sketch of a CMA with its two concentric cylindrical electrodes. The SE enter the CMA through a slit of width ω , which is located at a radius r_i with respect to the symmetry axis.

By choosing specific potentials for the electrodes, only electrons with energies around a certain kinetic energy, the so-called pass energy, are able to reach the exit slit. Due to its double-focusing property, the CMA is able to refocus electrons of a large range of azimuthal entry angles at the exit slit. In the used CMA the inner cylinder is positioned at $r_i = 3$ cm and the outer cylinder at $r_o = 9$ cm with respect to the symmetry axis. The spectrometer constant

$$C_{\text{sp}} = \left(K \cdot \ln \left(\frac{r_o}{r_i} \right) \right)^{-1} = \left(0.763 \cdot \ln \left(\frac{9 \text{ cm}}{3 \text{ cm}} \right) \right)^{-1} = 1.19, \quad (4.1)$$

with the CMA coefficient $K = 0.763$ [124] for this CMA, reflects the geometrical properties of the assembly.

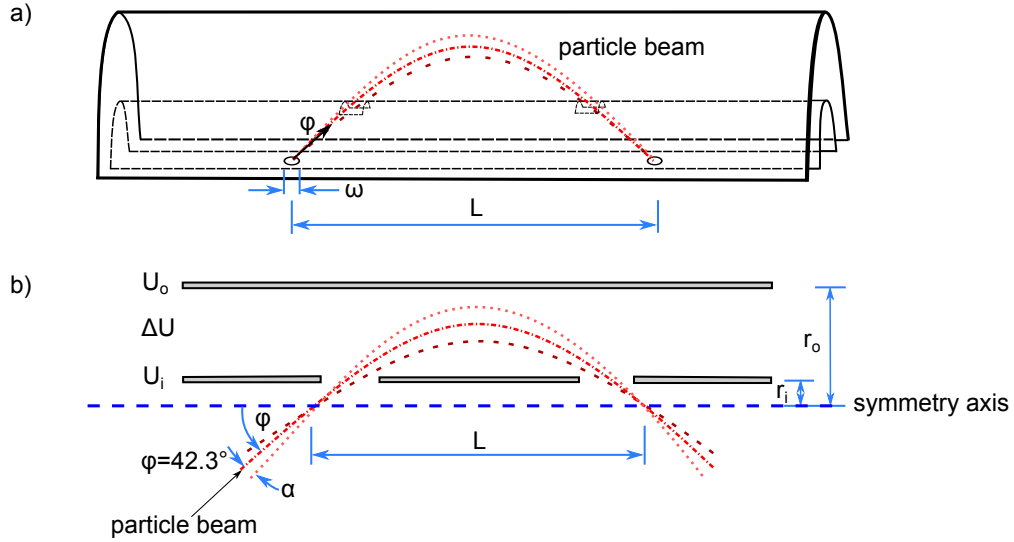


Figure 4.7: Schematic of the working principle of a CMA, adapted from [127]. a) The schematic visualizes the axial focusing of a CMA, when the entrance and exit slit are located on the symmetry axis. The width ω of the entrance/exit slits of the analyzer, the particle beam entrance angle ϕ and the distance L between the entrance and exit slit are indicated. b) Cross section through the CMA. The inner and outer radii r_i and r_o of the electrodes of the CMA are denoted, as well as α , the acceptance half angle of the analyzer in the dispersion plane, U_i and U_o , the inner and outer potentials and ΔU , the difference between them.

For dimensioning the CMA potentials, the following procedure has been used [127]:

1. Chose the desired energy passband ΔE , in this case $\Delta E = 11.2$ eV. The energy resolution $\Delta E/E_0$ relates the analyzer's energy passband ΔE with the pass energy E_0 , and can be determined via the so-called base resolution

4.2. Specifics and performance of the out-of-plane SEMPA setup

$\Delta E_B/E_0$. The base resolution is given by $\Delta E_B/E_0 = A \cdot \omega + B \cdot \alpha^n + C \cdot \beta^2$, with the coefficients $A = 2.2/L$, $B = 5.55$, $C = 0$, $n = 3$, and the angles α and β which describe the angular deviation of the electrons from the central path from the entrance to the exit slit in the deflection plane and in the plane perpendicular to it, respectively. Furthermore, the base resolution is connected to the energy passband via $\Delta E_B \approx 2 \cdot \Delta E$. For a CMA, β is always zero [127], and so is α in a first order approximation. Thus, with the length L between the entrance and exit slit of 188.2 mm and a slit width of $\omega = 3$ mm for the used CMA, it follows that $\Delta E_B/E_0 = 3.5\%$. The energy resolution equals thus $\Delta E/E_0 = 1.75\%$.

2. Determine the pass energy E_0 from the energy resolution of the CMA, in this case $E_0 = \Delta E/1.75\% = 640$ eV.
3. Assuming that the SE have an average kinetic energy of 3 eV, the potential of the inner electrode is $U_i = 1/e \cdot (E_0 - 3 \text{ eV}) = 637$ V.
4. The potential difference between the inner and the outer electrode ($\Delta U = U_i - U_o$) can be calculated by using the spectrometer constant C_{sp} (see Equation 4.1) via [127] $\Delta U = E_0/(e \cdot C_{sp}) = 640 \text{ eV}/(e \cdot 1.19) = 537.8$ V.
5. The potential of the outer electrode follows by $U_o = U_i - \Delta U = 637 \text{ V} - 537.8 \text{ V} = 99.2$ V.

Exit optics

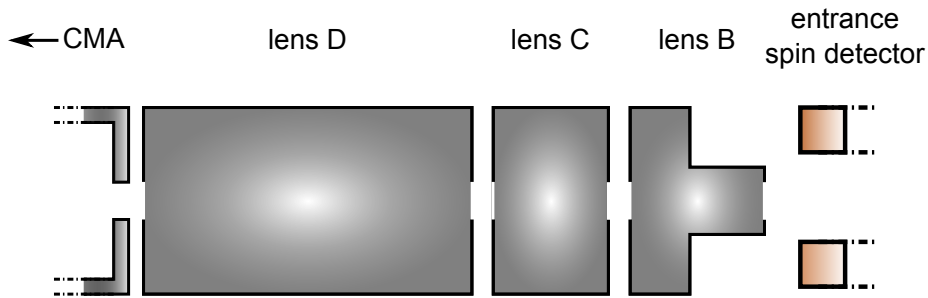


Figure 4.8: Schematic of the exit optics assembly. Consisting of three lenses, the exit optics transfers the SE beam towards the spin detector. The voltage applied to the first lens after the CMA is equal to the inner potential of the CMA. The last lens before the spin detector is on scattering potential, meaning on the same potential that is applied to the W(001) crystal, to allow a field-free diffraction.

After the SE leave the CMA through the exit slit, the electrons pass the exit optics composed of three lenses, as shown in Figure 4.8. The first lens after the CMA, for historical reasons labelled *lens D*, is in-situ connected to the potential of the inner electrode of the CMA. The second lens *C* is set to 300 V while the final lens *B* is on 102.4 V, which is the same as the scattering potential applied to the W(001) crystal. Lens *B* works as a drift tube and allows a field-free diffraction of the SE at the crystal.

4.2.4 Detection unit

After leaving the exit optics, the SE enter the spin detector shown in Figure 4.9. In the latter, the spin-dependent electron diffraction at W(001) takes place as described in Section 2.4.

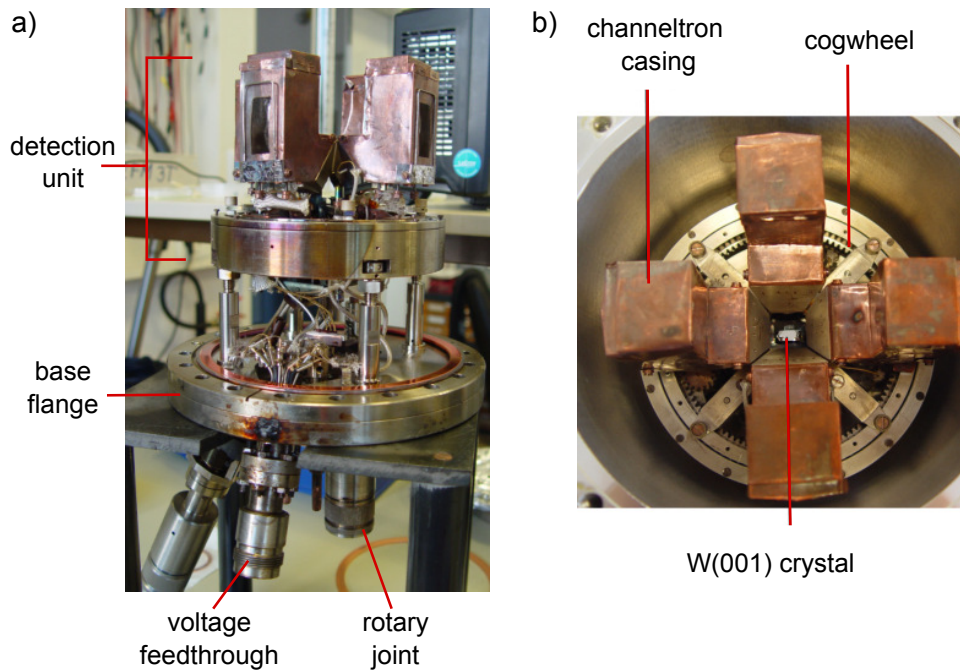


Figure 4.9: Photographs of the W(001)-based spin detector. a) Side view of the entire spin detector on its CF 160 flange. Below the base flange, a multipin voltage feedthrough and the rotary feedthrough for moving the gear wheel are visible. Between the flange and the detection unit, the cabling of the vacuum side can be seen. The cable lengths allow for a 90° rotation of the detection unit via the rotary feedthrough. On top of the gear wheel the W(001) crystal is surrounded by four channeltrons, housed each in a copper casing. b) The top view of the detector shows the W(001) crystal in the center of four channeltrons which are each surrounded by a copper casing. It also allows a view into the gear wheel that forms the base of the detection unit.

4.2. Specifics and performance of the out-of-plane SEMPA setup

The voltage feedthrough for potentials at the channeltrons and the cable management at its UHV side can be seen in Figure 4.9a) showing a side view of the detector. The MHV feedthroughs of the four detector channels are not visible in this angle of the photograph, but are located behind the indicated voltage feedthrough.

The detection unit was built onto a gear wheel that can be moved via a rotary feedthrough from the outside⁵. At the UHV side, the length of the wires between the CF-160 base flange and the detection unit allows for a 90° rotation of the latter. This cogwheel can be seen in Figure 4.9b) which provides a top view on the detector. Also the W(001) crystal which is surrounded by four copper-cased channeltrons is visible.

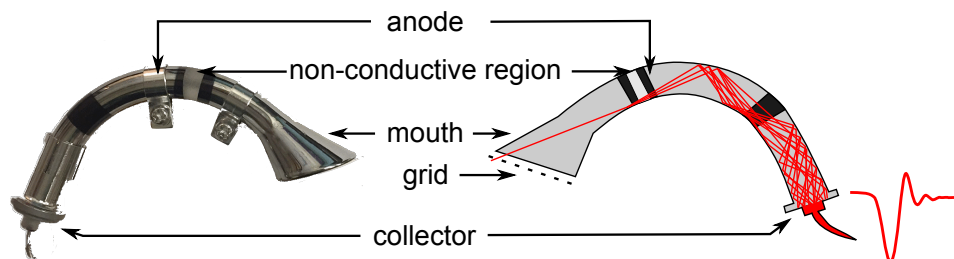


Figure 4.10: Photograph and scheme of a channeltron as used in the spin detector. Mouth and anode of the channeltron are separated by a non-conductive region, where the external coating of the glass tube has been removed. An internal electrical resistance in the order of 140-160 M Ω is present between mouth and anode. A retarding grid is mounted in front of the mouth to prevent low energetic SE which were created at the W(001) from entering. A voltage gradient between mouth and collector accelerates the incoming electrons towards the collector. The electron multiplication is indicated in the sketch on the right by red lines, showing their trajectories from the mouth towards the collector. The photograph on the left was adapted from [128].

In the following subsections, the optimization of the voltage-dependent detector performance will be presented and the handling of the W(001) crystal as well as its characteristics will be discussed. A scheme of one of the channeltrons used can be seen in Figure 4.10. A channeltron consists of a glass tube coated on the inside a semiconducting, high electron emissive material. Three electrical contacts allow applying an voltage gradient along the tube. Namely there are the mouth, which is the opening at the front, the anode in the middle of the tube and the collector at its end. A retarding grid is mounted in front of the mouth (see Section 4.2.5) to prevent SE which were created at the W(001) crystal

⁵This feature was implemented as a backup in order to be able to readjust the detector orientation in case of a possible false positioning.

from entering⁶. An electron entering the mouth will thus be accelerated towards the collector. On its way, the electron hits the inner coating and is due to its high kinetic energy able to induce the emission of about 1 to 3 electrons. The curvature of the channeltron ensures that all incident electrons, independent of their entry angle, collide with the inner channeltron coating. The resulting electron avalanche allows to amplify a single input electron to $\sim 10^7$ electrons at the collector. This electron multiplication is indicated by the red lines in the sketch in Figure 4.10.

4.2.5 Voltages at the channeltrons and signal processing

Before specifying the voltages used at the channeltrons, an overview on the signal processing is given as shown in Figure 4.11. In the schematic, *channeltron voltage* denotes the input high voltage (2 – 3 kV) to the decoupling circuit. An RC-low-pass filter blocks noise from the power supply from entering the pulse processing.

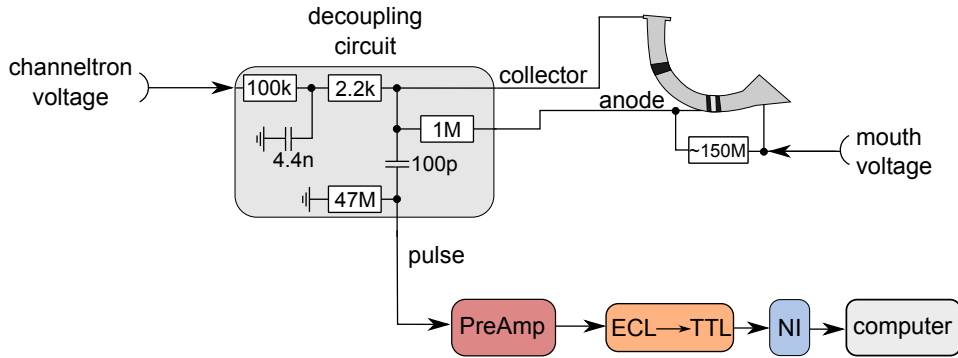


Figure 4.11: Schematic of the signal processing electronics. The decoupling circuit, into which the channeltron high voltage is inserted, generates the voltages for the collector and the anode of the channeltron. It also separates the detected avalanche pulses corresponding to a single electron hit at the channeltrons mouth from the high voltage. The following electronic devices discriminate and count the pulses with the help of an National Instruments (NI) TTL counting card. The mouth voltage is not generated from the channeltron voltage, but inserted separately. A resistance of roughly $(150 \pm 10) \text{ M}\Omega$ exists between anode and mouth.

The decoupling circuit generates the collector and anode voltages from the channeltron voltage with $U_{\text{collector}} > U_{\text{anode}}$ by forming a voltage divider versus the mouth voltage via the internal channeltron resistance. A 100 pF capacitor separates the current pulses, resulting from the amplified single-electron events, from

⁶The SE created at the W(001) crystal do not carry any spin information about the sample.

4.2. Specifics and performance of the out-of-plane SEMPA setup

the high voltages, before feeding them into separate electronic devices which amplify, discriminate and count the pulses. The pulse processing is done within a pre-amplifier (MIT, F100-E) which contains a linear amplifier and a discriminator. For the further data processing, the obtained emitter coupled logic (ECL) pulses from the pre-amplifiers are converted to transistor-transistor logic (TTL) allowing a readout via a National Instruments [129] card and a data processing in *LabView* [130].

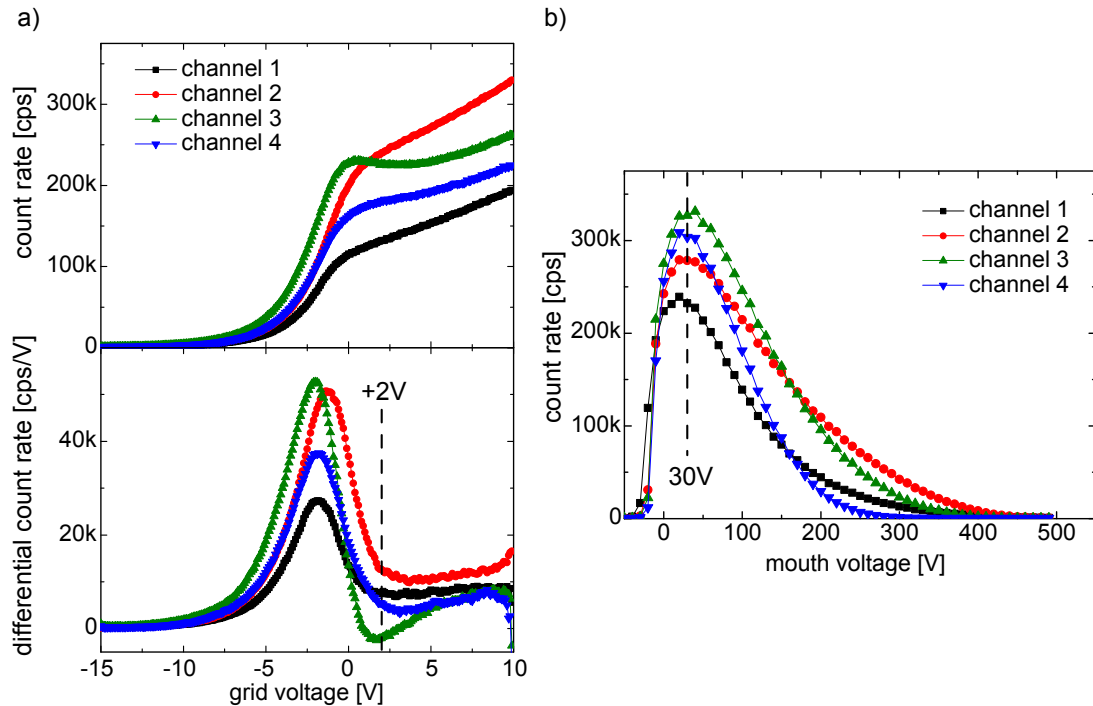


Figure 4.12: a) Grid scan: The upper panel shows the increasing count rates of the four channels in dependence of the voltage applied to the grids. The lower panel shows the differentiated count rate and visualizes that for grid voltages above 2 V the increase in the count rate does not originate anymore from the polarized SE of the sample. The additionally detected electrons at these grid voltages can be either scattered SE which lost energy during LEED or SE generated at the W(001) surface. While in the first case, the spin information might be altered due to multiple scattering, the SE described in the second case do definitely not carry any spin information of the sample. b) Mouth scan: The maximum of the count rate is found when a voltage of 30 V is applied to the mouth.

For each of the individual channeltron detectors, the optimum operation voltage needs to be determined to allow for the best possible measurement performance. The optimal working point differs among the devices due to aging effects as well as due to production tolerances. In the following, the potentials used for

the grids positioned in front of the channeltrons, the mouths as well as the channeltron voltages are derived. The voltages applied to the grids and the mouths are determined by performing *grid scans* and *mouth scans*, respectively. In these type of scans, the voltage is swept over a range that is meaningful for the element under test and the correspondingly obtained count rate is measured. The grids in front of the entrance of the channeltrons prevent that those polarized SE which experienced several scattering processes at the W(001) as well as SE generated at the W(001) surface enter the mouth. In the first case, the SE have an increased probability to not carry the correct spin polarization any longer. They loose energy with every collision and are thus observed as diffuse scattering in LEED. Detecting SE which underwent a spin-flip process together with the spin-polarized electrons from the sample leads to a decrease in the signal-to-noise ratio of the measurement, which should be avoided. In the second mentioned case of SE that were created at the W(001) crystal, no information on the sample magnetization is related to the spin of these electrons, and thus their detection is detrimental. The result of the grid scans, which were performed at a mouth voltage of 100 V and at a primary electron beam current of 3 nA, are shown in Figure 4.12a). The expected increase in the count rate with increasing voltage is observed, as seen in the upper graph. The lower plot shows the differentiated count rate in dependence of the grid voltage, indicating that beyond $U_{\text{grid}} = 2 \text{ V}$ no signal increase due to the SE from the sample, but only due to SE from the W(001) or diffuse scattered SE occurs. Thus, the grid voltage for all four detection paths has been set to 2 V.

A scan of the mouth voltage taken at an primary electron beam current of 3 nA and with a grid potential of 2 V is shown in Figure 4.12b). In contrast to the grid scan, a clear maximum in the count rate is found at 30 V for the mouth voltage. The form of the signal pulse exiting the channeltrons collector is shown in Figure 4.13a). This exemplary pulse was detected in channel 4 at a channeltron voltage of 2.2 kV. The pulse height of about -11 mV has a full width at half maximum of $\text{FWHM} = 10 \text{ ns}$ and shows only slight ringing. As mentioned above, aging of the channeltrons creates the need to adjust the applied operating voltages after prolonged use. This can be done by examining the pulse heights in dependence of the channeltron voltage, as seen in Figure 4.13b). The channeltron-voltage-dependent heights of channels 2, 3, and 4 show similar slopes and only a slight offset in respect to one another. Channel 1, on the other hand, shows a significantly different characteristic. Far higher voltages are needed to create pulses with comparable heights to the other channels and also a significant deviation of the slope is notable. Obviously, the aging process of channeltron 1 is further

4.2. Specifics and performance of the out-of-plane SEMPA setup

progressed than in the other three counters.

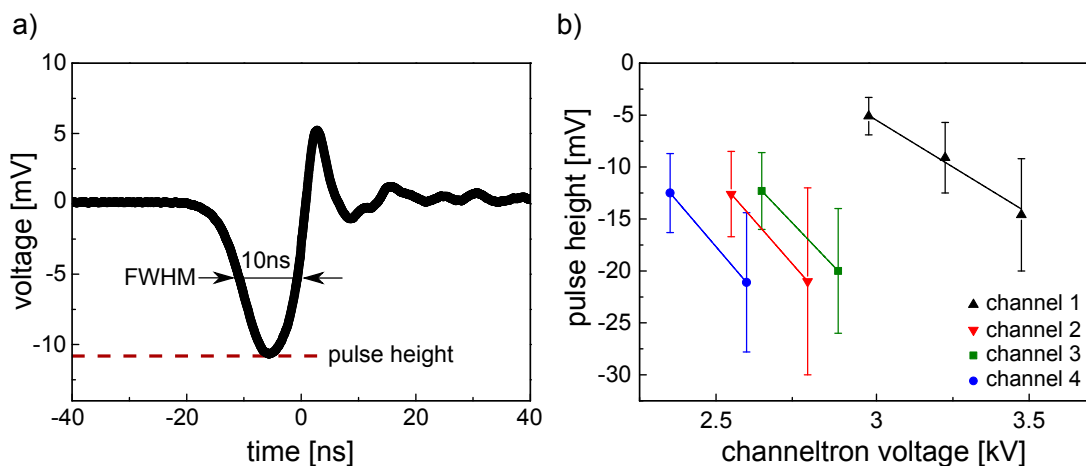


Figure 4.13: a) Unamplified typical channeltron pulse measured with an oscilloscope in channel 4 using a channeltron voltage of 2.2 kV. Slight ringing after the pulse is observed. The pulse height (minimum of the pulse) of ca -11 mV is marked with a dashed red line. b) Dependence of the pulse heights of the applied channeltron voltage. While the channels 2 – 4 exhibit a similar voltage behavior, channel 1 requires significantly higher voltages to obtain the same pulse heights. This deviation is ascribed to a further progressed aging process in this particular channeltron.

To finally determine the set of voltages applied at the four channeltrons, the count rate in dependence of the channeltron voltage is measured. Three regimes are expected in these kind of plot. At low channeltron voltages, the count rate increases with the voltage, as an increasing amount of pulses reach a pulse height which lies above the threshold voltage of the discriminator. At a certain voltage, a plateau in the count rate is reached as all electrons collected at the input of the channeltron produce a pulse which is detected by the discriminator. Only the pulse height/gain⁷ increases with the channeltron voltage in this regime. Finally, the plateau ends when the channeltron voltage is high enough to induce ion feedback⁸ due to the very high gain. Additionally, the increase in this regime can be superimposed by double counting of the incoming pulses, as also the amplitude of the ringing (see pulse in Fig. 4.13a)) is amplified.

These three regimes can be recognized in the plot in Figure 4.14 which shows the count rate in dependence of the channeltron voltage for all four channels.

⁷The gain defines the ratio of the output current to the input current.

⁸Ion feedback describes the phenomenon that gasses adsorbed at the inner surface of the channeltron are ionized and as a consequence produce SE. The gas ions are accelerated back to the entrance of the channeltron and gain enough energy to create SE when striking the inner coating.

The working points are chosen from the second regime which shows a plateau of the count rate in such a way so that the pulses from all channels have a pulse height of about 5.4 mV. These voltages are indicated in Figure 4.14 by dashed lines. Higher voltages would only cause faster aging of the channeltrons without giving more real counts.

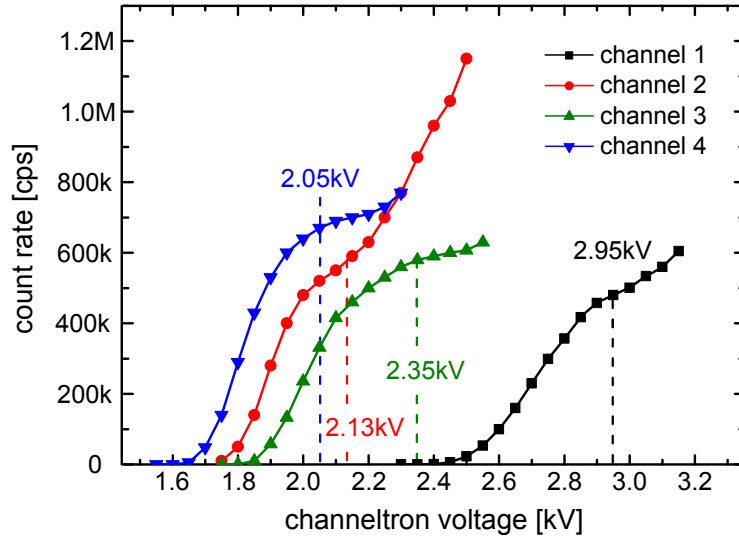


Figure 4.14: Count rate detected in all four channels in dependence of the applied channeltron voltage. The working points are chosen from the characteristic plateau region of the count rate at which all detectable SE are measured. For all channels, the determined working points are indicated by dashed lines.

4.2.6 Preparation of the W(001) crystal

The spin-dependent diffraction process requires a clean W(001) crystal surface, thus the crystal is cleaned regularly via flash heating. For flashing, a current running through the crystal is ramped up to a defined maximum value within 10s and afterwards held for 5s. Once a day (before the first measurement), a high-power flash up to ~ 2200 K is used to remove desorbed oxygen from the W(001) surface [23]. The high-power flash also removes carbon-monoxide contaminations, which desorb at $T \geq 1200$ K [23], as well as chemisorbed hydrogen at $T \geq 500$ K [131] from the crystal surface. A low-power flash up to ~ 1300 K, removing hydrogen and carbon-monoxide, is performed every 1–2 hours to maintain a clean surface and thus to ensure stable working conditions for SEMPA [132]. Furthermore, an automated oxygen cleaning cycle is used a few times per year to maintain the depletion of bulk-carbon contamination at the surface region. In this oxygen cleaning cycle, a partial pressure of $p_{\text{O}_2} = 5 \cdot 10^{-9}$ mbar is

4.2. Specifics and performance of the out-of-plane SEMPA setup

used and the crystal is flashed to ~ 1300 K (ramp up time 10 s, holding time 5 s) every 15 min for about 10 h. After this hot oxygen treatment, the remaining oxide layer is removed from the crystal surface by flashing up to 2200 K [23, 133].

4.2.7 Spatial resolution

In the light of future applications for this SEMPA instrument, it is desirable to achieve the highest possible spatial resolution. To determine the spatial resolution, a commercial test sample (Plano, S168U) of gold nanocrystals with sizes between 5 and 150 nm on a conductive carbon film of 2 mm thickness was used. An SE image of the gold nanocrystals taken at a primary electron current of 3 nA is shown in Figure 4.15a). The image is the sum of the intensities detected in the four channels of the spin detector. The Au crystals are clearly visible, show sharp edges and high contrast in respect to the underlying carbon film. The same Au crystals are shown in 4.15b), but the image has been taken with the so-called *crossover mode* mode of the SEM Gemini column, where the beam is focused in the aperture plane. This mode provides a primary-electron-beam current of up to 15 nA. The high current of this mode is appealing for the SEMPA technique as it allows to reduce the acquisition time⁹. As in this high-current mode the beam is not shaped by the aperture, a wider, non-round electron probe is created that unfortunately results in a decreased spatial resolution, see Figure 4.15b). The direct comparison of the images stresses the lower spatial resolution of the crossover mode resulting in a limited applicability in SEMPA.

Figure 4.15c) shows horizontal line profiles taken at 6 kV in the images with a primary current of 3 nA and in the crossover mode setting. The positions at which the line scans to determine the lateral resolution¹⁰ were taken are highlighted by a blue line in a) and by a green one in b). By fitting a Gaussian error function to the edges of the nanoparticles, the spatial resolution was derived. The width d of the error function, $f(x) = A \cdot \text{erf}((x - x_0)/d) + c$, relates to the resolution 2σ via $2\sigma = 2 \cdot d/\sqrt{2}$. For the 3 nA mode a width of $d_{3\text{nA}} = (11.5 \pm 0.4)$ nm is determined

⁹The acquisition time can not be reduced to any desired time by increasing the PE beam current, as the processing of high count rates is limited by the dead time of the used detector.

¹⁰As introduced in Section 4.2, the sample is tilted with respect to PE beam so that the surface normal of the sample and the incoming PE beam form an angle of 64°. While during SEMPA investigations a correction of this sample tilt is performed within the software of the SEM, the two SE images shown here have been taken purposely without a sample tilt correction. The lateral resolution is thus not identical to the longitudinal resolution of the magnetization images taken in SEMPA.

which correlates to a resolution of $2\sigma_{3\text{nA}} = (16.2 \pm 0.6)$ nm. In case of the crossover mode, $d_{\text{crossover}} = (29.4 \pm 1.2)$ nm and thus $2\sigma_{\text{crossover}} = (41.6 \pm 1.7)$ nm is found.

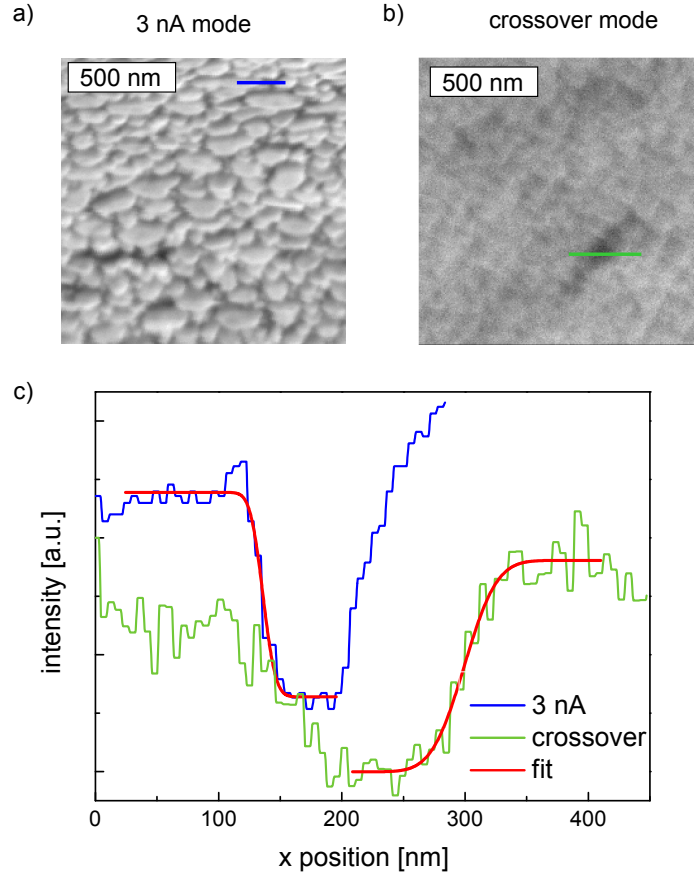


Figure 4.15: SE image of Au nanocrystals, obtained from the sum of the intensities of all four channels of the spin detector, taken at 6 kV and a) at an primary electron beam current of 3 nA, and b) in the crossover mode of the PE beam. c) Horizontal line profiles taken in a) and b) (positions highlighted in blue and green) are used to determine the lateral resolution. By fitting an error function to the edge of a gold particle, seen as red fits, a spatial resolution of $2\sigma_{3\text{nA}} = (16.2 \pm 0.6)$ nm was determined for the 3 nA mode and $2\sigma_{\text{crossover}} = (41.6 \pm 1.7)$ nm for the crossover mode.

4.2.8 Optimizing lateral image stability and minimizing signal noise

Reaching high spatial resolution requires extensive work regarding suppression of lateral image noise. The main effects contributing to this type of noise are mechanical vibrations, thermal drifts, electromagnetic interferences (EMI) and ground loops. Ground loops can lead to 50 Hz line-noise which couples into the primary electron beam of the SEM. A well-conceived grounding concept avoids

4.2. Specifics and performance of the out-of-plane SEMPA setup

these issues. Further information on grounding concepts can be found among others in references [134, 135]. A first measure to reduce electrical noise from radio frequency (RF) sources is to ensure proper shielding of the cabling at the setup, e.g. by using coaxial cables. Generally, all RF-sources can couple into the signals measured in the spin detector. Electrical cables conduct these noise currents and furthermore can radiate energy to—but also pick up energy from—their surroundings. In this way, cables serve as transmitter as well as receiver for EMI and are a significant noise source. Proper shielding attenuates such influences to an insignificant level. Nevertheless, a small amount of the noise might pass through the shield. Within the out-of-plane SEMPA setup, mostly coaxial cables are used providing already one inner shield. An additional metal wire sleeve is pulled over several cables and connected to ground.

The spin-detection arm is wrapped with μ -metal foil, a soft ferromagnetic material that is used for shielding against static or low-frequency magnetic fields. The magnetic shielding via μ -metal is based on leading the magnetic flux of external fields through the metal, and thus around the area that has to be shielded. Furthermore, the influence of slowly alternating magnetic fields from close by labs as well as DC fields is canceled via the usage of an active magnetic field compensation (Stefan Mayer Instruments, MR-3). The magnetic field probe, a fluxgate sensor, is attached to the setup detecting magnetic fields close to the SEM column. Large Helmholtz coils, incorporated in the lab walls, create the opposing field.

Mechanical disturbances originate from non-repetitive events like closing doors or footsteps¹¹, as well as from periodically induced vibrations from resonating setup components. The coupling of external floor vibrations to the SEMPA instrument is reduced via a passive air damping system (IDE, TNC-100). By using an acceleration sensor it was furthermore possible to identify other sources of mechanical vibration modes, which e.g. originated from the transfer rod. A support immobilizing the vibration of the transfer rod was constructed and damped the mechanical noise noticeably.

Repeatedly, image artefacts due to local charging of the sample interfered with the measurements, even while scanning conductive samples that were fixed by conductive adhesive tape to the metallic sample holder. An additional conductive graphite coat, which contacts the sample with the sample holder, as well as the the sample holder with the sample stage, was needed to obtain the required conductivity.

¹¹Footsteps are also an example for microphonics, which describes the characteristic of electrical components to transform acoustic noise into electrical noise.

4.2.9 Formation of the magnetization images

After introducing the individual parts and features of the out-of-plane SEMPA setup and explaining their functionality for the measurement process, the process of image formation itself is presented in the following. The process of the image formation in SEMPA is adapted from the one in a conventional SEM. For the data acquisition, the number of counts that have been detected in each channel-tron during the pixel dwell time is stored in a two dimensional array of cells. In these arrays, each cell corresponds to one of the positions scanned with the PE beam. While successively scanning over the sample surface from $(x_{\text{start}}, y_{\text{start}})$ to $(x_{\text{end}}, y_{\text{end}})$, the detected signals from all positions within the scanning area are, one-by-one, written into the corresponding cells of the array. This data storage takes place simultaneously for all four spin channels, resulting in four individual two-dimensional arrays. The size of the array is set before the measurement. Values for the x and y dimensions of the array are usually in the range of 100-500. Furthermore, the dwell time per pixel, which describes the measurement time at each (x,y) -position, is chosen between 5 and 50 ms. Each of the four arrays, corresponding to one spin channel, can be used to create a grayscale image, as seen in Figure 4.16 on the upper left. The magnetization images detected in the four channels show a magnetic domain pattern, as well as contrast due to topography. The upper row of the four images gives the two in-plane channels for the magnetization along the y-direction (vertical in-plane direction) and the lower row shows the two out-of-plane channels (perpendicular/ z-direction). Summing up all four channels leads to the conventional SE image seen at the lower left of Figure 4.16. No magnetic signal is visible, only the particles on the left part of the scanned area contribute to a change in the SE contrast. The upper right of Figure 4.16 shows the magnetic contrast along the y- and z-direction, determined from the raw data as described in Equation 2.3 (page 11). These two asymmetry images solely include the magnetic information without any topographic information. By color coding the magnetic information, the two asymmetry images can be reduced to one colored image. The color wheel shown in the lower right depicts the translation of color to magnetization direction. Yellow and blue represent the magnetization pointing to the positive and negative y-direction, respectively. In areas that are colored in red the magnetization points out of the paper plane (positive z-direction), in green areas into the paper plane (negative z-direction). With this color coding, spin-reorientation transitions as shown in Figure 4.16 can be visualized in one image, as well as the magnetization change at domain walls in systems with perpendicular magnetic anisotropy, at vortex structures or

4.2. Specifics and performance of the out-of-plane SEMPA setup

within skyrmions.

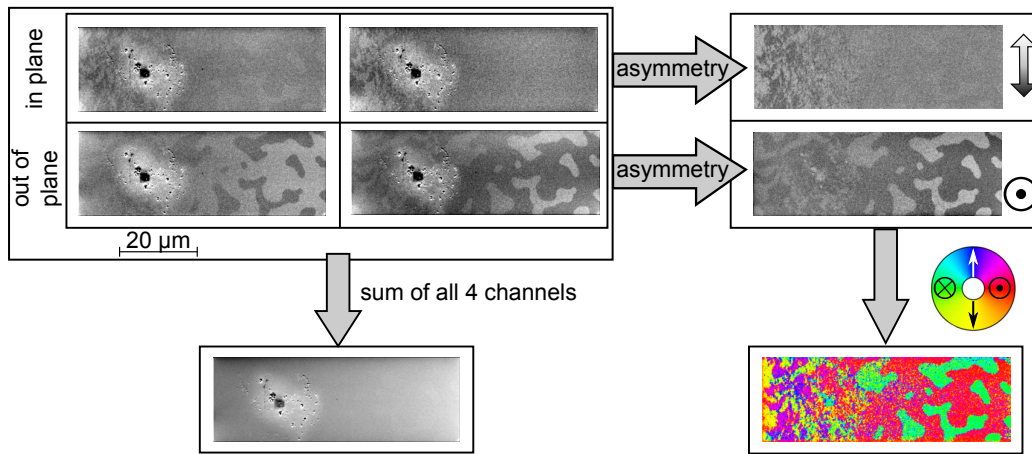


Figure 4.16: From the magnetization images detected in each spin channel, the conventional SE image can be generated by adding all four channels up. The magnetization information along the y- and z-direction is obtained by determining the asymmetry between the corresponding channels. Using the color wheel shown in the lower right allows to condense the information of the two asymmetry images in one color-coded one, where yellow and blue describe the direction of the y-component (vertical in-plane direction) and red and green the direction of the out-of-plane component of the magnetization.

New spin-detector design based on a pseudomorphic Au monolayer on Ir(001)

The concept of the spin-polarized LEED (SPLEED) detector presented in Section 2.4 has until now only been realized for a W(001) crystal. Possible opportunities of using other high- Z materials as spin analyzer in a SPLEED detector have not been explored yet. Fruitful discussions with Prof. Jürgen Kirschner about the studies of his group concerning low-energy electron diffraction from Au-passivated Ir(001) crystals [136, 137] lead to the idea of replacing the W(001) crystal of the LEED detector with an Ir(001) crystal that has a pseudomorphic monolayer (ML) of Au on top. Both materials, Au and Ir, are high- Z materials and are thus for themselves suitable candidates to replace the W(001) crystal. While Au provides the most inert metal surface for vacuum applications [36, 137], Ir is known for its ease of preparation in form of comparatively simple temperature treatments [137]. As Ir(001) as well as Au(001) have been found to be reconstructed in their thermodynamic equilibrium—with a (5×1) [137] and a $(5 \times n)$, $n = (26, 27, 28)$, pattern [138], respectively—they are less attractive for the usage in a SPLEED detector as precautions to avoid detecting beams from the reconstruction have to be taken.

In their search for a target for a spin-polarization detector that satisfies the desire of a high polarization sensitivity and a long lifetime in vacuum, the group of Prof. Kirschner considered epitaxial Au films on Ir(001). It was found that creating a pseudomorphic monolayer of Au onto the Ir(001) crystal results in an unreconstructed surface. This system indeed unites the advantages of both materials stated above, resulting in a target that is easily and reproducibly prepared [137]. Furthermore, it has been shown by Vasilyev *et al.* that in UHV the surface of the 1 ML Au/Ir(001) target has to be cleaned only every 6 months

[136], while the W(001) crystal needs a cleaning several times a day via flash heating (see Section 4.2.6).

In the first part of this chapter, the preliminary considerations concerning the scattering angles of the electrons after diffraction at Au/Ir(001) and the corresponding FOMs will be presented. The preparation procedure of the Au/Ir(001) target is described in the following and LEED images of first preparation trials are shown. The design of a new spin detector that is customized for the out-of-plane SEMPA setup and allows for the *in-situ* preparation of the Au/Ir(001) target, is introduced, before simulations on the needed electrode potentials as well as their effects on the trajectories of the spin-polarized electrons are presented.

After deriving a suitable working point and dimensioning the detector, the further steps were performed together with Maurice Pfeiffer who realized the implementation of the computer-aided design of the spin detector and performed simulations of the electron trajectories as part of his bachelor thesis [139].

5.1 Preliminary considerations

The first step of the design process for the new SPLEED detector is to derive the desired scattering potential, as it defines the scattering angle of the electron beam as well as the FOM. An initial study to determine the energy-dependent FOM of the (1,1) beams scattered at 1 ML Au/Ir(001) has been performed by Kirschner *et al.* [140] who forwarded the obtained data to our group. Evaluating this dataset revealed that two energy regimes, around 80 eV and 140 eV, of the (1,1) beams of the Au/Ir(001) target are highly appealing for the application in a LEED-based spin detector, as they provide a comparatively high FOM. A schematic of the experimental setup used by Kirschner *et al.* is given in Figure 5.1 showing the three

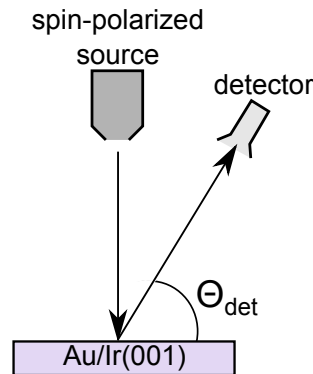


Figure 5.1: Sketch of the setup used by Kirschner *et al.* [140] to study the reflectivity R and the sensitivity S of a pseudomorphic Au ML on an Ir(001) crystal. The kinetic energy of the spin-polarized electrons created by a strained-layer photo cathode was varied at constant detector angle θ_{det} , and vice versa the detector was scanned through θ_{det} at fixed kinetic energies.

5.1. Preliminary considerations

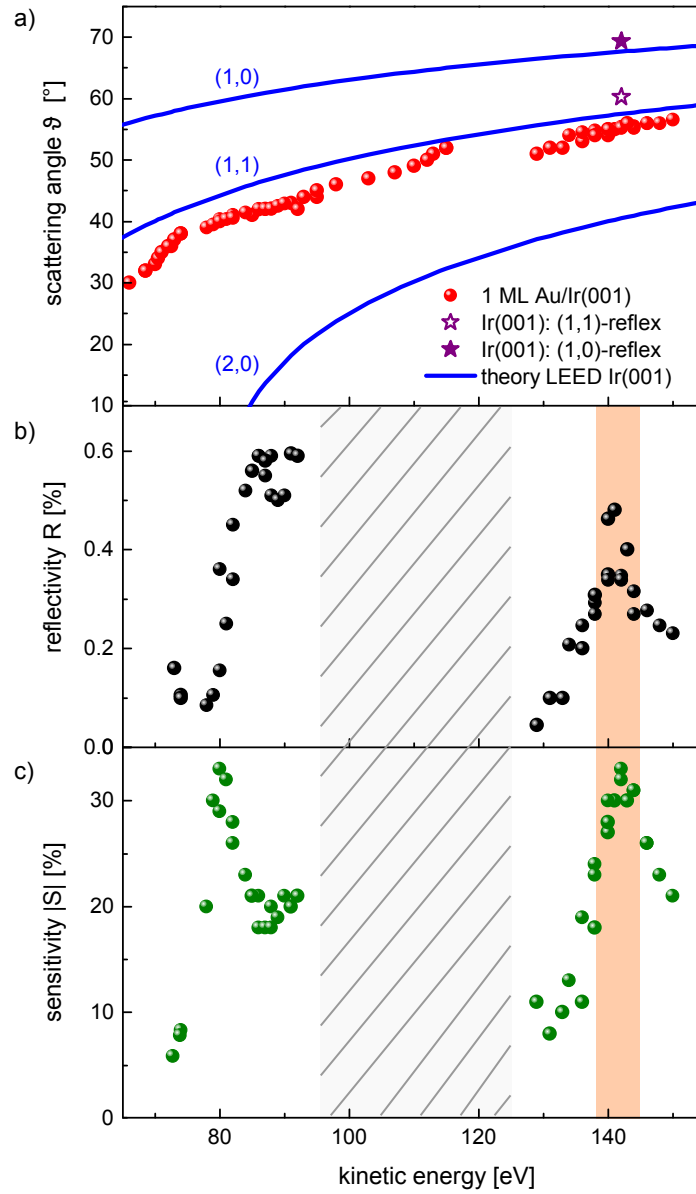


Figure 5.2: a) Energy-dependent scattering angles of the LEED beams measured on 1 pseudomorphic ML Au on Ir(001). The red spheres show the experimentally obtained scattering angles of the (1,1) beam, while the blue lines represent the theoretically derived energy-dependent scattering angles of the (1,0), (1,1) and (2,0) beams of Ir(001). Two scattering angles determined in the preparation chamber of the in-plane SEMPA on a clean Ir(001) crystal at 142 eV are shown as purple stars. b) The reflectivity R in dependence of the kinetic energy shows two broader maxima, one around 80 eV and the other around 140 eV. Only infrequent data points have been taken between 90 eV and 130 eV as a small sensitivity arises. The corresponding data are not shown here but the area is shaded in gray. c) The absolute value of the sensitivity $|S|$ in dependence of the kinetic energy shows a maximum at 80 eV that does not coincide with a maximum of the reflectivity. In contrast, the maximum of the reflectivity around 140 eV is accompanied with a maximum of $|S|$ promising a high FOM.

key features: a spin-polarized source (strained-layer photo cathode), a detector and the Au/Ir(001) target. By scanning the kinetic energy of the spin-polarized electrons through a certain range and keeping the detector at a fixed position as well as by—vice versa—changing the detector angle at a fixed kinetic energy of the electrons, the dataset connecting the information on the reflectivity R and the sensitivity S at a certain angle and energy has been obtained. The experimentally determined scattering angles ϑ of the (1,1)-LEED beam of 1 ML Au/Ir(001) are shown as red spheres over the energy range of 65 eV to 155 eV in Figure 5.2a). The theoretical angular dependence of the (1,0), (1,1) and (2,0)-LEED beams of Ir(001) is added as blue lines. These curves are easily derived via geometrical considerations of electron diffraction at a two dimensional lattice in real space¹ using the path difference of diffracted beams in case of constructive interference where $\cos(\vartheta) = \delta/\tilde{a}$ applies, see Figure 5.3a). The parameter \tilde{a} gives the distance to the next atom in the diffraction plane towards a certain lattice direction², see Figure 5.3b), while δ represents path difference equaling $n \cdot \lambda$, with n the order of diffraction and λ the energy-dependent wavelength of the electrons. The latter is defined by $\lambda = h/\sqrt{2m_e E_{\text{kin}}}$, with h the Planck constant, m_e the mass of an electron and E_{kin} its kinetic energy. Thus, the energy-dependent scattering angle is given via $\vartheta(E_{\text{kin}}) = \arccos(n h / (\tilde{a} \sqrt{2m_e E_{\text{kin}}}))$. The experimentally determined scattering angles for the pseudomorphic ML of Au on Ir(001), shown in red, lie slightly below the theoretically expected values for the (1,1) beam of Ir(001). To assess the significance of this deviation, the scattering angles of the (1,0) and (1,1) beams of a cleaned

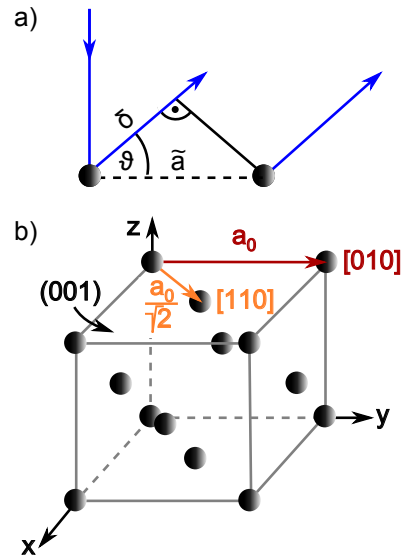


Figure 5.3: a) Sketch of the geometry of electron diffraction at a two dimensional lattice in real space. Explanation see text. b) Sketch of a face-centered cubic lattice as e.g. for Ir. The (001) plane as well as the [110] and the [010] directions are indicated, for the latter two the corresponding distances \tilde{a} to the next atom are given, a_0 being the lattice constant.

¹This nonlinear energy dependence of the scattering angles can analogously be derived in reciprocal space using the reciprocal lattice vectors and considering momentum transfer.

²For example, into [010] direction, \tilde{a} is equal to the lattice constant a_0 (for iridium $a_{\text{Ir}} = 3.84 \text{ \AA}$ at RT [141]). Into [110] direction, \tilde{a} is equal to $a_0/\sqrt{2}$.

5.2. Preparation of the Au/Ir(001) target

Ir(001) crystal were determined from a LEED image taken at $E_{\text{kin}} = 142 \text{ eV}$ in the preparation chamber of the in-plane SEMPA setup. The obtained angle positions are added to the plot as purple stars, revealing that they also deviate slightly from the theoretical values, but in opposite direction. Thus, the slight deviation can be treated as systematic reading error for each setup. Figure 5.2b) shows the reflectivity R for the energy areas around 80 eV and 140 eV³. Though the reflectivity reaches its global maximum around 80 eV, a broader maximum is observed around 140 eV. In contrast, the absolute value of the sensitivity $|S|$, shown in Figure 5.2c), shows two maxima with equivalent sensitivity of about 33%. Unfortunately, the sensitivity maximum at 80 eV does not coincide with the maximum in the reflectivity. The maximum of the sensitivity around 140 eV on the other hand is positioned at the same energy as the one of the reflectivity, and has been highlighted in orange in Figure 5.2b) and c). At 142 eV, a FOM of at least $6.3 \cdot 10^{-4}$ can be expected ($|S| \approx 30\%$ and $R \approx 0.35\%$), which is four times higher⁴ than the one for W(001) of $1.6 \cdot 10^{-4}$ [117].

5.2 Preparation of the Au/Ir(001) target

In parallel to implementing the new detector design in a CAD (computer-aided design) software (see Section 5.3), an Ir(001) single crystal has been transferred into the preparation chamber of the in-plane SEMPA setup (see Section 4.1) for initial surface cleaning, and to test the procedure to create a single monolayer of Au on its surface. The customized shape of the crystal is seen in Figure 5.4. A 3 mm wide side nose on the otherwise circular crystal geometry allows clamping to a sample holder plate. The crystal was mounted onto a commercial sample holder (Omicron sample plate, Scienta Omicron) made of molybdenum that has a hole with a diameter of about 5 mm in its center. The circular area of the crystal was positioned in front of the hole so that its back can be bombarded with electrons from the electron-beam heater of the preparation chamber. Three tantalum strips, seen in red in Figure 5.4, have been spot welded in place to fix the crystal on the sample holder.

As the Ir(001) crystal was newly purchased, an initial profound surface cleaning was performed. The applied cleaning procedure consists of three steps and is

³Only infrequent data points have been taken in the energy range between 90 eV and 130 eV as in this regime the sensitivity is close to zero, making this regime unattractive for SPLEED. The data are not shown here but the area is grayed out.

⁴In the highlighted range in Figure 5.2 from 138 eV to 146 eV, the FOM increases from $3.3 \cdot 10^{-4}$ up to $8.6 \cdot 10^{-4}$ before it decreases down to $3.8 \cdot 10^{-4}$.

Chapter 5. New spin-detector design based on a pseudomorphic Au monolayer on Ir(001)

adapted from the instructions given in reference [136]. During this flash-heating procedure, the temperature at the crystal was monitored with a pyrometer (Iacon Ultimax UX-20P). First, the Ir(001) crystal is heated up to 1200°C to remove adsorbates, like H or CO, from its surface. However, carbon impurities cannot be removed with this step.

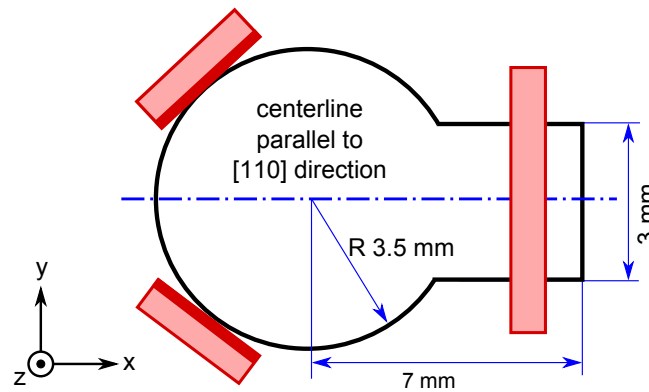


Figure 5.4: Dimensions of the circular Ir(001) crystal with a mounting nose. The crystal was fixed onto an omicron holder with tantalum strips, shown in red. While the right strip is simply spot-welded on each side of the crystal nose, the two on the left are L-shaped (going in z-direction, indicated by a dark red) to immobilize the crystal.

In a second step, cyclic heating up to 1000°C in an oxygen atmosphere of $2 \cdot 10^{-8}$ mbar was performed. The heating duration equals 21 s at an emission current of $I_E = 13$ mA and a voltage of $U = 1.25$ kV, while the cool-down time was set to 5 min. The oxygen reacts with carbon at the surface to CO that desorbs from the surface at this heating temperature. Due to the increased temperature, carbon impurities that are located underneath the surface move to the surface and are removed during the current or the following heating cycle. This cyclic heating leads to a carbon depletion and was performed for several days as the crystal was newly purchased. In contrast, a crystal that has already undergone the initial carbon depletion and solely shows surface contaminations requires only a cyclic cleaning duration of 15 – 20 min [136].

In the final step, the crystal is flashed in the absence of oxygen up to 1200°C to remove the remaining oxide layer from the crystal surface. By checking the surface quality via LEED the need for a repetition of the cleaning steps can be determined. When a (5x1) reconstruction with sharp spots is visible, the surface of the Ir(001) crystal is clean and well-ordered as seen in Figure 5.5a). After preparing a clean Ir(001) surface, about 1 nm Au is evaporated from a

5.2. Preparation of the Au/Ir(001) target

crucible at a rate⁵ of about 0.2 nm/min. According to literature [136], the sharp LEED pattern fades away after depositing 1 – 3 monolayers of Au, leaving only a fuzzy (1x1) structure. Repeated flashing up to 860°C is supposed to remove all but the first, pseudomorphic Au monolayer, which leads to the observation of a (1x1) pattern in LEED that is indistinguishable from the (1x1) pattern of the unreconstructed Ir(001) crystal. The pseudomorphic monolayer itself desorbs at temperatures above 900°C [137].

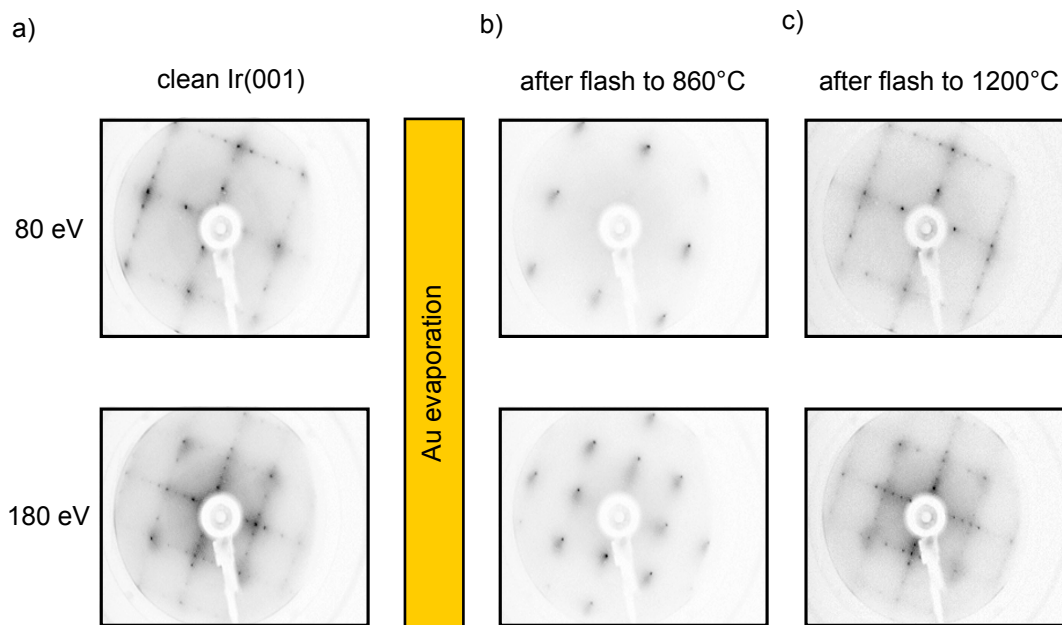


Figure 5.5: LEED images at 80 eV and 180 eV after cleaning and applying the processing steps to create the pseudomorphic monolayer of Au on Ir(001). The LEED images of the clean Ir(001) crystal with its (5x1) pattern are shown in a). Directly after evaporation of about 1 nm Au, only a diffuse LEED pattern without distinct spots is observed (not shown). After flash heating the crystal a few times up to 860°C, a (1x1) pattern with a blurry background is observed as shown in b). Flashing afterwards to 1200°C re-establishes the (5x1) pattern of the clean, reconstructed Ir(001) crystal as seen in c).

First tests of applying this procedure to create the pseudomorphic monolayer on the Ir(001) crystal have been performed in the preparation chamber right after the initial cleaning. The LEED images taken after depositing about 1 nm of Au onto Ir(001) and heating the Au/Ir(001) target several times up to about 860°C, seen in Figure 5.5b), indeed show the (1x1) pattern of the unreconstructed Ir(001), but with a blurry background around these spots. The LEED image

⁵Used parameters: $U = 900$ V, $I_{\text{filament}} = 1.7$ A, $I_{\text{emission}} = 22$ mA, flux = 11 mA

suggests that the heating procedure did not result in a perfect pseudomorphic monolayer. A few heating cycles up to about 1200°C were sufficient to make the (5x1) reconstruction of the clean Ir(001) visible again, see Figure 5.5c).

5.3 Detector design

Designing the Au/Ir(001)-based spin detector requires to take spatial constraints due to the dimensions of the detector chamber of the out-of-plane SEMPA, shown in Figure 5.6, into account. The 160 CF flange, on which the W(001)-based spin detector is mounted at present, provides a conveniently large base area for construction. A 40 CF flange, seen in the lower part of the sketch, is used as observation window providing a view onto the spin detector (not shown in the sketch) and the W(001) crystal. The currently used position of the W(001) crystal is indicated by a red bar.

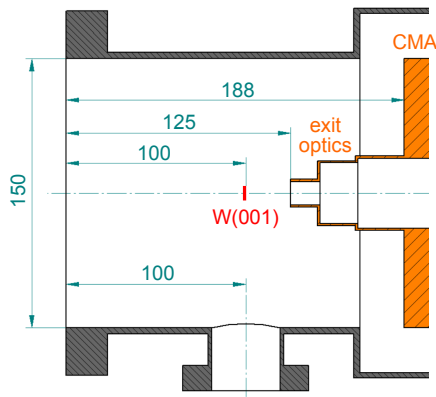


Figure 5.6: Relevant dimensions (turquoise, in mm) of the spin-detector arm at the position of the spin detector. The 160 CF base flange is seen on the left while a 40 CF flange in the lower part of the sketch provides an observation window with view onto the detector and the W(001) crystal. The three lenses of the exit optics and the end of the CMA are shown on the right, highlighted in orange. The position of the W(001) crystal in front of the exit optics is represented by a red bar.

On the right, the exit optics and a small part of the CMA (see Section 4.2 for setup details) are shown in orange, defining the space limitations opposite of the base flange. As the chamber has to undergo a bake out procedure to obtain UHV after venting the setup, e.g. for maintenance, the materials used for the construction of the spin detector are chosen to withstand temperatures up to at least 150°C without degassing or material fatigue. Namely, the flanges are made of non-magnetic steel 1.4429 (AISI 316 LN) and all other components are built of tantalum, Macor⁶, molybdenum, or titanium grade II.

The final spin-detector design is shown in Figure 5.7a). The 160 CF flange

⁶MACOR® is a machinable glass ceramic material. For ease of readability, "MACOR®" will be written as "Macor" within this thesis.

5.3. Detector design

is seen in the center, separating the parts on the air side including a linear feedthrough as well as rotary and electrical feedthroughs on the left from the UHV setup for measuring and preparing the Au/Ir(001) crystal, which is seen on the right. Figure 5.7b) shows a close up of the arrangement of the UHV components. Due to deactivating the display of internal features like shutters, the three key components of the detector are visible: the movable crystal-holder tube, the Au evaporator and the detection unit. In the following, these individual parts will be introduced in detail.

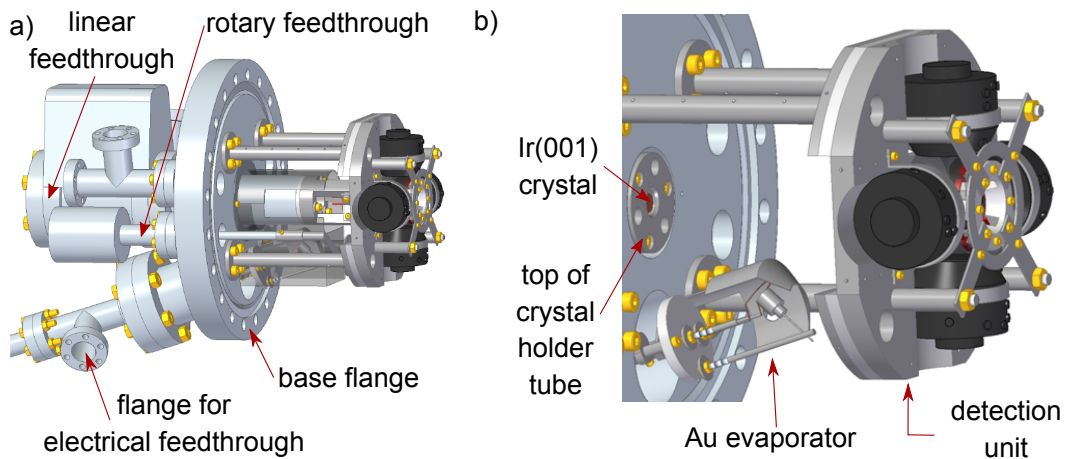


Figure 5.7: a) Overview of the final spin-detector design. On the left, the parts at the air side like e.g. linear feedthrough, flanges for electrical feedthroughs and rotary feedthrough can be seen. On the right of the base flange the components on the UHV side of the detector are visible. b) Zoom in on the UHV part of the detector (with deactivated display for several shutters) revealing the three key features: the movable crystal-holder tube (here in its retracted position), the Au evaporator and the detection unit.

5.3.1 Crystal-holder tube

The crystal-holder tube, shown in Figure 5.8a), is mounted on a linear feedthrough which allows to move the Ir(001) crystal from the preparation position (tube retracted) to the measurement position (tube inserted). To take in the preparation position, the crystal-holder tube is retracted so that the Ir(001) levels with the base flange, as seen in Figure 5.7b). In contrast, when moved into the measurement position, the top of the crystal holder tube will get in contact with the base plate of the detection unit.

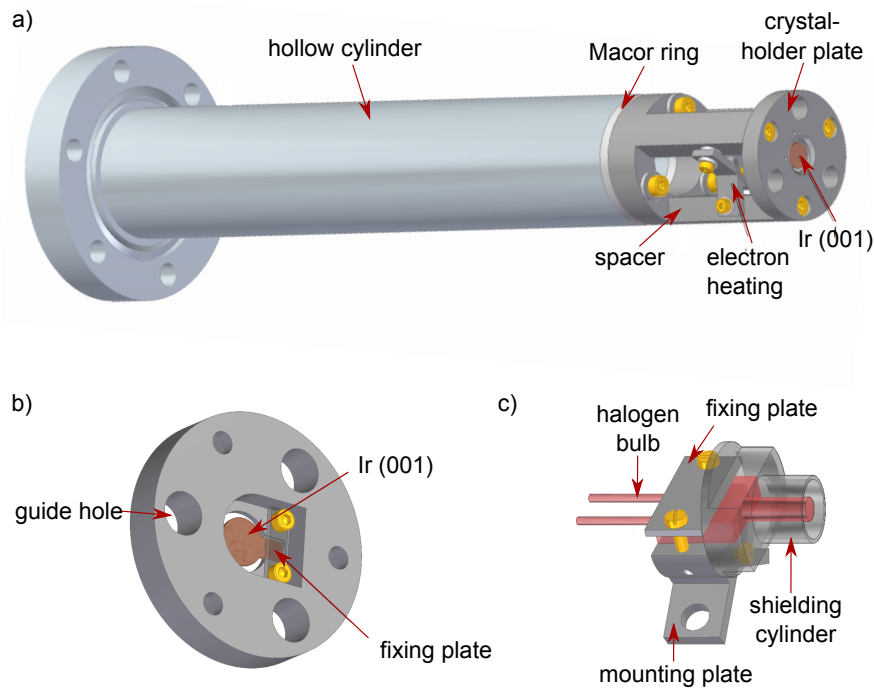


Figure 5.8: a) The crystal-holder tube: Within the hollow cylinder, which ends in a 40 CF base flange, run wires for the electrical connection of the crystal-holder plate and the electron-beam heating. The electron-beam heating unit is mounted via a plate onto a spacer that is electrically insulated from the hollow cylinder via a Macor ring. The crystal holder plate is mounted on top of the spacer, so that the Ir(001) crystal can be cleaned by flash heating via electron bombardment from its rear side. b) The crystal-holder plate: The Ir(001) crystal is positioned in the center of the circular crystal-holder plate. Three guide holes guide the crystal-holder tube to the precisely defined measurement position in front of the detection unit by means of three matching guide cones at its base plate. c) Electron heating: A halogen bulb with a bared axial filament is fixed between two plates. The lower plate allows mounting the bulb at the spacer. Adding ceramic washers between the mounting plate and the spacer results in an electric insulation of the electron heater. A shielding cylinder is added around the filament to focus the emitted electrons towards the Ir(001) crystal; respectively to prevent them from being attracted to the spacer or the crystal-holder plate as they lie at the same potential as the crystal.

The crystal-holder tube itself is composed of a hollow cylinder on an 40 CF base flange, an isolation ring made of Macor, a spacer which holds an electron-beam heating device, and the crystal holder plate to which the Ir(001) crystal is fixed. The Macor ring isolates the ground potential of the hollow cylinder from the potential of the crystal, which is also present at the crystal holder plate and the spacer.

5.3. Detector design

The front plate of the crystal-holder is shown in Figure 5.8b), where the Ir(001) crystal is clamped in position via a plate on its side nose. Three guide holes are used to guide the crystal-holder tube into the correct measurement position with the help of three cones mounted at the bottom side of the detection unit. Figure 5.8c) shows the construction for the electron-beam heating device, which is electrically insulated from the spacer by ceramic washers. A 50 W halogen bulb with a bared axial filament, which is surrounded by a shielding cylinder for focusing the emitted electrons onto the Ir(001), is fixed by a mounting plate onto the spacer behind the crystal-holder plate.

The shielding cylinder is needed, as not only the crystal but also the crystal-holder tube and the spacer are on crystal potential. The emitted electrons would thus not only be attracted to the crystal. A separate voltage can be applied to the shielding cylinder via a 16 CF feedthrough to control the repelling potential. Alternatively, it is possible to connect a pin of the halogen bulb with the shielding cylinder.

5.3.2 Detection unit

The detection unit, shown in Figure 5.9a), forms the heart of the spin-detection process. A Macor ring is positioned on top of the base metal ring that is used to connect the detection unit to the 160 CF base flange via four standoffs (see Figure 5.7). The Macor ring separates the electric potential of the holding plate for the detection cones from the ground potential of the 160 CF base flange. Four detection cones, which contain MCPs in a chevron stacking for the detection of the spin-polarized electrons, are fixed on the holding plate by retaining brackets. Indentations for the cones in the holding plate allow their precise positioning as well as a simplified dismount for maintenance by loosening the retaining brackets and pulling the cones backwards. Small threaded holes in the holding plate have been added for cable routing. These threaded holes are equipped with venting holes to prevent the creation of virtual leaks in the UHV. The large holes visible in the holding plate right in front of the spacer tubes fulfill the same purpose, as the standoffs between the detection unit and the base flange are screwed into the base metal ring⁷. The deflecting optics, seen in the center of the detection unit, is used to bend the trajectory of the electrons, which undergo LEED on the Au/Ir(001) target, into the cones. Such a deflection is not needed in the W(001)-based LEED detector.

⁷Consistently, also the Macor ring provides holes at these positions.

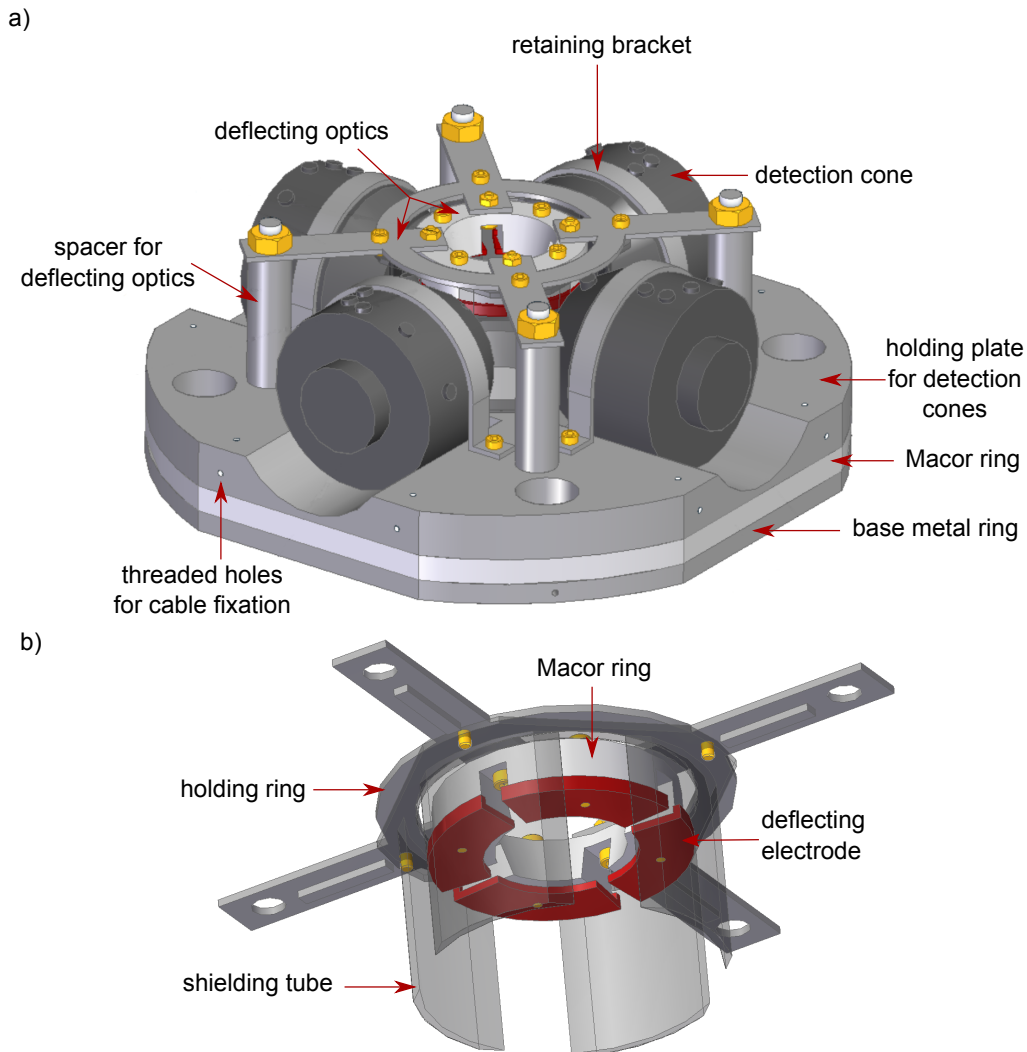


Figure 5.9: a) Assembly of the detection unit. Its base consists of a base metal ring, a Macor ring and a holding plate for the detection cones. Threaded holes in the base metal and the holding plate provide possibilities for cable fixation. The detection cones sit in indentations in which they are fixed via retaining brackets. The top part of the deflecting optics can be seen above the detection cones. b) Assembly of the deflecting optics. The four deflection electrodes are isolated from the holding ring by a Macor ring as well as the shielding tube which closes the gaps between the cones and is on the same potential as the outer shell of the cones.

Instead, the detection cones are positioned according to the scattering angle of the (2,0)-electron beams. The diffracted electrons thus enter the entrances of the cones directly without further deflection potentials. This scheme could not be adopted for the Au/Ir(001)-based detector due to the scattering angle of 57° at 142 eV (see Figure 5.2). Positioning the cones under this angle would make

5.3. Detector design

it necessary to mount them further away, near to the first lens of the exit optics after the CMA (see Figure 5.6), as the cones would—if positioned closer to the Ir(001) crystal—collide with the lenses of the exit optics.

Locating the cones next to the first lens of the exit optics results in a comparatively large distance between the Ir(001) crystal and the entrance of the detection cones of about 45 mm, and reduces thus the angular acceptance, leading to a decrease of the measurement signal. By mounting the detection cones with their openings perpendicular to the normal of the Ir(001) crystal and applying an electric field for deflection, the length of the electron flight trajectory is reduced to about 10 mm.

Simulations of the trajectories of the electrons, presented in Section 5.4, allowed to derive the potentials applied at the various components of the detector. For each of the four cones, the potential of the corresponding deflection electrode, seen in Figure 5.9b) in red, can be adjusted separately as they are not electrically connected. Thus, the count rates of the four channels can be optimized separately. Figure 5.9b) shows, besides the four electrodes seen in red, the Macor ring which insulates the potential of the electrodes from the potential of the cone plate. The shielding tube closes the gaps between the cones, leading to a homogeneous electric field seen by the diffracted electrons.

5.3.3 Au evaporator

In the first step of the preparation of the pseudomorphic monolayer of Au on top of the already cleaned Ir(001) crystal, Au is evaporated from the crucible shown in Figure 5.10. Two rods that are fixed via threaded holes on the CF 40 base flange serve as standoffs for the evaporator construction. Threaded holes along these rods provide the possibility for cable routing. A Macor plate separates the ground potential of the standoffs from the potentials at the evaporator and serves as the base for the construction of the evaporator. A crucible, whose inside is covered with a Au film⁸, is fixed on a standoff rod under an angle so that the opening of the crucible points onto the surface of the Ir(001) crystal (retracted position of the crystal-holder tube).

Two tantalum rods on top of the Macor plate are used as filament holders. This tungsten filament is bent around the front of the crucible. Electrons emitted

⁸The Au coating of the crucible has been achieved by using an electron-beam physical vapor deposition setup. A few Au pellets were inserted into the crucible and then mounted in a high-vacuum chamber. There, the pellets in the crucible were bombarded with an electron beam until they melted and wetted the inner surface of the crucible.

Chapter 5. New spin-detector design based on a pseudomorphic Au monolayer on Ir(001)

from the hot filament are accelerated towards the crucible, which is held at high positive voltage, and thus heat the crucible resulting in Au evaporation. In case the Au supply is exhausted, the evaporator can be removed for maintenance via the CF 40 flange without removing the whole detector. A semicircular shutter in front of the crucible prevents the unwanted deposition of Au on surrounding components during evaporation. The shutter is moved via a rotary feedthrough, and is provided with a hole which is aligned during evaporation with the opening of the crucible that points onto the Ir(001) surface. The shutter positions can be adjusted with two eccentric cam lobes that are mounted on the standoff rods and are used as limit stops.

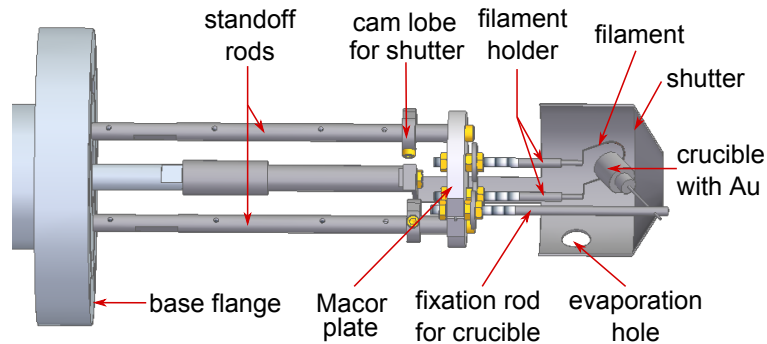


Figure 5.10: The Au evaporator is constructed onto a CF 40 base flange. Two rods are used as standoffs, on top of which a Macor plate is mounted. Two small rods on top of the Macor plate hold the filament that is bent around the front of a crucible. The crucible, whose inside is covered with a thin Au layer, is held by a third small rod that is mounted onto the Macor plate. The shutter, which is operated via a rotary feedthrough on the base flange is equipped with an evaporation hole. For preparation of the Au monolayer, the hole in the shutter is aligned with the opening of the crucible, which points onto the Ir(001) surface.

5.3.4 Assembly

After having introduced the three main components of the newly designed spin detector, namely the crystal-holder tube, the detection unit and the Au evaporator, some details concerning the assembly will be given in the following. The detector is mounted on a CF 160 flange that is equipped with four CF 16 and two CF 40 flanges. One of the CF 40 flanges is located in the center of the CF 160 base flange and holds the crystal-holder tube on a linear feedthrough. The second CF 40 flange is used for the Au evaporator and is mounted slightly tilted at the outer part of the CF 160 flange. This modularization allows a convenient

5.4. Field and electron-trajectory simulations

maintenance, as only the desired part and not the whole spin detector has to be removed. Furthermore, after removal, the flanges can be reclosed fast and the chamber can be pumped to sufficient vacuum to protect the hydrophilic MCPs inside the detection cones from atmospheric humidity.

Three of the four CF 16 flanges are used for electrical feedthroughs, while the fourth one holds a rotary feedthrough to operate a shutter. This shutter protects the opening in the center of the detection unit when the crystal-holder tube is retracted. The shutter prevents Au that desorbs during the flash cleaning of the Ir(001) crystal from flying into the detection unit and from metalizing the insulating Macor components. To make sure that also the inside of the detector is protected against unwanted Au coating originating from the evaporator, a thin metal shield is fixed on the CF 160 base flange. It separates the inner part where the crystal-holder tube is positioned from the outer part with the detection unit, its holding rods and its cabling.

5.4 Field and electron-trajectory simulations

Simulations have been performed with SIMION [142] to determine the optimum geometry and the required potentials inside the spin detector. SIMION is a software designed to calculate electrostatic fields as well as trajectories of charged particles within these fields. No magnetic fields have been considered within the simulations, as due to the choice of materials used in the spin detector the resulting magnetic fields are negligible. Figure 5.11 shows a comparison of the CAD drawing and the geometry modeled in SIMION of the center of the spin detector at measurement position (crystal-holder tube completely inserted). In the CAD drawing in Figure 5.11a), the Au/Ir(001) target (green) on the left is embedded in the crystal-holder plate (blue). The latter is snapped into the measurement position by making contact to the cone-holding plate (purple) on whose bottom three guide cones (yellow) are mounted. Those guide cones align, by gliding into the guide holes of the crystal-holder plate (blue), the crystal position with respect to the exit optics. The deflection plates, seen in red, are aligned with the exit of the last lens of the exit optics (orange). The same parts as shown in the CAD drawing are found in the modeled geometry of the SIMION simulation, seen in Figure 5.11b). The red lines visualize the equipotential lines of the derived potentials within the spin detector.

After diffraction at the Au/Ir(001) target, the LEED electrons are deflected into the detection cones via the deflection plates whose potential is at -270 V. Two grids are positioned in the opening of the detection cones to prevent SE that

Chapter 5. New spin-detector design based on a pseudomorphic Au monolayer on Ir(001)

have been created at the opening of the detection cone from entering. The first grid is at the same potential as the crystal (+142 V), while the second grid is at a slightly lower potential (+121 V).

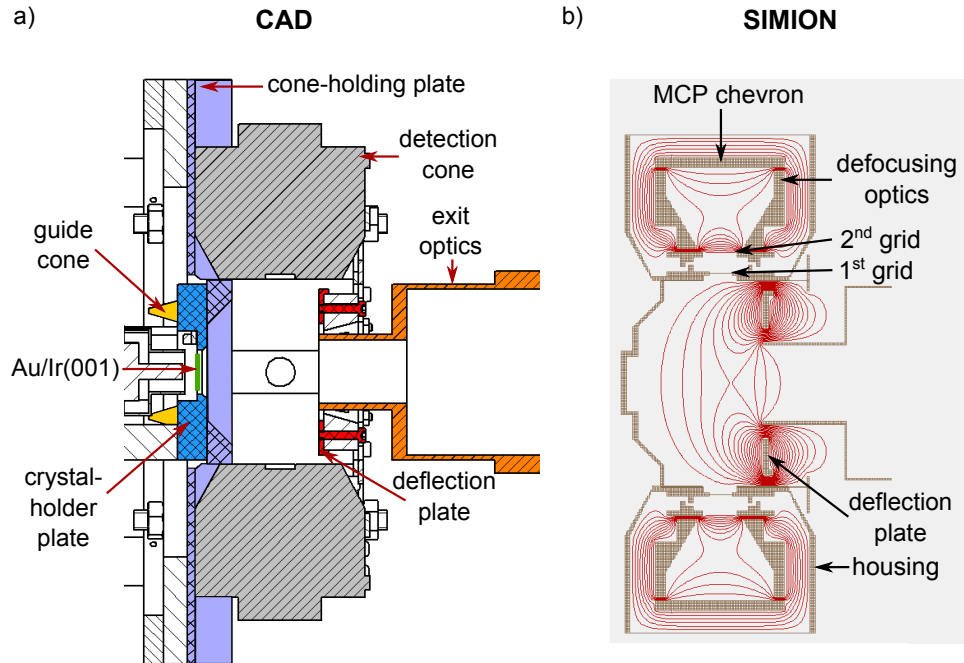


Figure 5.11: Comparison of the CAD drawing and the geometry used in the SIMION simulation. a) Cross section of the CAD drawing of the spin detector. It was used as template for modeling the geometry of the SIMION simulation. For clarity and orientation, several parts are highlighted or labelled: exit optics (orange), deflection plate (red), Au/Ir(001) target, crystal-holder plate (blue), guide cones (yellow), cone-holding plate (purple), detection cones (gray, without inner components). b) Analogous, the cross section of the modeled geometry in the SIMION simulation with equipotential lines of the determined potentials in the detector, shown in red. In front of the opening of the detection cones two grids are mounted to prevent SE created at the entrance of the detection cone from entering. A defocusing optics in front of the chevron stacked MCPs inside the detection cone broadens the entering diffracted electron beam and ensures a homogeneous wear of the micro channels.

In order to increase the transmission of the spin-polarized electrons that have undergone LEED at the Au/Ir(001) target these two grids can be removed, though one has to keep in mind that this change allows also some SE created at the entrance of the cone to enter. Behind the grids, a conical defocusing electrode at a potential of +1500 V is used to widen the electron beam. The dual-MCP stack at the rear of the detection cone is arranged in a chevron configuration, and its front face is put to +900 V to attract the electrons. Due to the defocus-

5.4. Field and electron-trajectory simulations

ing optics, the MCPs are illuminated more homogeneously preventing a strongly inhomogeneous wear of the micro channels. The detection cones themselves are surrounded by a housing which is at crystal potential.

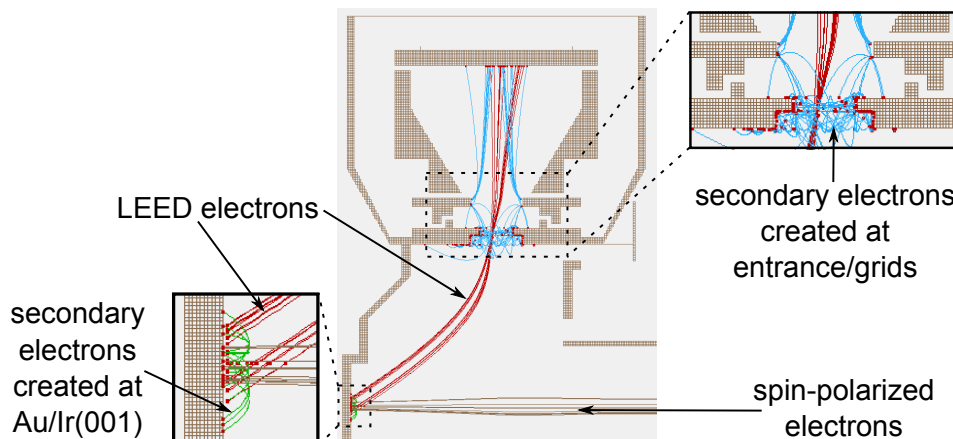


Figure 5.12: Simulation of the flight trajectory of the spin-polarized electrons. The spin-polarized SE (brown trajectories) diffract at normal incidence at the Au/Ir(001) target and fly under 57° towards the detection cone (red trajectories, labelled as LEED electrons). At the Au/Ir(001) target, secondary electrons are generated during LEED (shown in green). These SE will not leave the crystal towards the detection unit as they are attracted back to the crystal-holder plate. The trajectory of the LEED electrons moving towards the detection cone experience the negative potential of the deflection plate and their trajectory bends into the detection cone. Secondary electrons can be emitted at the entrance of the detection cones or their grids due to impinging LEED electrons. These SE, which are shown in blue, only reach the MCPs when they are created beyond the second grid. Elsewise, they are attracted to the entrance of the detection cone.

Figure 5.12 shows the trajectories of the diffracted SE into the detection cones. The trajectories of the spin-polarized secondary electrons that leave the exit optics and fly perpendicularly onto the Au/Ir(001) target are shown as brown lines. During LEED, secondary electrons are created at the Au/Ir(001) target, shown in green in Figure 5.12, that are attracted back to the crystal-holder plate. They do not leave the crystal towards the detection unit and thus will not contribute to the noise level. After the low-energy electron diffraction at the Au/Ir(001) target, the electrons of the (1,1)-LEED beams exit at an angle of 57° (between crystal plane and electron trajectory) towards the detection cones. Their trajectories are shown as red lines. There, they experience the electric field of the deflection electrode and their trajectories are bent into the entrance of the detection cone before their beam is widened by the defocusing optics. The bright

blue lines in Figure 5.12 show the trajectories of secondary electrons that have been created at the grids. Only the SE that have been created beyond the second grid reach the MCP, those emitted before are attracted toward the entrance of the detection cone.

The electron trajectory seen in Figure 5.12 describes the optimum situation. Within the angular acceptance of $\pm 4^\circ$ all diffracted electrons enter the entrance of the detection cone. Thus, even small deviations of the trajectories due to production/alignment tolerances or the energy width of the spin-polarized SE will not impede the LEED electrons from entering the detection cone.

5.5 Summary and Outlook

The idea and design for a new spin detector whose dimensions are customized for the out-of-plane SEMPA and that is based on LEED at a pseudomorphic Au monolayer on Ir(001) has been presented in this chapter. A suitable working point for the application in a spin-polarized LEED detector has been found for a scattering potential of 142 eV promising a four times higher FOM compared to the W(001)-based detector design. The cleaning procedure, as well as the procedure for the creation of the pseudomorphic monolayer, have been tested in the preparation chamber of the in-plane SEMPA setup which additionally allowed to monitor the crystal surface via LEED between the process steps. For the cleaned Ir(001) crystal the (5x1) pattern due to a surface reconstruction has been observed. After evaporation of Au and heating to 860°C the (1x1) pattern of unreconstructed Ir(001) was observed which is reported in literature as a sign for the existence of the pseudomorphic monolayer.

The design of the spin detector that has been constructed in a CAD software consists of three main components: the crystal-holder tube, which allows to move the Ir(001) from the measurement position to the preparation position, the detection unit with its deflection plates to bend the trajectories of the scattered spin-polarized electrons into the MCP-equipped detection cones, and the Au evaporator, which allows to evaporate Au onto the Ir(001) surface from a crucible. The electric potentials within the spin detector as well as the trajectories of the spin-polarized electrons have been simulated in SIMION. The simulations revealed that within an angular acceptance of $\pm 4^\circ$ all diffracted electrons enter the entrance of the detection cone. Furthermore, SE created at the Au/Ir(001) target are attracted back to the sample holder plate instead of entering the detection cones. Also, those SE created before the second grid of the detection cone, namely at its entrance and at the first grid, do not reach the MCPs as they

5.5. Summary and Outlook

are accelerated to the entrance of the cone. Thus, they do not cause any noise in the measurement. Only the SE created beyond the second grid are detected. Recently, the last pieces for the detector have been manufactured. The next project steps, including the assembly, putting the new detector into operation, as well as comparing the performance of the new detector with the W(001)-based one have been handed over to Ralph Buß, and will be part of his PhD thesis [143].

Magnetic domains and domain walls in an epitaxially grown Co/Pt(111) film

In 1989, Bogdanov and Yablonskii [144] first introduced the theoretical concept of a thermodynamically stable system of magnetic "vortices", which were later named magnetic *skyrmions*. Since then, these quasiparticles have been not only predicted theoretically in several systems [145–147], but have also been observed experimentally in magnetic bulk systems [148, 149] as well as in magnetic (ultra)thin films [14, 150, 151]. The stability of skyrmions, which results from a topological protection due to their spin alignment with respect to the spins of the surrounding film, makes these magnetic structures interesting for the next generation of data storage devices.

In thin film systems, where the magnetization is perpendicular to the film plane, skyrmions are stabilized due to the (interfacial) Dzyaloshinskii-Moriya interaction (DMI, see Section 3.4) which emerges at interfaces between a ferromagnetic and a non-magnetic layer (broken inversion symmetry) in systems with large SOC. The energy associated to the DMI is not always large enough to stabilize skyrmions. Nevertheless, the DMI affects the magnetic structure, namely the domain walls, and its strength can thus be quantified. The DMI adds to the domain-wall energy in such a way that Néel-like walls of a given sense of rotation become energetically favorable over Bloch walls, which leads to the existence of either tilted Bloch-like or pure Néel-like walls [112, 152]. By earning a greater understanding of the DMI at interfaces, researchers empower themselves to design sample systems with customized magnetic properties, e.g. for the stabilization of skyrmions. A crucial step towards this goal lies within the task of bringing theoretical calculations in accordance with experimental findings. With regard to the determination of the DMI strength, experimental results are often not comparable with theoretical predictions, mainly due to non-ideal interfaces re-

sulting from the preparation process, as will be discussed in greater detail later on. Experimental investigations of systems with interfaces that are as ideal as possible are thus of great interest as they present a link between theory and experimental studies of systems with non-ideal interfaces, adding greatly to the fundamental understanding of the DMI.

In this chapter, the magnetic domains and domain walls in an epitaxially grown Co/Pt(111) wedge are studied. At first, the current state of knowledge concerning the DMI in Co/Pt(111) is summarized and open questions are pointed out. Afterwards, the epitaxial preparation of Co wedges on a Pt(111) single crystal is presented. The investigation of the system with the in-plane SEMPA instrument is introduced before the Co-thickness dependent behavior is discussed and an analysis of the system at 7 ML Co is given. Furthermore, the domain-size model as proposed by Kaplan and Gehring is introduced and used to discuss the effect of the DMI in the Co/Pt(111) system as well as to estimate a lower bound of the DMI strength. Finally, the chapter closes with a short summary and outlook.

The magnetization images presented in this chapter were measured jointly with Dr. Edna C. Corredor, while the analysis of the 7ML Co on Pt(111) system was performed together with Fabian Kloodt-Twesten, who will present a quantitative analysis of the taken dataset in his future PhD thesis [153]. Parts of the results presented in this chapter have been published as a Rapid Communication in Physical Review B [115]¹.

6.1 The need of determining the DMI of the single Co/Pt interface

Co-based systems are of particular interest for studies on the DMI, as skyrmions have been observed in these Co systems up to RT [154–157]. From *ab initio* calculations a strong anticlockwise (ACW) DMI is predicted for Co/Pt(111) [147, 158, 159], which corresponds to a positive DMI strength. Absolute values of the total DMI strength d_{tot} , which gives the DMI strength in meV per bond between Co atoms at the interface, were determined within these studies and lie in the same order of magnitude²: Freimuth *et al.* find $d_{\text{tot}} = 2.7 \frac{\text{meV}}{\text{Co}}$ [160], Yang

¹E.C. Corredor, S. Kuhrau, F. Kloodt-Twesten, R. Frömter and H.P. Oepen. *SEMPA investigation of the Dzyaloshinskii-Moriya interaction in the single, ideally grown Co/Pt(111) interface*. Phys. Rev. B 96, 060410(R) (2017).

²As the published theoretical values are derived using different units and definitions, the results have been converted by F. Kloodt-Twesten into the here presented parameter d_{tot} giving the total DMI strength in meV per bond between Co atoms at the interface.

6.1. The need of determining the DMI of the single Co/Pt interface

et al. $d_{\text{tot}} = 3.1 \frac{\text{meV}}{\text{Co}}$ [158, 161], Dupe *et al.* $d_{\text{tot}} = 3.6 \frac{\text{meV}}{\text{Co}}$ [147] and Vida *et al.* derive a value of $d_{\text{tot}} = 2.9 \frac{\text{meV}}{\text{Co}}$ [159].

Experimentally, the effect of the total DMI on domains and their walls has been thoroughly studied for sputtered polycrystalline Co/Pt films as well as for sputtered multilayers of these two constituents [121, 150, 162–166]. Trilayer systems provide the possibility to enhance the effective DMI by adding such constituents on top of the magnetic layer that will create a DMI contribution of the same sign as in the interface below, leading to an increase of the total DMI in the stack. Unfortunately, this method of maximizing the effective DMI in a system is accompanied by a disadvantage in regard to gaining a fundamental understanding of the interfacial DMI. When trilayers (e.g. Pt/Co/Ir) or multilayers (e.g. [Co/Pt]_n) are studied, it is not possible to separate the DMI contributions of the interfaces on top and below the magnetic layer experimentally. Only the effective DMI of the multilayer stack is measured.

Another issue arises in samples prepared via sputter deposition. The interfaces between the layers are non-ideal and show disorder as they suffer from intermixing or roughening due to the sputter deposition. Zimmermann *et al.* [167] as well as Yang *et al.* [158] found a strong impact of such disorder to the DMI strength in theoretical calculations. While the first study reports on a decrease of the DMI strength by 20 % (in contrast to the ideal, undisturbed interface) for intermixing in the range of 20-80 %³, the second study reports that the DMI strength decreases by 50 % at 25 % interfacial intermixing. Besides this intermixing related issue, a second aspect of the sample preparation has to be kept in mind. For most analysis techniques it is necessary to add a capping layer on top of the sample stack to avoid oxidation of the magnetic layer. The capping again might affect the total DMI as a cap introduces another interface, which in turn necessitates a disentangling of the DMI contributions.

As opposed to this, no additional DMI contribution from a vacuum/Co interface is expected to arise for an uncapped Co/Pt sample [168], which is prepared as well as studied under UHV conditions. Very recently, an experimental study concerning the DMI of the single interface in the epitaxial Co/Pt(111) system was conducted [169] which confirmed the ACW sense of rotation of the domain walls, but the DMI strength could not be derived experimentally. The in-plane SEMPA instrument (see Section 4.1) with its attached preparation chamber provides the possibility to perform such an investigation on a Co/Pt(111) system, as Co can be evaporated epitaxially onto a cleaned Pt(111) crystal. An interface

³Here, 100 % intermixing means the top layer of the lower material has swapped with the first layer of the upper material.

comparable to the systems studied in *ab initio* calculations arises, allowing for a direct comparison to theoretical results of the ideal interface.

6.2 Preparation of the Co wedge on Pt(111)

The preparation of the Co/Pt(111) sample was performed at a base pressure of 10^{-10} mbar in a preparation chamber that is directly attached to the in-plane SEMPA instrument. First, the Pt(111) single crystal was cleaned. Cycles of Ar^+ sputtering at 500 eV (1 μA) and annealing in an oxygen atmosphere of $2 \cdot 10^{-8}$ mbar at 900 K for 50 min were used to remove carbon impurities from the topmost nanometers of the crystal. The temperature during the annealing was checked with a disappearing-filament pyrometer.

After the carbon-depletion, the final annealing step comprises a flash of the Pt(111) crystal without oxygen to about 1250 K in order to desorb the remaining oxide layer from the sample surface. The success of the cleaning process was checked by evaluating the crystal surface via LEED as will be discussed later on in detail. The Co was evaporated onto the cleaned Pt(111) crystal at RT as a wedge, ranging from 0 to 10 ML (0 to 2.0 nm) thickness, as well as in a stepped way, similar to a staircase. The results of these two possible evaporation types are shown schematically in Figure 6.1a). The wedge was created by a shutter moving at constant velocity in front of the crystal. Implementing the velocity profile of the shutter was realized by using a programmed piezoelectric stepper actuator (Attocube) to which the shutter is fixed. As indicated in the sketch of the stepped Co wedge, the step widths and heights can be prepared as needed, and also subwedges between the steps can be created.

The (partially) stepped samples with plateaus of the Co thickness allow a position and thickness cross check in the SE image. Figure 6.1b) shows an exemplary SE image of a step in the Co/Pt(111) sample. The clean Pt(111) side is brighter than the thin Co layer with an effective thickness of 1 ML. Such a change in the contrast was also observed at steps between thinner and thicker Co areas, though it becomes less pronounced for higher Co thicknesses (e.g. between 5 and 6 ML). The obvious explanatory approach that this contrast might result from the different work functions needs to be considered with caution. Literature reports for Pt(111) a work function of $\Phi_{\text{Pt}(111)} = 5.9 \text{ eV}$ [170] while a values of $\Phi_{\text{Co,fcc}(111)} = 5.0 \text{ eV}$ [170] and $\Phi_{\text{Co,hcp}(0001)} = 4.9 \text{ eV}$ [171, 172] are reported for Co. The lower value for Co would result in a higher SE emission on the right-hand side, which contradicts the observed contrast.

6.2. Preparation of the Co wedge on Pt(111)

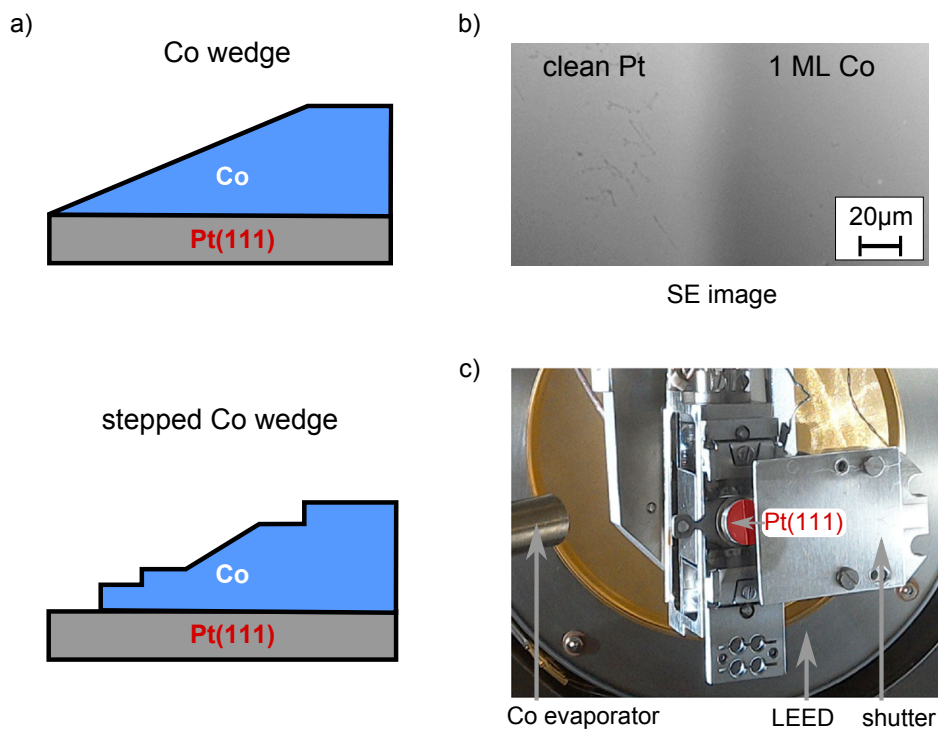


Figure 6.1: a) Two exemplary sample designs. To investigate the Co-thickness-dependent magnetic behavior, straight wedges as well as stepped ones have been prepared. b) Steps in the Co coverage result in a brightness contrast in the SE images. Here, the step from clean Pt(111) to 1 ML of Co is shown. The implementation of steps in the sample design allows thus for a precise thickness cross check and localization along within the wedge. c) Inside view of the preparation chamber. The Pt(111) crystal is highlighted in red. The piezoelectrically driven shutter is seen to its right. Co was evaporated from the evaporator visible on the left. The LEED in the back of the image was used to check the cleanliness of the surface of the Pt crystal as well as to cross check the thickness of the evaporated Co.

The growth of thin Co films on Pt(111) will be discussed in detail later on (page 81)—in brief, a lattice mismatch between Co and Pt(111) of 9.4% exists [173]. The Co at the interface thus experiences a tensile strain, which can be suspected to affect the band structure and the work function. Thus, the literature value of the work function for bulk Co is not necessarily applicable for the here investigated ultrathin films. On second thought, the observed contrast might also be attributed to a Z -contrast ($Z_{\text{Pt}} = 78$, $Z_{\text{Co}} = 27$) of the backscattered electrons which are detected beside the SE which in addition can lead to the emission of

type II SE⁴. Though this approach seems on a first glance to be in accordance with the darker Co side, a Monte Carlo simulation with the Casino software [174] reveals that the BSE yield between pure Pt and a 0.2 nm thick Co on Pt system varies by less than 3%. It can be suspected that such a small difference might not result in the observed contrast. The origin of the here observed change in contrast at the positions of the Co steps can thus not be clarified for good in this thesis.

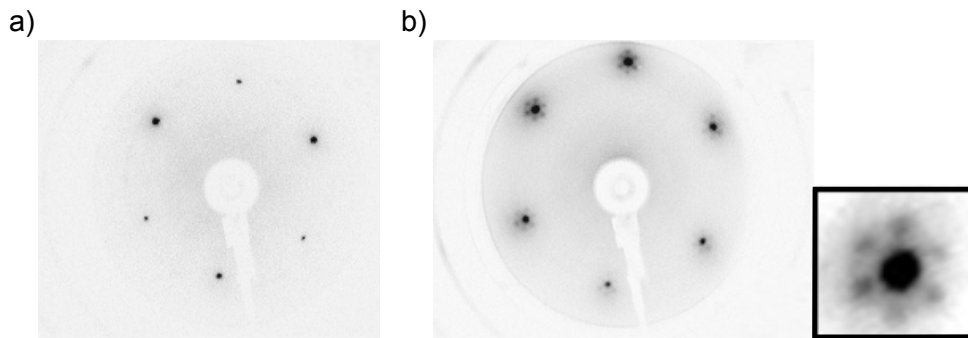


Figure 6.2: LEED images taken at 80 eV of a) the clean Pt(111) crystal and b) a 1.0 nm thick Co film (4 ML) on Pt(111). The six-fold fine structure around the main LEED spots is enlarged in the lower right. Graphic adapted from [115].

The Pt(111) crystal was fixed on top of a molybdenum sample holder (ScientaOmicron, Omicron sample plate) with tantalum strips that were spot welded onto the plate. Figure 6.1c) shows a picture of the preparation chamber with the crystal highlighted in red. On its right the piezoelectrically driven shutter can be seen. After aligning the sample accordingly to the evaporator, Co was deposited at normal incidence from a high-purity rod using an electron beam evaporator which is visible to the left in Figure 6.1c). The deposition rate of 0.07 nm/min was calibrated *ex situ* via ellipsometry measurements. The rate was kept stable during the evaporation process by monitoring and controlling the Co flux and the emission current. The LEED instrument, visible behind the sample holder, was used to check the quality of the surface of the cleaned Pt(111) crystal as mentioned above. Figure 6.2a) shows the observed LEED pattern of the clean Pt(111) surface with sharp p(1x1) spots and low background. Further LEED patterns taken at several Co thicknesses are in agreement with previous observations of samples prepared under similar conditions [175]. Exemplarily,

⁴Secondary electrons of type II are those SE that are created when back scattered electrons leave the sample. In contrast, SE created due to the interaction between the PE beam and the sample are labeled with type I.

6.3. Detecting the perpendicular magnetization in an in-plane sensitive SEMPA

Figure 6.2b) shows the observed LEED image after the evaporation of 4 ML of Co. Satellites around the Pt(111) $p(1 \times 1)$ spots arise in a six-fold symmetry at this Co coverage. The latter fine structure can be seen enlarged in the lower right and has been reported in literature for Co thicknesses between 1.2 and 4.5 ML on Pt(111) [173, 176]. The origin of this fine structure is associated with the lattice mismatch between Co and Pt of 9.4%⁵ which prohibits a perfect pseudomorphic growth of the first Co layer on Pt(111). Instead, a dislocation network is formed to release the strain arising from the lattice mismatch, as observed in STM measurements [173]. Due to the partial dislocations, two types of regions exist in which the stacking corresponds to either fcc or hcp Co, though the area covered with fcc-stacked Co prevails. The growth mechanism of the following Co layers has been described by Grütter *et al.* [176] as "quasi-layer-by-layer" growth, as the growth of a succeeding layer starts shortly before the completion of the previous one⁶. Nevertheless, below 0.7 nm (3.5 ML) a flat two-dimensional growth of Co is reported [173, 176]. Growing on top of the first Co layer, the second Co layer develops a moiré structure, which is observed up to 4.5 ML [173, 176], due to varying in-plane lattice spacing of the Co overlayer. The six-fold fine structure observed in LEED is attributed to the observed periodicity (about 13 Co atoms [173]) of the above mentioned dislocation network, which results in additional LEED spots. Contrary to this, Perini [177] noted just recently that the observed structure might not be a moiré pattern but a misfit structure resulting from a gradual change of the lattice constants from Pt to Co, which might be associated with an intermixing between the first Co layer and the Pt, even for preparations at RT. In the study presented here, defined LEED spots have been observed up to a Co thickness of 7 ML (1.4 nm). For Co thicknesses above 7 ML the LEED pattern becomes blurry as the Co starts to grow in triangular-shaped islands with predominantly fcc-twinning stacking [173].

6.3 Detecting the perpendicular magnetization in an in-plane sensitive SEMPA

The investigation of the magnetic structure of Co/Pt(111) presented in the following was performed at the in-plane SEMPA instrument which allows to detect the two in-plane magnetization components (see Chapter 4.1). As will be shown

⁵Nearest neighbor distance of 2.51 Å for Co and 2.77 Å for Pt.

⁶The formation of islands of the third Co monolayer have actually been observed to start before the first layer has been closed completely.

in the following, a pure out-of-plane magnetization is observed for Co thicknesses below 8 ML. The capability of the setup to detect the two in-plane components of the magnetization is advantageous to image the magnetization of the domain walls, as these naturally have to lie in plane. Then again, it was found beneficial during the experiments to have a hint on the location and orientation of the domains for a detailed analysis. Therefore, the sample was slightly tilted out of its usual position, in which the surface of the sample is aligned parallel to the surface of the W(001) crystal in the detector. Thus, a slight projection of the perpendicular component of the magnetization becomes visible in the vertical (y direction) in-plane channel.

6.4 Domain size in dependence of Co thickness

The magnetization images taken along the Co wedge reveals an onset of ferromagnetism at about 1.5 ML Co coverage. The size of the observed perpendicular domains decreases monotonously with increasing Co thickness until the SRT sets in at a Co thickness of about 8 ML.

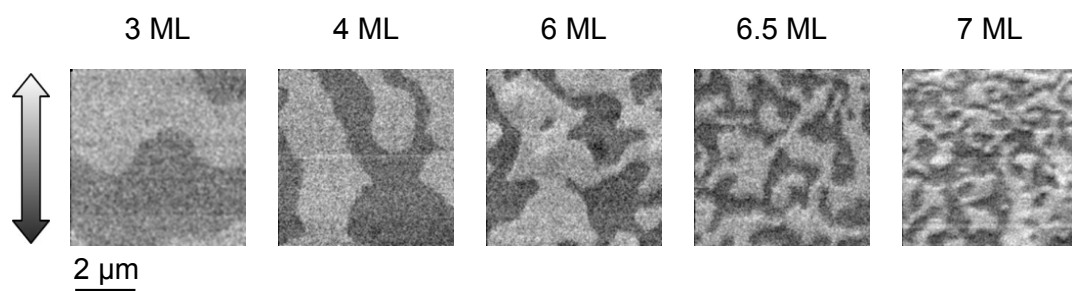


Figure 6.3: Magnetization images taken in the thickness range from 3 to 7 ML Co at the same magnification visualize the decrease in domain size with increasing Co thickness. Within this thickness range a perpendicular magnetization is observed. Due to the sample tilt of about 10° , the perpendicular component of the magnetization is admixed into the vertical magnetization channel. Thus, the gray scale arrow on the left does not only contain the usual information of the vertical magnetization, but also information on the out-of-plane component (bright: magnetization towards \odot or \uparrow , dark: magnetization towards \otimes or \downarrow). While for film thicknesses below 6 ML only the domain contrast is visible, additional contrast due to the domain walls (in-plane magnetization) is visible at higher Co coverages.

Figure 6.3 shows magnetization images for Co coverages in the range from 3 to 7 ML, taken with the same magnification to emphasize the reduction of the

6.4. Domain size in dependence of Co thickness

average domain size. The observed domain structure in the as-grown state corresponds to a disordered maze pattern. The change of the average domain size originates from the changing influence of the anisotropy contributions. With increasing Co thickness the influence of the surface anisotropy reduces with the magnetic film thickness t in a $1/t$ -behavior, see Equation 3.11 (page 22). Therefore, the shape and volume anisotropy gain influence, which eventually will lead to an SRT. In total, the effective anisotropy K_{eff} decreases, which leads to a reduction of the domain-wall energy. The implementation of a domain wall to reduce the magnetostatic energy is thus associated with a smaller energy cost. The magnetization images contain information concerning the perpendicular (sample tilt, see Section 6.3) as well as the vertical component of the magnetization. While for film thicknesses below 6 ML only the domain contrast is visible, additional contrast due to the domain walls (in-plane magnetization) is visible for higher Co coverages. A closer look at the magnetization images above 6 ML Co reveals that dark domains are outlined by an additional, inhomogeneous contrast that appears bright below and dark above these domains. For Co thicknesses below 6 ML, the domain walls are too thin to be resolved in measurements with the above-chosen imaging parameters.

For a quantitative description of the reduction of the domain size with Co thickness, the average domain sizes can be determined by the stereological method as proposed by Bodenberger and Hubert [178]. In this method, randomly oriented line profiles are extracted from the domain image. Bodenberger and Hubert introduce a formula to derive the average magnetic domain width by calculating the ratio between the total length of the test lines and the number of intersections with domain walls, and weighting this ratio by a factor of $2/\pi$. Based on this approach, a more detailed access to the domain size is obtained by analyzing the line lengths of the profile segments between domain walls, and generating a histogram of the domain size distribution. The magnetization images used for this analysis need to show a sufficiently large area to ensure appropriate statistics of the resulting domain size distribution. The data set taken in this study was aimed at resolving the domain walls in the system; thus, most images contain only a comparably small number of domains.

On the basis of a few images that meet the above mentioned criteria histograms of the domain size distributions have been generated, exemplarily shown in Figure 6.4a). According to Bodenberger and Hubert [178], the domain size of this exemplary domain pattern equals $d_{\text{Bodenberger}} = 1.13 \mu\text{m}$.

The asymmetric behavior of the domain size distributions, as for example shown in Figure 6.4a) for the domain pattern observed at 6 ML Co/Pt(111), can be

Chapter 6. Magnetic domains and domain walls in an epitaxially grown Co/Pt(111) film

described with a gamma distribution, as was introduced by Bagschik *et al.* [179]. The probability density function (PDF) of the gamma distribution is given by

$$g(x) = \frac{x^{k-1} \exp(-x/\vartheta)}{\vartheta^k \Gamma(k)}, x > 0, \quad (6.1)$$

with the shape parameter $k > 0$, the scale parameter $\vartheta > 0$ and the gamma function $\Gamma(k) = \int_0^\infty t^{k-1} \exp(-t) dt$ with $t = \log(k)$. The symmetry and the width of the distribution function are determined by the shape parameter k , the scale parameter ϑ on the other hand stretches the profile of the PDF. The parameters characterizing the fit curve, which is shown in blue in Figure 6.4a), take on the values of $k = 2.4$ and $\vartheta = 0.3$. The shape parameter k provides a quantity to classify the domain pattern. It takes on a rather constant but low value of 2.2 ± 0.2 within the thickness range below 7 ML, which is in agreement with the observed highly-disordered maze domain patterns. In contrast, a value of $k = 4$ is found for just slightly disordered maze patterns [179].

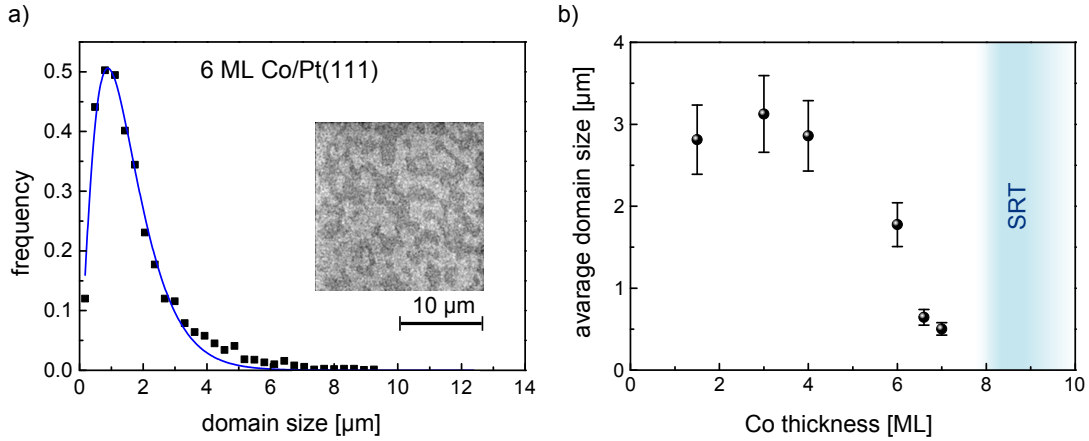


Figure 6.4: a) Exemplary histogram of the domain-size distribution (black squares) for 6 ML Co on Pt(111). The blue graph gives the PDF of the gamma function with $k = 2.4$ and $\vartheta = 0.3$. The magnetization image used to obtain the histogram is shown as inset. b) Average domain sizes $d_{\text{Bodenberger}}$ according to the stereological approach of Bodenberger and Hubert between 1.5 ML Co (onset of ferromagnetism) and 7 ML.

Via the above described stereologic method of Bodenberger and Hubert, the average domain sizes have been derived for the Co thickness range between 1.5 ML and 7 ML, shown in Figure 6.4b). The average domain sizes obtained using this method are in agreement with the qualitatively observed behavior of the domain size as shown in Figure 6.3. The domain size in the as-grown measured Co/Pt(111) system is nearly constant in the range from 1.5 to 4 ML of Co showing a value of about 2.8 μm . Such a behavior is common for as-grown systems, as

6.5. Néel-like walls with fixed anticlockwise sense of rotation

at thin film thicknesses the domains are influenced by the layer-by-layer growth of the magnetic film on the substrate which is not covered completely at this Co thickness, as has been observed by STM measurements [176, 177]. In colloquial language, these domains are sometimes referred to as "growth domains" whose size and shape is "frozen" into the film upon increase of the magnetic material. Upon further increase of Co thickness beyond 4 ML the domain size decreases due to the changing anisotropy contributions, as discussed before in Section 6.3.

6.5 Néel-like walls with fixed anticlockwise sense of rotation

As pointed out with respect to Figure 6.3, which shows magnetization images at various Co thicknesses below the SRT, the domain walls are resolveable for film thicknesses above 6 ML. In the following, a closer inspection of the domain walls at a Co thickness of 7 ML (1.4 nm) is presented. This thickness is chosen as for thinner Co films the domain walls become too small to be imaged satisfyingly, while at slightly higher Co thicknesses the SRT sets in. For determining the domain-wall type, a magnetization image with sufficient lateral resolution of the 7 ML Co on Pt(111) sample is analyzed. The raw data of the magnetization components along the horizontal and vertical direction are shown in Figure 6.5a) and b), respectively. The gray-scale arrows in the upper right corner indicate the direction of the magnetization of bright or dark areas (e.g. for the horizontal component, the magnetization of bright areas points to the left, dark areas to the right). For this image, the sample has been slightly tilted by 3° around the horizontal axis. While the domains visible in the horizontal magnetization component (Figure 6.5a)) show the same gray level, domains which point out of the substrate have a slightly brighter contrast in the vertical component (Figure 6.5b)) due to the tilt. The most noticeable contrast visible in both images is given by the domain walls, where the magnetization lies in the film plane. The information of all three magnetization directions, which have been extracted from the shown raw data, is condensed in the full three-dimensional map of the magnetization given in Figure 6.5c). In this compilation, the black and white contrast indicates domains pointing up and down, respectively. The in-plane orientation of the domain-wall magnetization is color coded with respect to the color wheel in the lower left. Furthermore, the magnetization direction is also given for a small area by arrows. This encircled area is depicted enlarged below,

showing that the magnetization of all domain walls points outward of the down domains (\otimes) and inward of the up domains (\odot), revealing the Néel character of the domain walls and the fixed anticlockwise rotational sense of the Néel-like walls in the imaged area. The anticlockwise sense of rotation is equivalent with a positive sign of the DMI strength and is in agreement with theoretical *ab initio* calculations.

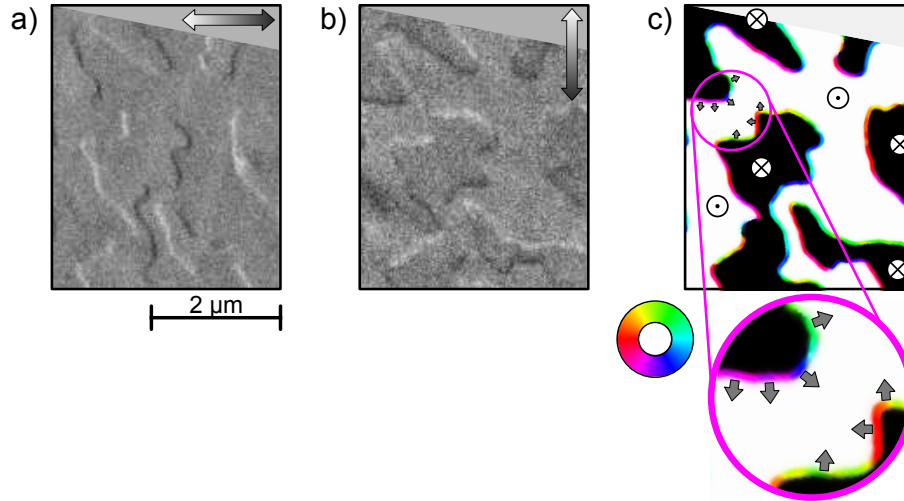


Figure 6.5: Analysis of the magnetic domain structure at 7 ML (1.4 nm) Co. Panel a) and b) show the magnetization components along the horizontal and vertical direction, respectively. A weak out-of-plane contrast is observed in the vertical component due to a slight tilt, leading to a superimposition of the domains with perpendicular magnetization into the vertical component. In c) a full three dimensional map of the magnetization vector has been put together from the raw data. Black and white indicate the down and up pointing out-of-plane domains. The in-plane domain walls are color coded with respect to the color wheel on the lower left. The enlarged area with additionally drawn arrows indicating the direction of the magnetization of the domain walls visualizes the fixed sense of rotation of the observed Néel-like walls. Graphic adapted from [115].

6.6 Discussion of the DMI strength based on a domain-size model

Various complex models for the description of the domain size of magnetic (multilayer) films in dependence of the magnetic film thickness have been published over the last decades. Such models describe the thickness-driven evolution of the average domain size for a system in its equilibrium state, meaning when it

6.6. Discussion of the DMI strength based on a domain-size model

has reached its energetic minimum. In contrast, the here-studied Co/Pt(111) system is investigated in its as-grown state, which is a significant difference that has to be taken into account in the later discussion. For a discussion of the trends observed in Figure 6.4b) the analytical model as proposed by Kaplan and Gehring [180], which gives an approximation for the domain size in a magnetic single layer by evaluating the domain-wall energy, will be used in the following. This model is straightforward and is thus comparatively intuitive to understand. Two more well-known domain-size models that are slightly more complex, but are as well based on the domain-wall energy, are the model by Draaisma and de Jonge [181] which has been derived to model the stripe domain structure of multilayer systems with PMA, or the model by Lemesh *et al.* [182] which additionally includes effects of the volume and surface charges of the domain walls. Both models require solving numeric equations, while in the here used model of Kaplan and Gehring all contributions will be quantified analytically. The domain size d_{KG} according to the model of Kaplan and Gehring is given by:

$$d_{\text{KG}} = Bt \exp\left(\frac{\pi}{2} \frac{\gamma_w}{E_{ms}t}\right) \quad (6.2)$$

B is a prefactor that reflects the geometry of the domains and takes on a value of 0.955 for stripe domains or 2.620 for a checkerboard pattern, respectively [180, 183]. In our case, a prefactor of $B = 1.375$ has been used to account for the observed maze pattern⁷. Furthermore, t gives the thickness of the magnetic film, γ_w the domain-wall energy density and $E_{ms} = \mu_0 M_S^2/2$ is the magnetostatic energy ($M_S(\text{Co}) = 1.44 \text{ MA/m}$ at RT [81]). The domain-wall energy density per unit area γ_w is given by

$$\gamma_w = 4\sqrt{A_{\text{ex}}K_{\text{eff}}} + t \frac{\ln(2)}{\pi} \mu_0 M_s^2 \cos^2 \Phi + \pi D_{\text{DMI}} \cos \Phi \quad (6.3)$$

and sums up the contributions from the anisotropy and exchange stiffness (first term), the stray-field energy of the volume charges of the domain wall as derived by Tarasenko *et al.* [185] (second term) and the energy contribution due to the DMI (third term). The angle Φ describes the angle between the in-plane magnetization direction present in the center of the domain wall and the normal of the domain wall. This angle takes on a value of 0 or π for pure Néel walls (clockwise or anticlockwise sense of rotation, respectively) and $\pm\pi/2$ for pure

⁷This exact value was chosen as an investigation of a Co/Pt multilayer found that the domain size in the maze pattern is 1.44 times larger than the one in the stripe pattern [184]. Testing different values of B (between 0.995 and 2.620) for the domain-size evolution shown in Figure 6.8 revealed that the influence of B is comparatively small and negligible, especially in contrast to the later shown influence of slightly different DMI values.

Chapter 6. Magnetic domains and domain walls in an epitaxially grown Co/Pt(111) film

Bloch walls. A quantitative analysis of the domain walls that are shown in Figure 6.5 is published in references [115, 153] and reveals that for the here-observed anticlockwise Néel walls $\Phi = \pi$ applies, meaning they are of pure Néel character. In the analysis of the latter references, furthermore, an anisotropy constant of $K_{\text{eff}} = (0.38 \pm 0.04) \text{ MJ/m}^3$ for 7 ML Co/Pt(111) has been derived, which will be used in the following to model the thickness-dependent anisotropy in the system.

As introduced in Equation 3.11, the effective anisotropy is determined by three terms—the volume anisotropy K_V , the shape anisotropy $K_d = -\mu_0 M_S^2/2$ and the surface anisotropy K_S :

$$K_{\text{eff}} = K_V + K_d + \frac{2K_S}{t}$$

As the interfaces on top and below the Co film are not identical (Co/Pt(111) versus UHV/Co), the corresponding interface anisotropies are expected to differ, and the obtained K_S value is an average surface anisotropy of both interfaces: $K_S = (K_{S,\text{Co/Pt}} + K_{S,\text{UHV/Co}})/2$.

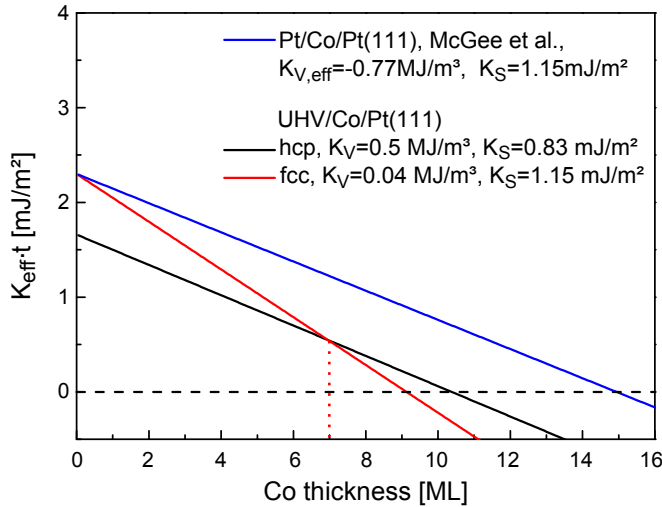


Figure 6.6: Plot of $K_{\text{eff}} \cdot t$ against the Co thickness t for the two derived cases for a pure fcc and a pure hcp lattice for the UHV/Co/Pt(111) system, shown as red and black line, respectively, and of an epitaxially grown Pt/Co/Pt(111) system as studied by McGee *et al.* [186], shown as blue line.

By using the literature value for the volume anisotropy of a specific lattice type, a K_S value can be derived that fulfills Equation 3.11 at 7 ML Co. As the growth of Co on Pt(111) is reported to start as fcc and changes to a mixture of fcc and hcp (dislocation network to release strain, see page 81) with increasing Co thickness, the limiting cases of a pure fcc and a pure hcp lattice are studied in the following. Therefore, the values found in literature for the volume anisotropy

6.6. Discussion of the DMI strength based on a domain-size model

of Co for fcc $K_{V,\text{fcc}} = 0.04 \text{ MJ/m}^3$ [187]⁸ and hcp $K_{V,\text{hcp}} = 0.5 \text{ MJ/m}^3$ [188] are used to find the interface anisotropies, which result in $K_{S,\text{fcc}} = 1.15 \text{ mJ/m}^2$ and $K_{S,\text{hcp}} = 0.83 \text{ mJ/m}^2$. The anisotropy parameter have been used to plot $K_{\text{eff}} \cdot t$ against the Co thickness t in Figure 6.6 for both lattice types; the red line shows the fcc case and the black line the hcp case. As the known value of K_{eff} at 7 ML was used to derive both interface anisotropies, the lines intersect at 7 ML (highlighted by red dotted line). Additionally to the two derived dependencies for the UHV/Co/Pt(111) system, the $K_{\text{eff}} \cdot t$ against t plot for an epitaxially grown⁹ Pt/Co/Pt(111), investigated by McGee *et al.* [186], is added to the graph. Adding the shape anisotropy for Co to the effective volume anisotropy of $K_{\text{eff}} = -0.77 \text{ MJ/m}^3$ that was experimentally derived by McGee *et al.* gives the value of the corresponding volume anisotropy which roughly coincides with the one of the hcp lattice, thus both lines have a similar slope. On the other hand the interface anisotropy that was experimentally determined by McGee *et al.* equals the one derived for the pure fcc lattice—thus, both lines intersect at a Co thickness of zero ML¹⁰. At the Co thickness t_{SRT} at which K_{eff} becomes negative, the SRT takes place and the out-of-plane direction of the magnetization changes into the film plane. According to the derived anisotropies, this thickness equals 9.1 ML for the fcc and 10.3 ML for the hcp case. In the simple model used here, higher orders of the anisotropy, which would influence the SRT, are neglected. Exemplarily, an investigation on sputtered Co/Pt multilayers revealed a second order anisotropy value of $K_2 = +116 \text{ kJ/m}^3$ [189] which leads to a canting of the magnetization into the film above t_{SRT} . In contrast, negative K_2 values indicate that the thickness-driven SRT takes place via a coexistence phase, which takes place slightly below t_{SRT} [190].

Besides the anisotropy, also the value of the exchange stiffness A_{ex} is thickness dependent in ultrathin films. When evaluating the domain sizes below 10 ML of Co, the exchange stiffness can be estimated from the bulk exchange stiffness $A_{\text{ex,bulk}}$ by assuming that it scales linearly with the average coordination number of the Co atoms. Several approaches to illustrate the derivation of this formula

⁸The volume anisotropy for fcc Co is, especially in comparison to the hcp value, negligible small. To use a non-zero value for the following calculation, the value for the uniaxial anisotropy for the case of a polycrystalline textured Co film is used which was derived from the value of the cubic system reported in [187].

⁹Grown via molecular beam epitaxy.

¹⁰ Concerning this perfect agreement of the K_S values one has to keep in mind that the Co film in the study of McGee *et al.* is sandwiched between Pt layers but the here investigated Co film has no cap layer but an UHV interface at its top, so this agreement is interpreted as a coincidence.

Chapter 6. Magnetic domains and domain walls in an epitaxially grown Co/Pt(111) film

exist, one is exemplarily given in the following. Both lattices, fcc and hcp, have a coordination number of $C = 12$ in the bulk; in a single monolayer the coordination number of Co reduces to 6. Thus, for a double layer, an average coordination number of 9 results. For a film of n_{Co} monolayers of Co, the layers can be separated in two cases by their coordination number. The top and bottom layer have a coordination number of 9, while all other ($n_{\text{Co}} - 2$) layers have the full coordination number of 12. The exchange stiffness given in dependence of the number of Co monolayers n_{Co} is hence given via:

$$A_{\text{ex}}(n_{\text{Co}}) = \frac{A_{\text{ex,bulk}}}{12} \cdot \frac{9 \cdot 2 + 12(n_{\text{Co}} - 2)}{n_{\text{Co}}} = A_{\text{ex,bulk}} \cdot \left(1 - \frac{1}{2n_{\text{Co}}}\right) \quad (6.4)$$

According to this formula, a value of 90% of the bulk value $A_{\text{ex,bulk}}$ is already reached at 5 ML. The formula will also be used as approximation of $A_{\text{ex}}(n_{\text{Co}})$ for non-integer values of n_{Co} , and furthermore is set to zero for film thicknesses below 0.5 ML, as at these thicknesses the used linear assumption results in negative values of $A_{\text{ex,bulk}}$, which are an unphysical result.

To evaluate the influence of the three contributions to the domain-wall energy density γ_w (see Equation 6.3), all three contributions are plotted separately in Figure 6.7a). The contribution of the exchange stiffness and the anisotropy, $4\sqrt{A_{\text{ex}}K_{\text{eff}}}$, is shown in black. The solid black line represents the resulting energy density for the fcc lattice, using $A_{\text{ex, fcc}} = 23.3 \text{ pJ/m}$ [78] in Equation 6.4 and $K_{\text{V, fcc}} = 0.04 \text{ MJ/m}^3$ [187] (and thus $K_{\text{S, fcc}} = 1.15 \text{ mJ/m}^2$). The dashed black line shows the behavior of $4\sqrt{A_{\text{ex}}K_{\text{eff}}}$ in the hcp system using $A_{\text{ex, hcp}} = 30 \text{ pJ/m}$ [78, 79] and $K_{\text{V, hcp}} = 0.5 \text{ MJ/m}^3$ [188] (and thus $K_{\text{S, fcc}} = 0.83 \text{ mJ/m}^2$). While the t -dependence of the (interface) anisotropy leads to a continuous reduction of the energy density with increasing Co thickness (dominates for Co coverages greater 1 ML), the t -dependence of the exchange stiffness derived in Equation 6.4 enforces a decrease of the energy density with decreasing film thickness (dominates for Co coverages smaller 1 ML). For fcc as well as for hcp, the term $4\sqrt{A_{\text{ex}}K_{\text{eff}}}$ is non-zero for Co thicknesses greater 0.5 ML, as at lower Co coverages A_{ex} is set to zero, as explained above. Comparing the Co-thickness dependence of the energy density of the fcc and hcp lattices shows that below 5 ML, the behavior is almost identical, meaning the effect of the increased exchange stiffness for hcp which leads to an increase of the energy density at low coverages, is counterweighted by the decreased interface anisotropy constant, which reduces the energy density. Above 5 ML Co, significant deviations between fcc and hcp arise due to the different values used for the interface anisotropy. As a consequence, also the spin-reorientation transition (SRT) is found at different Co thicknesses for fcc and hcp, as was already shown in Figure 6.6.

6.6. Discussion of the DMI strength based on a domain-size model

The second term of the domain-wall energy density γ_w given in Equation 6.3 is the stray-field energy of the volume charges of the domain wall. This term, shown as red solid line in Figure 6.7a), is only a small correction to γ_w and increases with the Co thickness for the here modeled case of pure Néel walls, as shown enlarged in the inset on the upper right. In dependence of the DMI strength, the transition from pure Néel walls to Néel walls with a Bloch contribution will take place at a certain Co thickness t_{NB} , above which the stray-field energy will decrease towards zero (due to $\cos \phi_{\pi \rightarrow \pm\pi/2} \rightarrow 0$ in Equation 6.3). This effect is not included in the here-presented simple model and is expected to have a negligible influence on the modelled domain-wall energy density, as already the contribution of the stray-field energy is comparatively small.

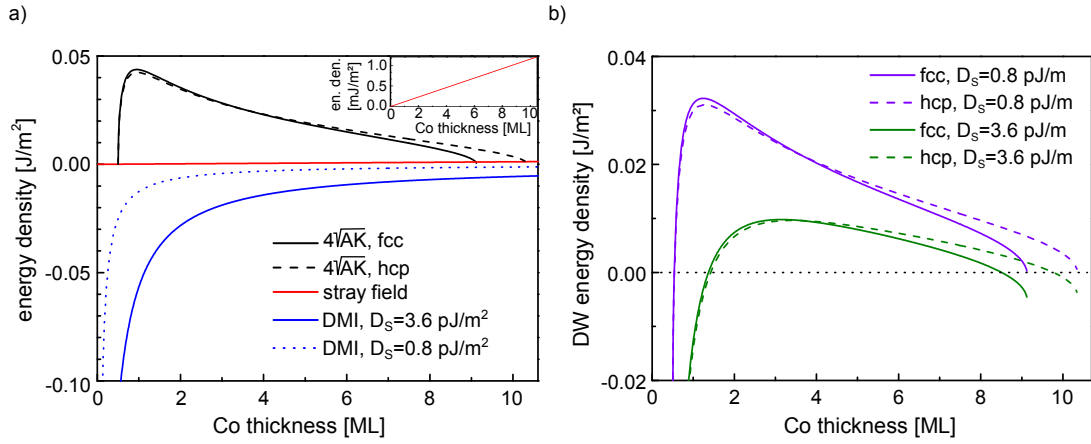


Figure 6.7: a) The three contributions to the domain-wall energy density γ_w in dependence of the Co thickness for Néel walls. The contribution of the exchange stiffness and the anisotropy is shown in black, the solid line represents the energy density of the fcc and the dashed line the one of the hcp Co system. The red solid line gives the energy contribution due to the stray field of the volume charges of the domain wall as derived by Tarasenko *et al.* [185]. It gives only a small contribution and is shown individually in the inset on the upper right with an appropriate ordinate in the lower mJ/m^2 range. The evolution of the DMI contribution is seen in blue. While the solid line gives the dependence for $D_S = 3.6 \text{ pJ/m}$, the dotted line shows the energy density for $D_S = 0.8 \text{ pJ/m}$. b) Adding up the three contributions, the thickness dependent domain-wall energy densities for fcc and hcp are derived and shown as solid and dashed line, respectively. For both lattices, the influence of the DMI is visualized by plotting the domain-wall energy density γ_w for a high DMI value of $D_S = 3.6 \text{ pJ/m}$ (green) as well as for a low DMI value of $D_S = 0.8 \text{ pJ/m}$ (purple). The dotted black line gives the zero line to highlight the transition from positive to negative values of γ_w .

The last term describes the contribution of the DMI to the domain-wall energy

density. The t -dependence of the micromagnetic DMI constant D_{DMI} is implemented via $D_{\text{DMI}} = D_{\text{S}}/t$ where D_{S} is the interfacial DMI constant [165, 191]. The behavior is shown for two different values of D_{S} . While the solid blue line shows the dependence for a comparatively high DMI value of $D_{\text{S}} = 3.6$ pJ/m, the dotted blue line shows the dependence for a weaker DMI strength of $D_{\text{S}} = 0.8$ pJ/m. As the DMI reduces the domain-wall energy, it arises as a negative contribution to γ_w that becomes more negative with increasing DMI strength. By adding up the three terms discussed above, the domain-wall energy density γ_w is obtained and is plotted in Figure 6.7b) for fcc and hcp, shown as solid and dashed line, respectively. For both lattices, the effect of the DMI is illustrated by plotting γ_w for a small interfacial DMI constant of $D_{\text{S}} = 0.8$ pJ/m, shown in purple, and for a high value of $D_{\text{S}} = 3.6$ pJ/m, shown in green. The two purple curves, solid and dashed for fcc and hcp, represent the weak DMI case and take on higher values of γ_w than the high-DMI case, shown in green. For all four dependences regimes with a negative domain-wall energy density arise. In these regimes, no stable domains will form in equilibrium, but spin spirals or a skyrmion lattice [192, 193]. For the low-DMI case (purple, $D_{\text{S}} = 0.8$ pJ/m), negative values of γ_w are found at thicknesses below 0.5 ML Co while for the high-DMI case (green, $D_{\text{S}} = 3.6$ pJ/m) negative domain-wall energy densities are observed below 1.4 ML Co. Experimentally, the first weak ferromagnetic contrast was observed at 1.5 ML. For the case of high-DMI, a second regime with negative values arises at Co thicknesses above 8.5 ML for fcc and 9.8 ML for hcp, in which spin spirals or skyrmions are predicted for the equilibrium state.

As introduced in Section 6.1 on page 76, *ab initio* calculations of the total DMI strength d_{tot} in Co/Pt(111) range from 2.7 to 3.6 meV per bond between Co atoms at the interface. These values are converted to D_{S} by making use of the above introduced relation between the micromagnetic DMI and the interfacial DMI constant $D_{\text{S}} = D_{\text{DMI}}t$, and the relation between the micromagnetic DMI and the total DMI strength $D_{\text{DMI}} = d_{\text{tot}}\sqrt{6}/(a_{\text{sub.}}t)$ [158] for a (111) interface with $a_{\text{sub.}}$ being the lattice constant of the substrate ($a_{\text{Pt}} = 3.912\text{\AA}$ [194]). Exemplarily, the total DMI strength of $d_{\text{tot}} = 3.6$ meV/Co converts to $D_{\text{S}} = 3.6$ pJ/m. The different values obtained from theory are inserted into the domain-size model and the resulting domain sizes are plotted in Figure 6.8 on a logarithmic scale. The model is shown for both, an fcc and an hcp lattice in Figure 6.8a) and b), respectively. While the blue dashed line gives the domain-size evolution in absence of DMI ($D_{\text{S}} = 0.0$ pJ/m), the four solid lines show the influence of the DMI strengths, as determined by Dupé *et al.* [147] (pink, $D_{\text{S}} = 3.6$ pJ/m), Freimuth *et al.* [160] (orange, $D_{\text{S}} = 2.7$ pJ/m), Vida *et al.* [159] (black, $D_{\text{S}} = 2.9$ pJ/m),

6.6. Discussion of the DMI strength based on a domain-size model

and Yang *et al.* [158, 161] (green, $D_S = 3.1$ pJ/m). The average domain sizes $d_{\text{Bodenberger}}$, which were determined for various Co thicknesses of the as-grown Co/Pt(111) system, are added as black spheres in both plots. Furthermore, the experimentally observed region of the SRT is shaded in blue.

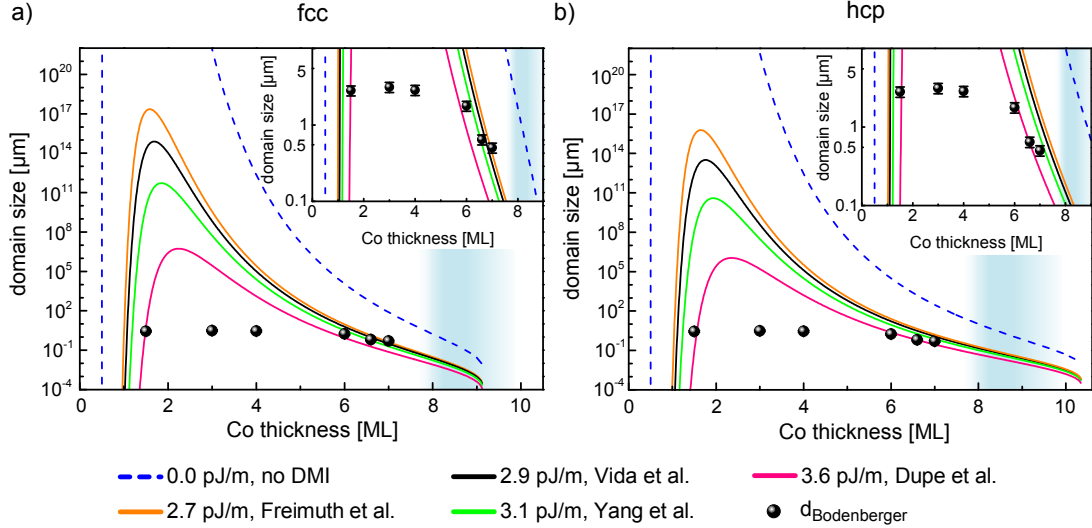


Figure 6.8: The domain-size evolution in dependence of the Co thickness according to the analytical model of Kaplan and Gehring is shown as lines for five different DMI values for both, the case of an fcc lattice in a), and an hcp lattice in b). The pink line shows the dependence for 3.6 pJ/m as found by Dupé *et al.* [147], orange for 2.7 pJ/m by Freimuth *et al.* [160], black for 2.9 pJ/m by Vida *et al.* [159], and green for 3.1 pJ/m by Yang *et al.* [158, 161]. In contrast, the blue dashed line gives the dependence for the case for 0.0 pJ/m, meaning no DMI. The domain sizes that were determined experimentally in the as-grown Co/Pt(111) system (see Figure 6.4b)) are added as black spheres. The experimentally observed region of the SRT, starting around 8 ML, is shaded in blue.

The domain-size evolutions that result for the different DMI values show the same characteristic features: At thin Co thicknesses the domain size increases steeply and reaches its maximum around 2 ML, before the domain size decreases again. This characteristic behavior of the domain size with increasing thickness of the magnetic film resembles the ones observed in thin films systems that are in, or close to, their equilibrium state [69, 195]. The model breaks down at the Co thicknesses of the SRT where the effective anisotropy K_{eff} becomes negative, as already discussed in context of the domain-wall energy density (see Figure 6.7). With decreasing DMI strength, the domain sizes increase. This behavior originates from the influence of the DMI to lower the domain-wall energy density, as visualized in Figure 6.7. While the peak domain size varies strongly with the

DMI value (note the logarithmic ordinate), domain sizes of a similar order of magnitude are predicted in the regimes between 1 and 1.5 ML, and between 6 ML and the SRT. As mentioned above, the domain-size model describes the system in its equilibrium state, whereas the investigated system was in its as-grown state. Thus, it cannot be expected that the experimentally obtained data show the same behavior as the theoretical model. Instead, deviations between theory (equilibrium) and experiment (as grown) are inevitable. Comparing the experimentally found domain sizes (black spheres) with the theoretical model (solid lines), following points are noticeable:

1. The first data point, showing the domain size at 1.5 ML Co, where the onset of ferromagnetism is found, coincides roughly with the modelled domain sizes, especially with the one for $D_S = 3.6$ pJ/m of Dupé *et al.*. This is independent of the assumed lattice type, as the domain-wall energy density is barely affected by the change in A_{ex} and K_{eff} for very thin films, as it was shown in Figure 6.7. Nevertheless, one has to keep in mind that the used t -dependent exchange stiffness $A_{\text{ex}}(n_{\text{Co}})$ is not very accurate for extremely low coverages, suggesting that this agreement between theory and experiment might be a coincidence and thus should not be used to derive physical quantities of the system.
2. A strong deviation of the experimentally determined domain sizes from the ones given by the model is found at 3 and 4 ML for both lattice types. As pointed out before (see page 85), the experimentally observed domain size is nearly constant in the range between 1.5 and 4 ML. This behavior is ascribed to the strong influence of the three-dimensional growth of the Co film on Pt(111), which is not covered completely within this thickness range. Thus, the domain size and shape is "frozen" into the Co film ("growth domains").
3. For film thicknesses above 6 ML, the experimentally determined decrease of the domain size follows the trend of the theoretical model. The observed significant change of the domain size above 6 ML suggests that the substrate is now completely covered with Co and thus, different energy contributions start to effectively compete with each other resulting in a change of the domain size, so that the latter approaches the equilibrium one. As the domain size shows a decrease instead of an increase, it is reasonable to conclude that the equilibrium domain size above 6 ML is smaller than the one experimentally observed at 4 ML. The experimentally determined

6.7. Summary

domain sizes above 6 ML fit within the assumption of an fcc lattice best to the models with a lower DMI between 2.7 and 3.1 pJ/m, and for an hcp lattice for the highest plotted DMI value of 3.6 pJ/m. Nevertheless, as the studied system is in the as-grown state, it is not likely to observe precisely the equilibrium domain size, but a larger one.

The goal in applying domain-size models to DMI-driven systems is usually to derive the DMI strength. As pointed out several times above, this ansatz needs to be treated with care, as the observed domain size is often not identical to the equilibrium domain size. Besides the beforehand-mentioned observation that at thin film thicknesses the experimentally derived domain sizes are smaller than the ones in equilibrium, at higher film thicknesses pinning of domains or domain walls can result in domains larger than in the equilibrium case. For the here investigated data set it can be assumed that the regime of "growth domains" whose size lies below the equilibrium domains ends below 6 ML Co, as above this film thickness a change, namely the decrease of the domain size, is observed. Thus, the three data points above 6 ML can be treated as upper limit of the equilibrium domain size—meaning the equilibrium domain size is smaller, or at most equal, to the observed domain sizes, but it can by no means be larger. From this line of thought and the above-derived domain-size model follows that the DMI strength in Co/Pt(111) can be expected to be larger than 2.7 pJ/m, as seen in Figure 6.8a). This lower bound is derived from the fcc case, while for a pure hcp lattice a larger lower bound of the DMI strength of about 3.5 pJ/m is found. Within the investigations performed here, no weighting of the hcp to fcc ratio present at higher Co thicknesses around 7 ML can be derived, which would allow to raise the lower bound. Expressing the lower bound in terms of total DMI results in $d_{\text{tot}} = 2.7 \text{ meV/Co}$.

6.7 Summary

In this chapter, the magnetic domain structure of a DMI system has been studied via SEMPA and the presence of Néel-like walls with a fixed rotational sense was found. The epitaxial UHV/Co/Pt(111) sample has been prepared by e-beam evaporation in a UHV chamber at RT. A LEED investigation of the surface of the Pt(111) crystal was performed to confirm its cleanliness before the evaporation. Satellites around the Pt (1x1) spots which arise in a sixfold symmetry are observed for thin Co thicknesses around 2 – 4 ML. The preparation conditions ensure that the interface between Co and Pt is as ideal as possible at

RT, making the prepared interface comparable to the ones studied in theoretical calculations. Tilting the sample during the SEMPA investigation allowed to admix the perpendicular magnetization component into the vertical magnetization channel, and thus the magnetization information from all three dimensions were accessible simultaneously. With increasing Co thickness, the perpendicularly magnetized domains, which start to appear at 1.5 ML, decrease their size until the SRT sets in around 8 ML. An analysis of the domain walls at 7 ML revealed the existence of Néel-like walls with an anticlockwise sense of rotation. This observation proves that the interfacial DMI plays an important role in the energy balance of the domain-wall energy even at a Co thickness as high as 7 ML (1.4 nm). The domain-size evolution of the Co/Pt(111) system in its equilibrium state was derived via the analytical model of Kaplan and Gehring. A careful comparison to the experimentally observed domain sizes of the as-grown sample allowed to derive a lower bound of the DMI strength of $D_S = 2.7$ pJ/m, which is equal to $d_{\text{tot}} = 2.7$ meV/Co.

6.8 Outlook

As pointed out in Section 6.6, additionally to the here-presented study of the Co/Pt(111) system, a quantitative analysis of the domain walls at 7 ML Co on Pt(111) was performed on this data set, see references [115, 153]. In this quantitative analysis, lower and upper bounds for the DMI strength of the 7 ML Co on Pt(111) system were derived. The found range of $0.8 < d_{\text{tot}} < 4.3$ meV/Co is in agreement with *ab initio* calculations predicting values between 2.7 and 3.6 meV/Co (see Section 6.1, page 76) as well as with the lower bound of 2.7 meV/Co found in this thesis.

The investigation of the DMI in the UHV/Co/Pt(111) system has been a crucial step towards a detailed understanding of the DMI in this system, which is highly valuable in regard to designing systems for future data storage devices. As mentioned in the beginning of this chapter, maximizing the DMI in Co-based systems is often achieved by sandwiching Co between Pt and Ir layers¹¹. The next step in extending the "toolkit"¹² of designing high-DMI systems lies in deepening the understanding of trilayer systems of these constituents, which again can be approached by studying the DMI in an epitaxial UHV/Co/Ir(111)

¹¹Due to the opposite sign of the DMI in Co/Pt and Co/Ir, the DMI strength of both interfaces in [Ir/Co/Pt] samples adds up so that the effective DMI strength increases.

¹²meaning the knowledge on preparation parameters and mechanisms and the corresponding effect on the resulting magnetic properties

6.8. Outlook

system. Kloodt-Twesten *et al.* [116]¹³ have just performed such an investigation. In contrast to the pure Néel walls in Co/Pt(111) which have been observed up to the onset of SRT [115, 116], a change in the domain-wall angle Φ with the Co thickness has been observed in Co/Ir(111) for Co thicknesses below the SRT, visualizing the transition from pure Néel walls towards walls with a partial Bloch contribution. Analyzing this thickness-dependent wall angle allowed a precise determination of the DMI strength, whose value is furthermore in agreement with theoretical predictions for the ideal Co/Ir interface.

¹³F. Kloodt-Twesten, S. Kuhrau, H.P. Oepen and R. Frömter. *Measuring the Dzyaloshinskii-Moriya interaction of the epitaxial Co/Ir(111) interface*. PRB **100**, 100402(R), (2019).

Cap-layer-dependent oxidation and magnetic contrast in SEMPA of ultrathin Co films

As discussed in the previous chapter, the DMI is not only a rising research field for scientific reasons but it is also inspiring for new approaches concerning future data storage devices. Though the previously introduced sample preparation via thermal evaporation (used for the Co/Pt(111) study, see Chapter 6) leads to a defined interface that is as ideal as possible, it is not the common method for the preparation of thin films in an industrial context, as it is a complex procedure that requires exceptionally clean working environments (UHV) as well as sample surfaces. An often used method to prepare single or multilayer stacks of thin films is sputter deposition. This technique offers the possibility of producing large quantities of samples with reproducible properties and is thus interesting for industrial applications.

Such magnetic data storage systems are in the need of a non-magnetic capping layer to prevent oxidation of the magnetic material. The same applies for ex-situ prepared samples that are intended to be investigated via SEMPA. Furthermore, this kind of protection layer serves simultaneously as a constituent that determines the interface anisotropy, and DMI. To avoid the need for such a capping layer, samples for a SEMPA investigation are often prepared in situ. In contrast, when studying ex-situ prepared systems in SEMPA, the surfaces are cleaned via ion milling and/or dusted with an ultrathin ferromagnetic layer before the investigation [16, 119, 121]. To gain an unrestricted applicability of SEMPA, it is highly desirable to establish a procedure that allows for the direct investigation of samples prepared ex-situ, meaning without any pre-treatment that might affect the sample. Especially the magnetic properties of those thin-film systems

that exhibit PMA are highly susceptible to any treatment by ions to remove the capping, and even to dusting. The ion impact of removing the cap by sputtering results in an intermixing that destroys the PMA in the system before even small amounts of the cap layer are removed. The approach of dusting the system with magnetic films affects the magnetic properties as well, as the active magnetic volume increases. On the other hand, cap layers, which typically are as thick as a few nm, result in a noteworthy reduction if not extinction of the magnetic contrast in SEMPA.

In this chapter, a new approach for the investigation of ex-situ prepared samples without any pre-treatment in SEMPA is presented. First, the ex-situ preparation of the [Pt/Co/Ir]₂ samples via magnetron sputtering is reported in Section 7.1. Hereafter, the influence of the cap-layer thickness on the magnetic contrast observed in SEMPA is discussed, as well as the related oxidation of the Co layer, see Section 7.2. Finally, a short summary and an outlook are given in Section 7.3 and 7.4, respectively.

Parts of the results presented in this chapter have been published in Applied Physics Letters 113, 172403 (2018) [196].

7.1 Ex-situ preparation via sputter deposition

For testing the new approach of imaging ex-situ prepared samples without any pre-treatment in SEMPA, the samples were grown via sputter deposition in a custom-build sputter chamber. The preparation of thin-film systems with the tools available in this chamber has been optimized during previous PhD theses, which included the investigation of the growth behavior as well as the resulting magnetic properties, especially concerning the Pt/Co/Pt system [197, 198]. The fundamentals of the two sputter techniques used are introduced in Section 7.1.1. A calibration of the deposition rates has been performed via X-ray reflectometry (XRR), see Section 7.1.3. Specifics on the preparation of the Pt/Co/Ir double layers are found in Section 7.1.2.

7.1.1 Preparation techniques

The studied Pt/Co/Ir double layer films are prepared ex situ in a sputter chamber. Two sputter techniques are used, namely the electron-cyclotron resonance (ECR) as well as the direct current (DC) magnetron sputtering. Figure 7.1 illustrates the working principles of both techniques. The ECR sputtering process, which is depicted in 7.1a), is based on the phenomenon that electrons in a static

7.1. Ex-situ preparation via sputter deposition

and homogeneous magnetic field \vec{B} are able to absorb energy resonantly from an electromagnetic microwave field. Due to the Lorentz force electrons in such a constant magnetic field move on a helical path, cycling with an angular frequency of $\omega_C = \frac{eB}{m_e}$, the so-called cyclotron frequency, where e denotes the charge of an electron and m_e its mass. As seen in Figure 7.1a), the plasma is generated in a separate plasma chamber (top left). The latter is made of ceramics and surrounded by a permanent magnet. Furthermore, it is directly connected to a gas inlet. A magnetron source, which operates at 2.45 GHz, generates microwaves, which are transferred into the plasma chamber via an antenna. The microwaves pump energy into the electrons, which ionize the Ar and create a plasma. The main chamber, which contains the sputter target as well as the substrate, is separated from the plasma chamber via a concave two-grid system. While the grid in contact with the plasma is held at +1.2 kV, defining the potential of the conductive plasma behind, the one facing the main chamber is grounded, just as the target. The Ar^+ ions are accelerated to the outer grid and fly towards the target to bombard it, so that atoms of the target are ejected.

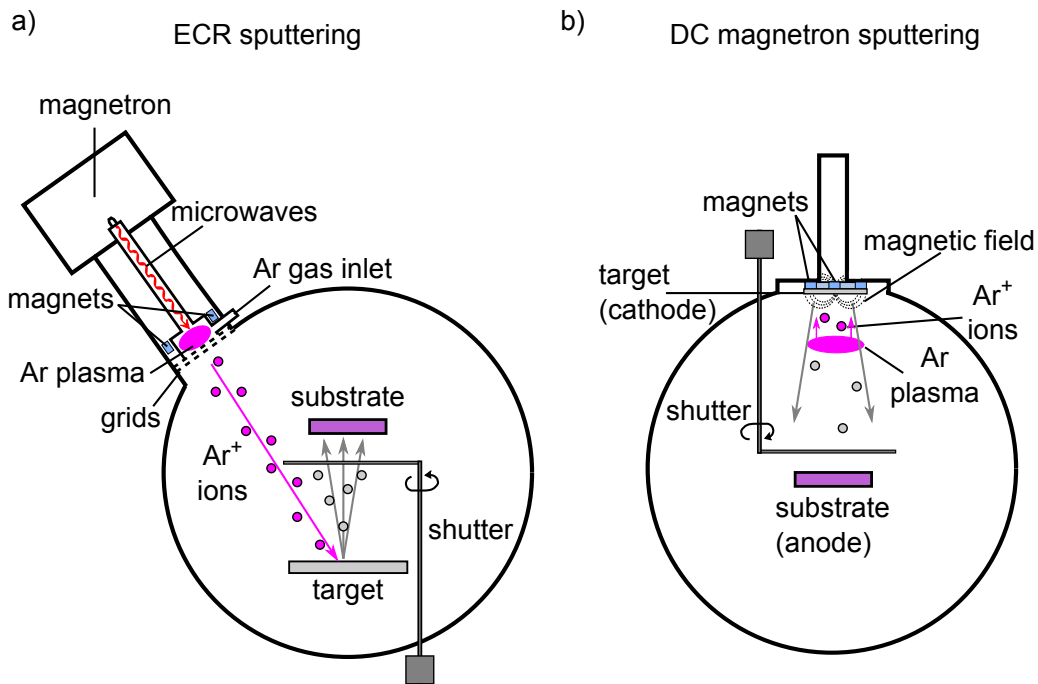


Figure 7.1: a) Schematic of the ECR sputtering technique. The Ar^+ ions are produced separately in the plasma chamber and accelerated to the outer grid, before they fly towards the target. b) Schematic of the DC magnetron sputtering technique. Due to the arrangement of the permanent magnets, the electrons move on a helical path in front of the target. This enhances the probability for the ionization of the Ar atoms. Adapted from [197].

The sputtered material is deposited on the substrate side facing the target. The Ar^+ ions from the plasma source hit the target at an angle of 45° . Reflected Ar^+ ions mostly leave the target at 45° (specular reflection) so that these, besides a few scattered ones, will not reach the substrate. The shutter between the target and the substrate is used to manually control the duration of the deposition.

In Figure 7.1b) the working principle of DC magnetron sputtering is illustrated. Contrary to ECR sputtering, the noble gas plasma is created directly in front of the sputter target. Therefore, the target is mounted in front of an arrangement of permanent magnets. These create a magnetic field in such a way that electrons are forced onto a helical trajectory in front of the target. Thus, the collision probability leading to an ionization of the used noble gas, in our case Ar, is strongly increased. Any ionized Ar atom provides another electron which again is able to create an Ar^+ ion. Thus, one single electron is able to ignite the plasma. The target is put on negative potential ($\approx -300\dots-500$ V) so that Ar^+ ions are accelerated onto it. The sputtered target material is then deposited onto a substrate, the desired deposition time is again controlled by the usage of a mechanical shutter.

The important difference between these two sputter techniques lies in the different kinetic energies of the sputtered atoms - both, leaving the target and arriving at the substrate. The atoms leaving the target that have been sputtered via ECR have an average kinetic energy of about 30 eV, those sputtered via the DC magnetron of about 20 eV [198]. While the Ar pressure of $p_{\text{Ar}} = 3 \cdot 10^{-4}$ mbar during ECR sputtering results in a mean free path of about 20 cm, the higher pressure of $p_{\text{Ar}} = 3 \cdot 10^{-3}$ mbar during DC magnetron sputtering leads to a mean free path of about 2 cm [199]. The ECR target is positioned with a distance of 5 cm from the substrate, thus the mean free path is greater than the distance between target and substrate. The sputtered atoms thus reach the substrate without colliding with gas atoms, and therefore do not lose kinetic energy. In contrast, the target to substrate distance for the DC magnetron sputtering equaling 10 cm is greater than the above derived mean free path. Due to one or several collisions, the sputtered atoms lose kinetic energy on their way to the substrate and thus arrive with low energies at the latter.

7.1.2 Sample preparation

The Pt/Co/Ir films have been grown onto a Si_3N_4 substrate (200 nm Si_3N_4 on Si wafer, *Si-Mat*). The base pressure in the sputter chamber, which is shown in Figure 7.2a), is $< 2 \cdot 10^{-9}$ mbar. A 4 nm thick Pt-seed layer is created by means

7.1. Ex-situ preparation via sputter deposition

of ECR sputtering ($p_{\text{Ar}} = 3 \cdot 10^{-4}$ mbar) on top of the Si_3N_4 substrate before the Pt/Co/Ir layers are deposited via DC sputtering ($p_{\text{Ar}} = 3 \cdot 10^{-3}$ mbar). This combination of ECR and DC sputtering has been found to enhance the PMA in the sample system [200]. Due to the before mentioned high energy of the Ar^+ ions in ECR sputtering and the different working pressure, the mobility of the sputtered Pt atoms is enhanced, which allows for an ordered, energetically favorable arrangement of the atoms on the substrate [200]. Thus, the polycrystalline Pt-seed layer exhibits a (111) texture [201]. It serves as a template for the growth of the (111)-textured fcc [202] ultrathin $[\text{Pt}/\text{Co}/\text{Ir}]_2$ films that are grown on top of the seed layer via DC magnetron sputtering. The usage of DC instead of ECR sputtering in the latter case is crucial, as it reduces intermixing at the interfaces [202].

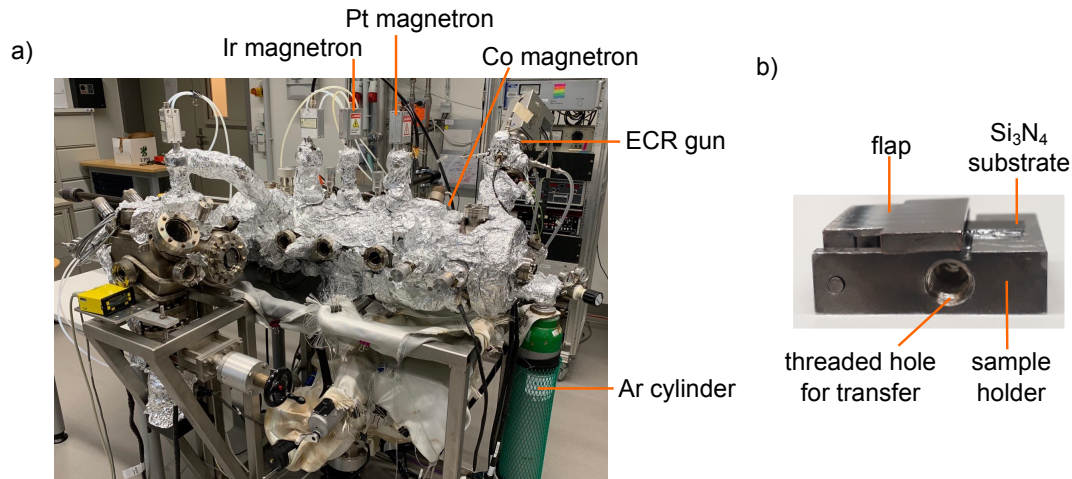


Figure 7.2: a) Photograph of the sputter deposition chamber. The positions of the Ir, Pt and Co magnetrons are indicated, as well as the ECR gun which is used to prepare the (111)-textured Pt-seed layer. The Ar cylinder is seen on the right. b) Sample holder used for the creation of a wedge. The flap, which is attached to the sample holder, is shown in its closed position, partially covering the substrate mounted below.

The Pt-seed layer created via ECR sputtering was deposited at a rate of 0.071 nm/s, the used acceleration voltage of the Ar^+ ions was set to 1.2 kV. During the DC sputtering, the Ar^+ ion current at the target was monitored and kept fixed (Ir: 20 mA, Co: 50 mA, Pt: 30 mA). The applied high voltage varied slightly for each preparation process due to abrasion at the sputter targets. For Ir, the Ar^+ ions were accelerated to an energy of 460-480 eV, for Co to 290-310 eV and for Pt to 420-440 eV. The resulting deposition rates for these three materials are 0.021 nm/s for Ir, 0.025 nm/s for Co and 0.048 nm/s for Pt.

In the investigations presented in the following, different sample types have been prepared. Studying the Pt-cap-layer thickness dependent magnetic contrast and the correlated oxidation process of the Co is achieved by preparing Pt/Co/Ir double layer films whose final Pt layer is wedged. The wedge is created by using the penumbra of a flap in front of the sample, see Figure 7.2b). To reassure that the coupling between the two Co layers does not influence the magnetic signal observed in SEMPA, the Ir/Pt-interlayer thickness is varied for different samples as will be discussed in Section 7.2.4.

7.1.3 Calibration via X-ray reflectometry

The deposition rates are calibrated via XRR measurements, which offer a non-destructive method to determine, among others, the film thickness of single and multilayers. An X-ray beam reflects from a sample at grazing incidence and the specular X-ray reflectivity R , which describes the ratio of the reflected to the incident intensity, is detected. Detailed information on the technique and the underlying physical fundamentals can be found in [203–205].

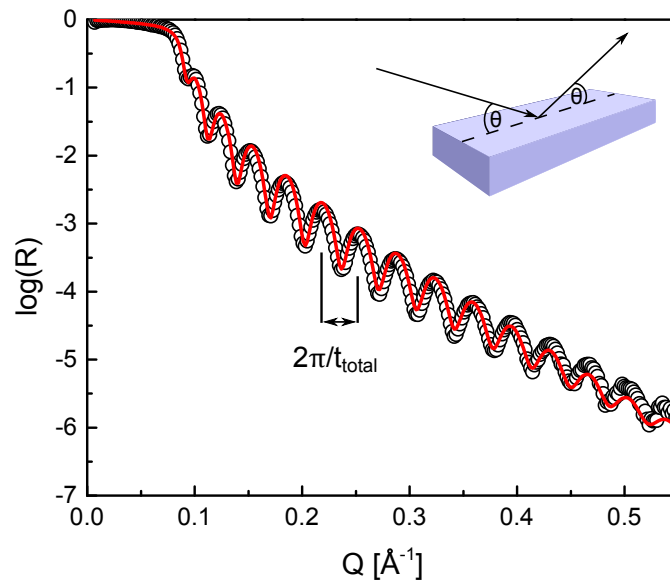


Figure 7.3: XRR data (specular reflectivity R versus momentum transfer Q) of an Ir film on Si_3N_4 is shown as black open circles. The least square fit using Abelès formalism is shown as a red line and yields an Ir film thickness of 17.1 nm. The error, obtained from the fit, of the film thickness for this single layer sample is $< 0.4\%$.

The XRR data used for the calibration of the sputter deposition rates were taken at the XRD 3003 PTS (Seifert) instrument of the Helmholtz-Zentrum Geestacht which uses radiation at a wavelength of $\lambda = 1.54 \text{ \AA}$ (Cu K_α). The

7.2. Cap-layer-thickness dependent Co oxidation and its influence on the magnetic contrast

reflectivity R was measured over a Q range from 0.01 \AA^{-1} to 0.7 \AA^{-1} , where $Q = 4\pi \sin \theta / \lambda$ describes the momentum transfer and θ the angle of incidence. Figure 7.3 shows the XRR data of an Ir film on Si_3N_4 which were analyzed with the Motofit package [206] developed for IGOR Pro [207]. It uses the Abelès matrix method [208] to fit the specular reflectivity R . The observed oscillations, known as "Kiessig fringes" [209], result from interference between reflections of X-rays from different interfaces. The thickness of a single-layer film can be calculated from the momentum difference ΔQ_{total} between two oscillation maxima via

$$t_{\text{total}} = \frac{2\pi}{\Delta Q_{\text{total}}},$$

as indicated in Figure 7.3.

7.2 Cap-layer-thickness dependent Co oxidation and its influence on the magnetic contrast

For the investigation of the magnetic contrast in dependence of the Pt-cap-layer thickness, the final Pt layer has been prepared as a wedge. Furthermore, the correlation between the cap thickness and the Co oxidation has been studied for thin Pt-cap-layer thicknesses. A sketch of an exemplary sample composition is given in Figure 7.4. Two kinds of samples with varied Ir/Pt-interlayer thickness have been prepared separately, as will be discussed later on in this section. The transfer of the samples from the sputter chamber to the out-of-plane SEMPA is associated with an exposure to ambient conditions for 5-10 min. After the SEMPA investigation, the sample is transferred to a standard SEM to investigate the local surface composition along the wedge by means of energy dispersive X-ray spectroscopy (EDX) line scans. Finally, an atomic force microscope (AFM) is used to determine the surface morphology of the oxidation process in dependence of the Pt-cap-layer thickness.

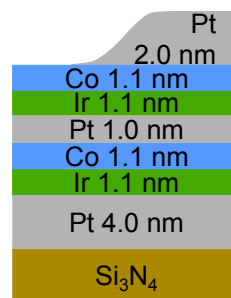


Figure 7.4: Exemplary sketch of a $[\text{Pt}/\text{Co}/\text{Ir}]_2$ sample composition with wedged Pt cap. Taken from [196].

7.2.1 EDX analysis of the $[\text{Pt}/\text{Co}/\text{Ir}]_2$ samples

The local surface composition of the $[\text{Pt}/\text{Co}/\text{Ir}]_2$ films is determined by means of EDX line scans. These scans were performed along the Pt wedge at normal

incidence with a primary electron energy of 6 keV and a detection angle 65° off normal. Later on, the results of the EDX analysis will be used to correlate the magnetic contrast obtained by SEMPA measurements with the Pt-cap-layer thickness (see Section 7.2.3). Figure 7.5 gives the integrated and background-corrected count rates of the emission peaks of platinum M (blue), cobalt L (black) and oxygen K (red) along the wedge, which give the amount of the three constituents along the Pt wedge. Please note that the EDX analysis also found Si, N, Ir and C, which are not shown in Figure 7.5 as they do not contain any issue-related information for the investigation of the oxidation in dependence of the Pt-cap-layer thickness.

The platinum trace (blue) shows a sigmoidal shape. This form is characteristic for wedges that were grown by the penumbra technique from an extended source, as used here. Fitting by an error function (fit in magenta) yields a 2σ -width of $w_{\text{Pt}} = (216 \pm 7) \mu\text{m}$. Knowing that the two plateaus on the left and right correspond to the uncovered Co side and the side with the 2 nm Pt-cap layer, respectively, a conversion into Pt-cap-layer thickness is given at the right axis.

The oxygen profile, shown in red, also reveals a sigmoidal shape on top of some background. The same oxygen background is measured at a Pt film that has been directly sputtered onto a Si_3N_4 substrate, prompting that it originates from a small amount of oxygen or oxygen compounds that are adsorbed onto the surface. A decrease of the intensity of the oxygen signal is observed with increasing Pt thickness, indicating an increasing protection against oxidation upon thickness increase of the cap layer. A detailed inspection of the reduction of the oxygen intensity shows that its decrease starts at about 0.15 nm Pt coverage, thus shortly after the onset of the Pt wedge, and is already completed at about 1 nm Pt thickness. This area has been highlighted by a red shading in the plot. It indicates that already at about half the prepared wedge thickness a closed Pt film is obtained that protects the underlying Co film against oxidation. A further increase of the Pt-cap layer does not reduce the oxygen content anymore. An error function fit (green) yields a width of $w_{\text{O}} = (78 \pm 18) \mu\text{m}$ for the observed oxygen wedge, which is centered at about 0.5 nm Pt. The conversion into oxygen atoms/ nm^2 seen on the right axis, which will allow a quantitative discussion, will be derived later on.

Contrary to the previous two EDX traces, the trace of Co, which is shown in black, is almost flat. A small reduction of the measured Co intensity by $\sim 4\%$ on the Pt-capped side compared to the uncapped site is found and can be ascribed to X-ray absorption by the platinum on top. The detected Co L_α emission is

7.2. Cap-layer-thickness dependent Co oxidation and its influence on the magnetic contrast

associated with an X-ray energy of 776 eV and the attenuation length in platinum at this energy equals 60 nm [210]. Thus, upon the 2 nm thick Pt-cap layer a signal loss of 3.33% is indeed to be expected.

Above the plot of the EDX signals (Figure 7.5), the change of the SE contrast along the same wedge is shown. The brightness evolution follows the sigmoidal shape of the Pt and is observed in all studied samples. In case no EDX is available, the Pt thickness can thus be determined via the SE contrast.

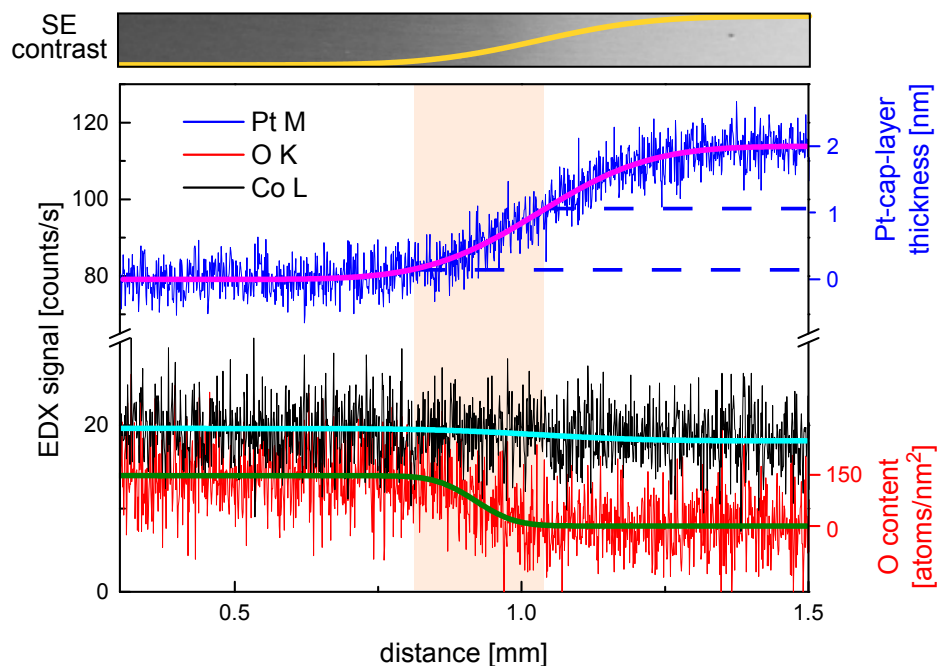


Figure 7.5: The EDX line scan along the Pt wedge shows the traces of platinum, cobalt and oxygen. Platinum as well as oxygen show a sigmoidal shape, while the cobalt trace is almost flat. The red shaded area highlights the area of the oxygen wedge. A conversion into Pt-cap-layer thickness to nm as well as for the oxygen content to atoms/nm² is given at the right axis. The image stripe above the plot shows the SE contrast change along the wedge. The brightness along the image, plotted in yellow, correlates with the sigmoidal behavior of the Pt signal. Adapted from [196].

7.2.2 Quantitative analysis of the polarization contrast

For the cap-layer-thickness-dependent investigation of the magnetic contrast a series of magnetization images has been taken with SEMPA along the Pt wedge. Acquisition times of 90 min for the 300x300 pixel images were used as the polarization values are expected to be small due to contamination and/or Pt coverage. A typical domain image obtained in the out-of-plane component is

shown in Figure 7.6a), taken at a cap-layer thickness of 1.1 nm. The image shows a maze domain pattern and has a signal-to-noise ratio of 4.

Figure 7.6b) displays the corresponding histogram of measured asymmetry values in this image. The asymmetry measured in the black or white domains gives the the separation of the two peaks which equals in this case about 3%. As quantification for the magnetic contrast, half of the difference between the average asymmetry values in these domains pointing up and down will be used (here $\pm 1.5\%$) and denoted as ΔA . The quantity ΔA is referenced to zero spin polarization and is thus equivalent to the asymmetry radius A_r as defined by Frömter *et al.* in reference [117]. It is important to note that independent of the Pt-cap thickness studied here, no in-plane component could be found within the error margin.

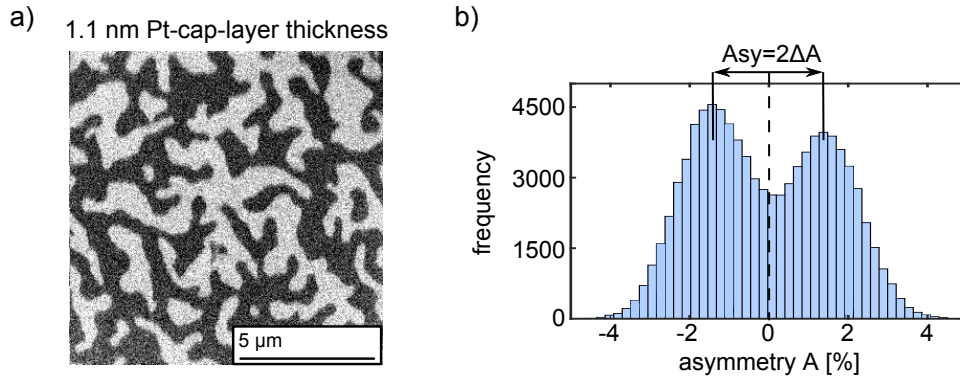


Figure 7.6: a) The image of the out-of-plane magnetization at a Pt-cap-layer thickness of 1.1 nm shows a maze domain pattern. The corresponding histogram of the asymmetry of this image is shown in b). The two visible maxima correspond to the black and white domains. As a measure for the magnetic contrast we use half of the difference between both maxima, denoted as ΔA . Adapted from [196].

7.2.3 The dependence of the magnetic contrast on the Pt thickness

To draw conclusions for the thickness-dependent investigation of the magnetic contrast, a correlation of the position of the SEMPA measurement and the Pt-cap-layer thickness at this spot is essential. As mentioned in Section 7.2.1, EDX line scans were performed to obtain the local surface composition along the wedge. These line scans as well as the SEMPA measurements result in a darkening of the scanned areas, probably due to the deposition of cracked residual gas molecules [211, 212]. This darkening is seen in the SEM micrograph in

7.2. Cap-layer-thickness dependent Co oxidation and its influence on the magnetic contrast

Figure 7.7. On top, the stripe of the EDX line scan is visible, while in the lower part several square shaped areas due to SEMPA measurements can be recognized. This contamination of the sample surface is often an undesired effect observed in electron microscopy, but in the present case it can be used to correlate the local surface composition from the EDX analysis with the positions of SEMPA measurements. It thus allows to determine the magnetic contrast as function of the Pt-cap-layer thickness.

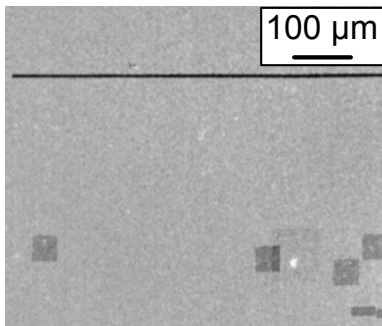


Figure 7.7: The SE micrograph shows several darkened areas due to the EDX line scan (stripe on the top) and the SEMPA investigation (squares in the lower part). Adapted from [196].

Figure 7.8 shows the measured magnetic contrast values in dependence of the Pt-cap-layer thickness as black squares. The upper x-axis gives the dependence to the oxygen content, which is derived later on in Section 7.2.5. The magnetic contrast increases in the range from 0 to 0.8 nm Pt-cap thickness and decreases exponentially above 1 nm. At low Pt coverage, the increase of the magnetic contrast obviously originates from the increasing protection against oxidation. The latter results in a greater portion of unoxidized Co that contributes to the asymmetry signal. The decrease of the magnetic contrast above 1 nm Pt on the other hand is attributed to the increasing spin scattering at higher thicknesses of the Pt-cap layer. The maximum of the measured magnetic contrast is thus observed around a Pt-cap thickness of 1 nm, giving a sufficiently high magnetic contrast that allows for high-quality imaging. No additional pre-treatment is needed to obtain this contrast, meaning the ex-situ prepared sample is directly imaged after transfer into UHV. A model to describe the magnetic contrast as function of the cap-layer thickness is derived below. It accounts for both effects introduced above and is fitted to the experimentally determined magnetic contrast, which are shown as black squares in Figure 7.8, as red line.

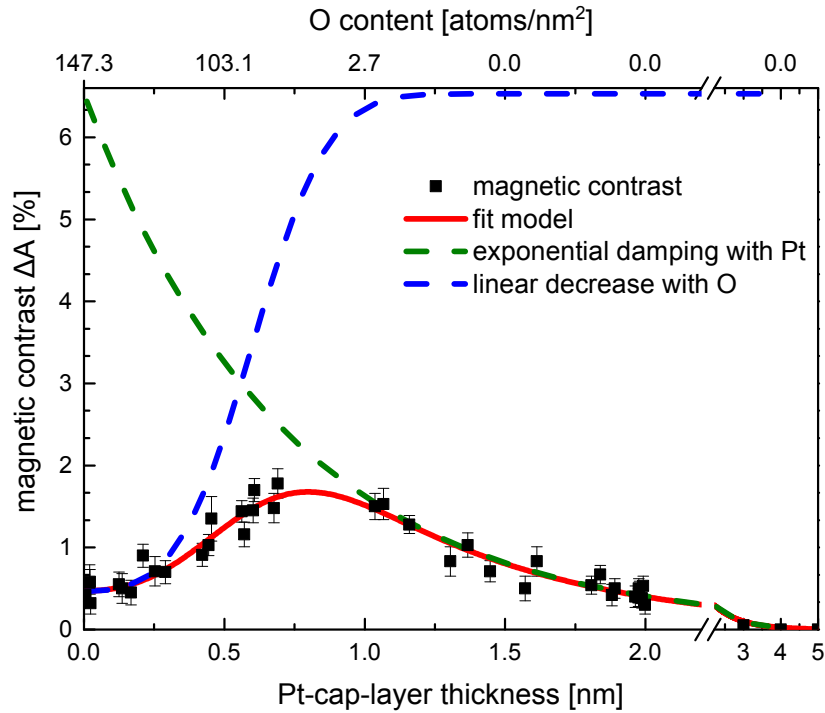


Figure 7.8: Magnetic contrast (black squares) in dependence of the thickness of the Pt-cap layer (bottom abscissa) as well as the corresponding oxygen content (top abscissa). The red solid line is a fit of a model (given in Equation 7.1) to describe the thickness dependent contrast. This model takes both effects into account, the exponential reduction of the magnetic contrast that originates from spin scattering at Pt (green dashed line) and the increase of the contrast that stems from vanishing oxidation (blue dashed line) due to a more effective protection of the Co by the Pt capping. Three additional asymmetry values are shown after the break of the x-axis. They were obtained by investigating samples with constant, but higher thicknesses of the Pt-cap layer, and are in accordance with the model. Adapted from [196].

As concluded from the EDX line scans, above 1 nm of the Pt-cap layer the Co is completely covered and no oxidation takes place. Thus, the decrease of the magnetic contrast above 1 nm is ascribed to the increasing Pt thickness and the resulting effect of spin scattering within Pt. This effect is modeled via a simple exponential decay, which is fitted to the magnetic contrast above 1 nm and is plotted as green dashed line. Correcting for the latter exponential decrease in the data, the obtained data points fall on the blue dashed line. This sigmoidal curve begins at a slight offset (about 0.3 %) and reaches a plateau of 6.5 % at a Pt-cap-layer thickness of 1.1 nm. Furthermore, the blue dashed line can be well described when a reduction of the polarization asymmetry is assumed that is proportional to the oxygen intensity detected in the EDX measurement.

7.2. Cap-layer-thickness dependent Co oxidation and its influence on the magnetic contrast

To deduce a model for the observed behavior of the magnetic contrast, the additional oxygen content detected in the EDX line scan (see Figure 7.5) is parametrized as function of the Pt thickness $c_{\text{oxy}}(t_{\text{Pt}})$ on a scale from 0 to 1. With this, the following fit function for the magnetic contrast can be formulated

$$\Delta A(t_{\text{Pt}}) = a \cdot (1 - b \cdot c_{\text{oxy}}(t_{\text{Pt}})) \exp\left(\frac{-t_{\text{Pt}}}{\tau}\right), \quad (7.1)$$

with a , the magnetic contrast of a pure unoxidized Co film, b the reduction of the magnetic contrast at maximum oxidation (zero Pt coverage) ranging from 0 (full contrast) to 1 (no contrast), and τ the exponential spin-decay length of the capping Pt film. Fitting to the data results in $a = (6.5 \pm 1.3) \%$, $b = 0.938 \pm 0.022$ and $\tau = (0.72 \pm 0.07) \text{ nm}$. An asymmetry of 6.5 % appears reasonable for a clean, thin film of Co. Deducing from the asymmetry of Fe measured in the in-plane SEMPA [117] and the saturation magnetizations of Co and Fe [81] one could expect a magnetic contrast for bulk Co of roughly

$$\Delta A(\text{Co}_{\text{bulk}}) = \left(\frac{\Delta A(\text{Fe})}{M_{\text{S}}(\text{Fe})}\right) \cdot M_{\text{S}}(\text{Co}) = \frac{8.6 \text{ \%}}{1717 \text{ kA/m}} \cdot 1447 \text{ kA/m} = 7.2 \text{ \%}. \quad (7.2)$$

Taking into consideration that at this position the Co film has only a thickness of 1.1 nm and assuming a magnetic information depth of 0.8 nm for Co [213], one finds

$$\Delta A(\text{Co}_{1.1 \text{ nm}}) = 7.2 \text{ \%} \cdot \left(1 - \exp\left(\frac{-1.1 \text{ nm}}{0.8 \text{ nm}}\right)\right) = 5.4 \text{ \%}. \quad (7.3)$$

The derived spin-decay length $\tau = 0.72 \text{ nm}$ lies in the same order of magnitude as values reported for the magnetic information depths of Fe, 0.63 nm [15], or Ni, 0.4 – 1.1 nm [16, 213]. Please note that in contrast to the spin-diffusion length¹ at the Fermi level, this spin-decay length applies to electrons with an energy roughly 6 – 10 eV above the Fermi level, as only these electrons are detected in SEMPA after passing over the work function barrier of the sample into vacuum. The fact that the parameter b , which describes the reduction of the magnetic contrast at maximum oxidation, is not equal to 1 (complete loss of magnetic signal) but slightly smaller, results from the tiny magnetic contrast that is observed at the uncovered Co side. Speculations, that this magnetic contrast is not associated with the upper Co layer but originates from the second, buried Co layer can easily be disproved. As will be shown in Section 7.2.4, and has already been mentioned in the introduction to this chapter, the coupling between the two Co layers can be tuned from antiferro- to ferromagnetic via minor changes

¹The spin-diffusion length equals the mean distance that electrons diffuse between spin-flip collisions.

of the Ir/Pt-interlayer thickness. In both cases, meaning for antiferro- as well as ferromagnetic coupling, the dependence of the magnetic contrast from the Pt-cap-layer thickness shows the same behavior which is seen in Figure 7.8. In case the antiferromagnetic coupling had an influence on the detected contrast, a reduction of the magnetic contrast towards zero at a compensation thickness $t_{\text{comp}} > 0$ nm would be expected. As this is not observed, it follows that the polarization signal originates from the topmost Co layer. The mere existence of this small magnetic contrast at the uncovered Co side implies that the topmost Co film (though uncovered) is not completely oxidized. The degree of oxidation will be discussed in Section 7.2.5.

7.2.4 Tuning the interlayer coupling from ferro- to antiferromagnetic

Two kinds of [Pt/Co/Ir]₂ samples have been prepared for the investigation of the cap-layer-thickness dependent behavior of the magnetic contrast: Those with a ferromagnetic coupling as well as some with antiferromagnetic coupling between the Co layers. As introduced in Section 3.5, the coupling between the two Co layers can be modulated to be either antiferromagnetic or ferromagnetic by changing the thickness of the non-magnetic interlayer. The influence of a non-magnetic interlayer composed of Pt and/or Ir sandwiched between Co has been extensively studied in the PhD thesis of J. Wagner [69], whose work inspired the preparation of samples with different IEC in this study.

Two exemplary magnetization curves, obtained by employing the magneto-optic Kerr effect (MOKE) [214, 215], of [Pt/Co/Ir]₂ samples with varied Pt/Ir-interlayer thickness are shown in Figure 7.9. The samples studied with MOKE did not have a wedged cap layer, but a closed 2-nm thick Pt-cap layer. They were prepared simultaneously with the wedged samples by attaching another Si₃N₄ substrate at a position of the sample holder which is not shadowed by the flap (see Figure 7.2b), page 103). The magnetization curve seen in 7.9a) shows a clear ferromagnetic coupling of the two Co layers. The total thickness of the non-magnetic spacer is 1.8 nm. On the contrary, the magnetization curve presented in 7.9b) belongs to a sample with 2.2 nm interlayer thickness, and exhibits a clearly antiferromagnetic behavior. The coupling constant for the antiferromagnetic case can be calculated via Equation 3.15. The switching field of $H_{\text{sf}} \simeq 28$ mT, the saturation magnetization of $M_{\text{S}}(\text{Co}) = 1.44$ MA/m and the thickness of the Co layers of $t_{\text{Co}} = 1.1$ nm lead to $J_{\text{IEC}} \simeq -0.044$ mJ/m².

7.2. Cap-layer-thickness dependent Co oxidation and its influence on the magnetic contrast

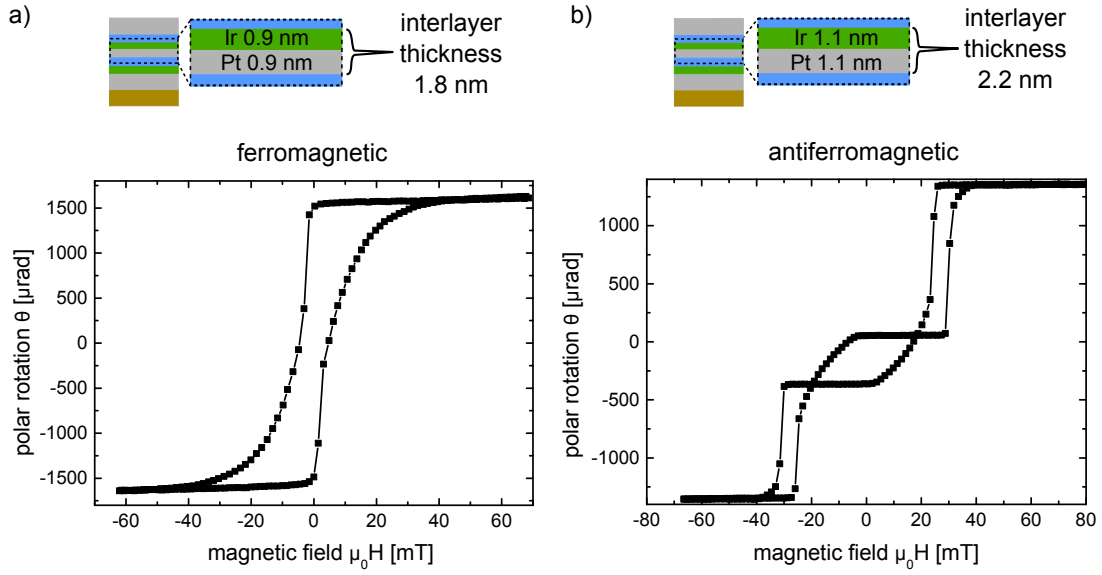


Figure 7.9: Magnetization curves of two $[\text{Pt}/\text{Co}/\text{Ir}]_2$ samples with different interlayer thickness. a) The sample with a non-magnetic interlayer of 1.8 nm thickness shows ferromagnetic coupling of the Co layers. b) Antiferromagnetic coupling is observed for the sample with a 2.2 nm-thick interlayer. The switching field of $H_{\text{sf}} \simeq 28.0$ mT results in $J_{\text{IEC}} \simeq -0.044$ mJ/m².

7.2.5 Investigation of the Co oxidation

In order to quantify the amount of oxidized Co that is present in the topmost Co layer, a calibration of the EDX system has been performed by using a naturally oxidized silicon wafer. The thickness of the SiO_2 layer was determined via ellipsometry measurements to be as thick as $t_{\text{SiO}_2} = 2.7$ nm, which is equivalent to 125 oxygen atoms per nm² surface area. This conversion is given via the formula

$$\frac{\# \text{ atoms}}{\text{area}} = \frac{\rho}{M} \cdot N_{\text{A}} \cdot t \cdot n \quad (7.4)$$

using the molar mass of SiO_2 $M(\text{SiO}_2) = 60$ g/mol and N_{A} the Avogadro constant. As density ρ for the naturally oxidized silicon a value of ~ 2.3 g/cm³ [216] can be expected². The factor n accounts for the stoichiometry. As two oxygen atoms are bound in one SiO_2 molecule, $n = 2$ in the calculation above.

The count rate of the oxygen (K) peak, which was detected via EDX on the naturally oxidized Si wafer, amounts to 5.2 Cts/s. In the $[\text{Pt}/\text{Co}/\text{Ir}]_2$ samples one Co layer is 1.1 nm thick and thus consists of 100 Co atoms/nm² (Equation

²The density of SiO_2 strongly varies among its different modifications. The highest value is reported for the α -quartz SiO_2 with a density of 2.65 g/cm³[170]. Naturally oxidized SiO_2 on the other hand is polycrystalline which results in a lower density.

7.4 with $\rho(\text{Co})=8.90 \text{ g/cm}^3$, $M(\text{Co})=59 \text{ g/mol}$, $n = 1$).

The oxygen K background obtained on the 2 nm Pt reference film is used to correct the oxygen data (from EDX) along the wedge. After this step, the measured oxygen content is converted into quantitative units, namely oxygen atoms per nm^2 , by utilizing the presented calibration via SiO_2 . Comparing the oxygen content detected on the capped to the uncapped side, an increase in the oxygen count rate of 6.2 Cts/s is found at the uncovered Co surface (see EDX plot in Figure 7.5), which is equal to an oxygen coverage of 147.3 oxygen atoms per nm^2 . Furthermore, the information depth obtained in EDX is much larger than the thickness of the studied film of a several nm, and thus, it is straightforward to assume that the measured oxygen count rates are proportional to the oxygen content. This thesis was confirmed by performing Monte Carlo simulations [174] of the EDX experiments. Tompkins *et al.* [217] found that a clean surface of bulk Co forms an 8 – 10 Å thick surface layer of $\text{Co}(\text{OH})_2$ ³ within less than 1 s when exposed to ambient conditions. A discussion to what extent the assumption (formation of $\text{Co}(\text{OH})_2$) fits to experimental results observed in literature as well as in this thesis will be given further down.

Following the assumption that indeed $\text{Co}(\text{OH})_2$ with an O/Co ratio of $n = 2$ has formed on top of the here investigated sample, the measured count rate of 6.2 Cts/s indicates that the equivalent of 4 ML of Co (= 0.8 nm Co) are oxidized

$$t_{\text{Co}} = \frac{M(\text{Co}) \cdot \frac{\text{O atoms/area}}{n}}{\rho(\text{Co}) \cdot N_{\text{A}}} \quad (7.5)$$

Considering the density of $\text{Co}(\text{OH})_2$, this results in an effective thickness of 3.2 nm $\text{Co}(\text{OH})_2$ ⁴. Knowing that 4 ML (0.8 nm) Co have been oxidized, it can be directly concluded that in the upper 1.1 nm-thick Co layer a remaining equivalent of only 1.5 ML Co (= 0.3 nm Co) stays unoxidized, and is therefore the origin of the observed non-vanishing magnetic contrast at the uncovered side. In the following, a more quantitative understanding of the magnetic contrast at the uncapped side will be derived. The remaining contrast is equal to the factor $a \cdot (1 - b)$ as can be directly seen in Equation 7.1, with a the magnetic contrast of a pure, unoxidized Co film, and b the reduction of the magnetic contrast at maximum oxidation. Considering the remaining amount of unoxidized Co, two limiting cases can be derived. On the one hand, a full spatial segregation of oxidized and unoxidized Co patches can be assumed, or on the other hand a homogeneous oxidation from top downwards can be expected. For both cases, a corresponding

³The samples were investigated in X-ray photoelectron spectroscopy (XPS).

⁴ $\rho(\text{Co}(\text{OH})_2)=3.6 \text{ g/cm}^3$ [170], $M(\text{Co}(\text{OH})_2)=93 \text{ g/mol}$

7.2. Cap-layer-thickness dependent Co oxidation and its influence on the magnetic contrast

value of b can be derived. For the first case of a full spatial segregation of oxidized and unoxidized patches, in which also an identical secondary electron yield is assumed for both surfaces, the magnetic contrast can be expected to scale like the unoxidized Co ratio, and thus follows

$$b_{\text{full segregation}} = 1 - (0.3 \text{ nm}/1.1 \text{ nm}) \simeq 0.73. \quad (7.6)$$

The second limiting case that assumes a homogeneous oxidation from top downwards, gives

$$b_{\text{homo. oxidation}} = 1 - \frac{(1 - \exp(-0.3 \text{ nm}/0.8 \text{ nm}))}{(1 - \exp(-1.1 \text{ nm}/0.8 \text{ nm}))} \simeq 0.58, \quad (7.7)$$

assuming an information depth in Co of 0.8 nm [213]. The experimentally derived value of $b = 0.938$ is significantly higher, meaning the observed magnetic contrast at the uncovered Co side is lower, than estimated from these limiting cases that are solely based on the $\text{Co}(\text{OH})_2$ stoichiometry, . Further contributions to the experimentally observed reduction of the magnetic contrast are expected to origin from spin scattering in the hydroxide layer on top of the remaining Co, as well as from a reduction of the Co magnetization due to finite-size effects. These effects cannot be easily quantified, but assuredly lead to an additional reduction of the measured spin polarization.

To investigate further whether the assumption of the formation of $\text{Co}(\text{OH})_2$ is reliable, a sample that was stored for six months under ambient conditions is studied via EDX. For such a sample, a complete oxidation of the upper Co layer can be assumed. The EDX investigation revealed the presence of 206 oxygen atoms/nm² at the uncovered side (100 Co atoms/nm² in a 1.1 nm thick layer), which reflects the exact stoichiometric amount of oxygen atoms for the 2:1 ratio, supporting the assumption that $\text{Co}(\text{OH})_2$ has formed. The exclusive formation of other known states of oxidation, like CoO, Co_2O_3 or Co_3O_4 that have been observed at elevated temperatures [217, 218], or using UHV-dosed O_2 [219, 220] can thus be ruled out. It may be noted that within the here-performed measurements it can also not be deduced evidently, that $\text{Co}(\text{OH})_2$ is exclusively formed, instead of a layer which is composed of a mixture of (hydr-)oxides. $\text{Co}(\text{OH})_2$ is a hydroxide that is paramagnetic ($\chi=0.013$) at RT [221], and thus will not contribute to the experimentally derived magnetic contrast, which is in agreement with the model proposed above. It may be noted that Smardz *et al.* [222] who studied the oxidation kinetics of thin and ultrathin Co films at air claim that a CoO layer forms on top of their Co samples. While Tompkins *et al.* [217] proved the formation of $\text{Co}(\text{OH})_2$ via X-ray photoelectron spectroscopy (XPS),

Smardz *et al.* solely refer to a study [223] in which the chemisorption of oxygen on Co was investigated in an oxygen-dosed UHV setup via the electron energy loss fine structure (EELFS) technique, meaning the samples were not exposed to ambient conditions. Within their investigation at 4.5 K, Smardz *et al.* conclude that an antiferromagnetic surface layer forms on top of Co. This finding agrees with their assumption of an CoO surface layer which has a Néel temperature of $T_N=291$ K [76], but it does not contradict the existence of $\text{Co}(\text{OH})_2$ which is also antiferromagnetic at this temperature [221].

For the investigation of the morphology of the (hydr-)oxide that have formed on the partially covered Co (thin Pt-cap coverages below 1 nm), a series of images of the topology have been taken with an AFM along the wedge. Figure 7.10a) shows height maps that were obtained at four different thicknesses of the Pt-cap layer. The bare oxidized Co surface with a 0.0 nm thick Pt-cap layer is seen in the left panel and appears rough. This roughness is presumed to originate from the inhomogeneous oxidation to $\text{Co}(\text{OH})_2$. The other three panels show the height maps with increasing Pt-cap thickness in which flat Pt islands appear. These islands lead to a reduction of the area in which the oxidation of the underlying Co can take place, as they leave only patches of uncovered Co at which the $\text{Co}(\text{OH})_2$ oozes out. With increasing Pt-cap layer thickness the coverage with Pt islands increases and the islands start to coalesce. For Pt coverages above a nominal film thickness of 0.9 nm, an entirely smooth surface is observed, indicating a closed Pt film. The RMS roughness has been extracted from the $1 \times 1 \mu\text{m}^2$ height maps taken by AFM and is plotted versus the oxygen content as black dots in Figure 7.10b). A comparably rough surface of 4.5 \AA is observed on the oxidized Co side, while the Pt-covered side is rather smooth and yields a roughness of 1.2 \AA . Plotting the roughness as function of position reveals the same sigmoidal trend that was observed in the oxygen profile, thus a rather linear decrease of the roughness with decreasing oxygen content is observed. A black dashed line is added as guide to the eye in Figure 7.10b) to emphasize this linear trend. In addition to the AFM measurements, high-resolution SEM images (InLens SE detector, working distance 2.7 mm) were taken along the Pt wedge to assess the surface morphology. The according micrographs are added as grayscale insets in Figure 7.10a) and reveal a similar change in the morphology as observed via AFM. While the AFM measurements allowed for an investigation which did not affect the sample perceivably, the detected SE contrast was not stable under electron bombardment. The visibility of the observed structures vanished quickly and thus a detailed analysis by means of SEM was not possible.

7.3. Summary

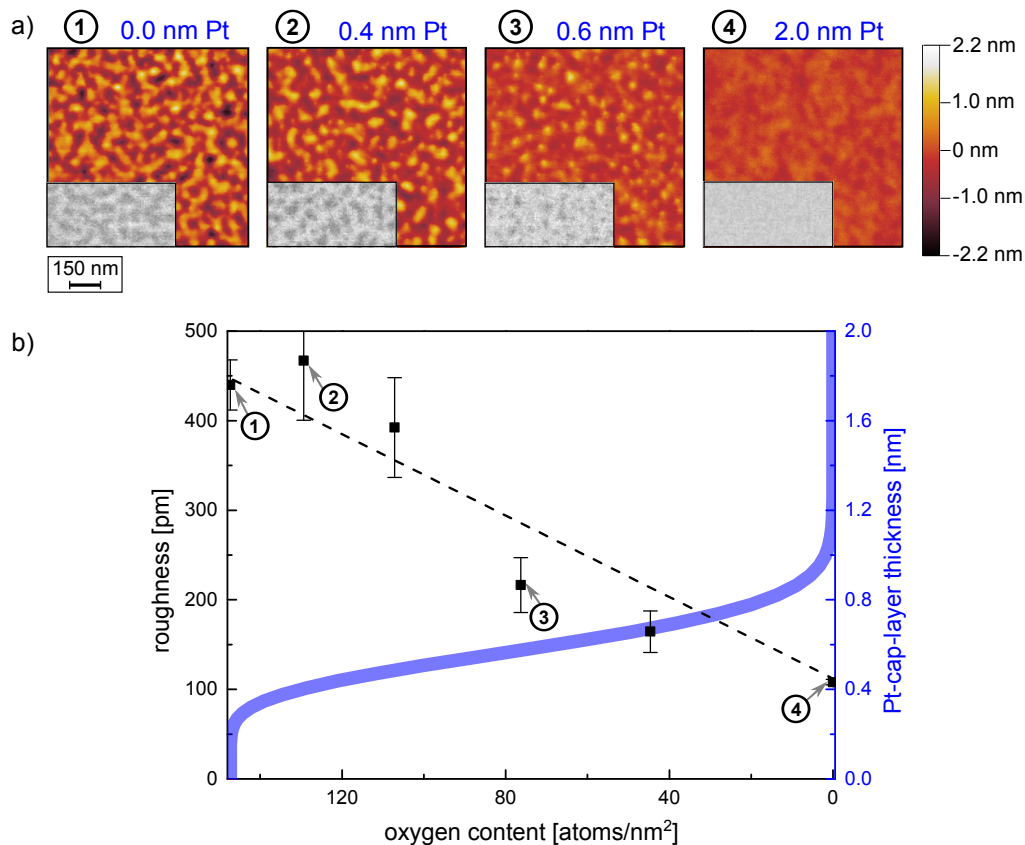


Figure 7.10: a) Height maps taken with AFM along the Pt wedge of the sample, the respective Pt-cap thickness is given on top of the images. The insets show SEM micrographs that were taken at the corresponding Pt thicknesses. b) The plot shows the roughness (RMS) that was determined from the AFM measurements as black squares in dependence of the oxygen content. The black dashed line is added as a guide to the eye. Additionally, the above found correlation between the thickness of the Pt-cap layer (right axis) and the oxygen content is given as blue line. Adapted from [196].

7.3 Summary

The dependence of the magnetic contrast of a Co thin film on the thickness of a Pt-cap layer was studied. Therefore, the cap layer of the ex-situ prepared sample was built as a wedge. An investigation via SEMPA was performed after exposure to ambient conditions for several minutes. An EDX investigation reveals that an effective protection of the Co against oxidation is obtained for Pt-cap-layer thicknesses above 1 nm. A sufficiently high magnetic asymmetry of 1.5 % is found at a Pt-cap thickness of 1.1 nm which equals about $\frac{1}{4}$ of magnetic contrast that is expected from clean Co. Furthermore, a spin-decay length of 0.7 nm was derived

for electrons in Pt whose energies lie roughly 6 – 10 eV above the Fermi level. Thus, it was demonstrated that investigations on ex-situ prepared samples can be performed via SEMPA without the need of any pre-treatments like ion milling or dusting. The study presents a new approach on handling delicate thin film multilayers in surface-sensitive magnetic imaging. Furthermore, the oxidation process of bare Co has been investigated. Quantitative EDX measurements were used to determine the stoichiometry between Co and oxygen, and suggest that the uncapped Co oxidized to $\text{Co}(\text{OH})_2$. $\text{Co}(\text{OH})_2$ is a paramagnetic hydroxide whose formation reduces the amount of ferromagnetic material which is in agreement with the decrease of the magnetic contrast that is observed on the uncovered Co side. Investigations via AFM as well as SEM reveal a change of morphology due to the oxidation. Both methods show that the oxidized (uncovered) side is rough, while the Pt-covered side maintains a flat surface. With increasing thickness of the Pt-cap layer, Pt islands grow and coalesce until at an effective Pt coverage of 0.9 nm a flat surface is observed. The growth of the Pt islands is accompanied with an increasing protection of the Co against oxidation, which leads to a continuous increase of the magnetic signal.

7.4 Outlook

The presented study opens a path for the surface-sensitive examination of the magnetism via SEMPA of various types of ex-situ prepared sputtered samples, which will be especially relevant for industrial applications. Regarding the $[\text{Pt}/\text{Co}/\text{Ir}]_2$ system, two interesting leads for further investigations may be pointed out. On the one hand, a study concerning the DMI in this system is obvious and of great interest. In the here-studied samples, the domain walls of the at most 5.5 ML thick Co layer were too narrow to allow for a quantitative analysis of the DMI as it was performed in references [115, 116]. Using a cap layer of 1.1 nm and preparing the underlying Co layer as a wedge might allow for a rough estimation of the DMI strength via domain-size models, as discussed in Chapter 6. Qualitatively, it was possible to observe domain walls of Néel type with a fixed clockwise sense of rotation, see Figure 7.11a). The latter magnetization image was taken at a Pt/Co/Ir single layer film at a Pt-cap-layer thickness of about 0.85 nm. The color-coded image visualizes the fixed sense of rotation as it reveals along the positive y-direction (vertical in-plane component) the consecutive sequence of green \rightarrow yellow \rightarrow red \rightarrow blue which is equal to a clockwise rotation (see color wheel on the lower right). One approach to obtain a detailed insight on the DMI in this specific system is the preparation of a sample with a

7.4. Outlook

Co wedge that is capped with 1.1-nm Pt to prevent oxidation. Furthermore, a direct comparison of the Pt/Co/Ir system, which has been epitaxially grown on a single crystal, with a sputtered one is evident.

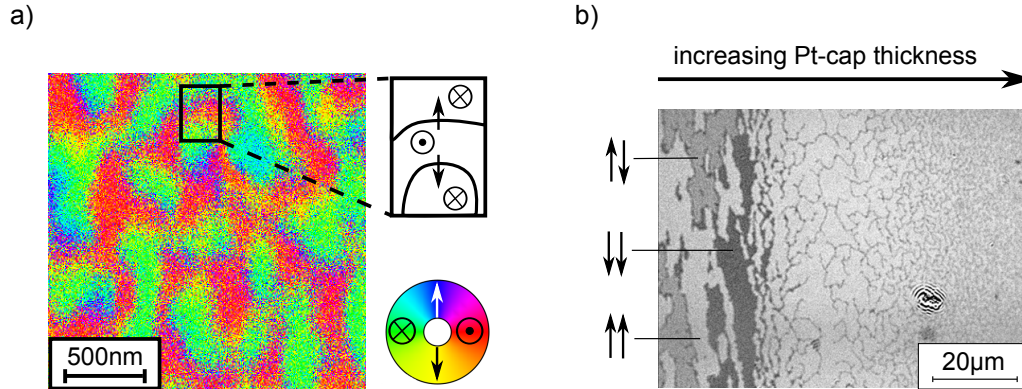


Figure 7.11: a) Color-coded image of the magnetization in a Pt/Co/Ir single layer at a Pt-cap-layer thickness of about 0.85 nm. The observed in-plane component along the y -direction visualizes the existence of domain walls of Néel type with a fixed clockwise sense of rotation: While moving along the positive y -direction, a consecutive sequence of the colors green \rightarrow yellow \rightarrow red \rightarrow blue is observed. b) Magnetization image with perpendicular sensitivity obtained via Kerr microscopy at an antiferromagnetically coupled Pt/Co/Ir double layer. The appearance of a third gray level appears to be correlated with a partially antiparallel coupling of the Co layers. The arrows on the left indicate a possible alignment of the magnetization in the two magnetic layers. Though the Pt-cap thickness increases from left to right, the explicit thickness of the Pt layer is unknown for the performed measurements. A magnetic field of $B_{\text{ext}} = 50$ mT was applied under an angle of 78° to the normal of the sample, which results in a component along the surface normal of about $B_{\text{ext},\perp} = 19$ mT.

The second lead worthwhile investigating includes a comprehensive study via Kerr microscopy (see Section 2.5). In contrast to SEMPA, which is only sensitive to the magnetization in the upper monolayers of the sample, the information depth of 5 – 10 nm in Kerr microscopy allows to investigate the magnetization of both Co layers. In a short test study, three gray levels were observed in Kerr images, as can be seen in Figure 7.11b). It was noticeable that this three-level behavior was exclusively present in the samples with antiferromagnetic coupling. The conclusion that a correlation to the antiferromagnetic coupling exists is thus plausible. A correlation of the position studied in the Kerr microscope with the thickness of the Pt cap, and thus the degree of oxidation, is needed for the interpretation. Furthermore it has to be noted that for the measurement presented in Figure 7.11b), a magnetic field was applied that has been tilted

Chapter 7. Cap-layer-dependent oxidation and magnetic contrast in SEMPA of ultrathin Co films

by 78° in respect to the samples normal (details on Kerr microscopy in this setting can be found in reference [224]). The discussion whether the in-plane component of the external field contributes to the observed behavior can be examined by the usage of a magnetic field which is aligned solely parallel to the sample normal. Besides the above-mentioned difference in the information depth between SEMPA and Kerr microscopy, it may be pointed out that while in SEMPA the as-grown state was investigated, magnetic-field sweeps are applied in Kerr microscopy.

Bibliography

- [1] C. Razy, *Étude analytique des petits modèles de métiers exposés au musée des tissus* (Lyon, France: Musée historique des tissus, 1913)
- [2] <https://www.ibm.com/ibm/history/ibm100/us/en/icons/floppy/breakthroughs/>
- [3] https://www.seagate.com/www-content/investors/_shared/docs/tech-talk-mark-re-20150825.pdf
- [4] <https://www.backblaze.com/blog/hdd-vs-ssd-in-data-centers/>
- [5] <https://www.backblaze.com/blog/ssd-vs-hdd-future-of-storage/>
- [6] <https://uk.pcmag.com/ssd/8061/ssd-vs-hdd-whats-the-difference>
- [7] M. Gu, X. Li, and Y. Cao, «Optical storage arrays: a perspective for future big data storage», *Light: Science & Applications* **3**, e177 (2014)
- [8] C. Vogler, C. Abert, F. Bruckner, D. Suess, and D. Praetorius, «Areal density optimizations for heat-assisted magnetic recording of high-density media», *Journal of Applied Physics* **119**, 223903 (2016)
- [9] A. D. Kent and D. C. Worledge, «A new spin on magnetic memories», *Nature nanotechnology* **10**, 187 (2015)
- [10] A. Fert and P. M. Levy, «Role of anisotropic exchange interactions in determining the properties of spin-glasses», *Physical Review Letters* **44**, 1538 (1980)

-
- [11] A. Vanhaverbeke and M. Viret, «Simple model of current-induced spin torque in domain walls», [Physical Review B](#) **75**, 024411 (2007)
- [12] S. Parkin and S.-H. Yang, «Memory on the racetrack», [Nature Nanotechnology](#) **10**, 195 (2015)
- [13] A. Fert, V. Cros, and J. Sampaio, «Skyrmions on the track», [Nature Nanotechnology](#) **8**, 152 (2013)
- [14] N. Romming, C. Hanneken, M. Menzel, J. E. Bickel, B. Wolter, K. von Bergmann, A. Kubetzka, and R. Wiesendanger, «Writing and deleting single magnetic skyrmions», [Science](#) **341**, 636 (2013)
- [15] K. Koike, «Spin-polarized scanning electron microscopy», [Microscopy](#) **62**, 177 (2013)
- [16] D. L. Abraham and H. Hopster, «Magnetic probing depth in spin-polarized secondary electron spectroscopy», [Physical Review Letters](#) **58**, 1352 (1987)
- [17] M. J. Fransen, J. S. Faber, T. L. van Rooy, P. C. Tiemeijer, and P. Kruit, «Experimental evaluation of the extended Schottky model for ZrO/W electron emission», [Journal of Vacuum Science & Technology B: Microelectronics and Nanometer Structures Processing, Measurement, and Phenomena](#) **16**, 2063 (1998)
- [18] H. P. Oepen, G. Steierl, and J. Kirschner, «Scanning electron microscope with polarization analysis: Micromagnetic structures in ultrathin films», [Journal of Vacuum Science & Technology B: Microelectronics and Nanometer Structures Processing, Measurement, and Phenomena](#) **20**, 2535 (2002)
- [19] M. von Ardenne, «Improvements in electron microscopes», (1937), british patent no. 511204
- [20] L. Qing, *Zur Frühgeschichte des Elektronenmikroskops* (Verlag für Geschichte der Naturwissenschaften und der Technik, Stuttgart, 1995)
- [21] J. Kirschner, «Spin polarization of secondary electrons from Fe(110) excited by unpolarized primary electrons», [Surface Science](#) **273**, 147 (1992)
- [22] T. Koshikawa and R. Shimizu, «A Monte Carlo calculation of low-energy secondary electron emission from metals», [J. Phys.D: Appl. Phys.](#) **7**, 1303 (1974)
-

References

- [23] K. Zakeri, T. Peixoto, Y. Zhang, J. Prokop, and J. Kirschner, «On the preparation of clean tungsten single crystals», [Surface Science Letters](#) **604** (2010)
- [24] L. Reimer, [Scanning Electron Microscopy](#) (Springer-Verlag Berlin Heidelberg New York, 1998)
- [25] L. Reimer and G. Pfefferkorn, [Rasterelektronenmikroskopie](#) (Springer-Verlag Berlin Heidelberg, 1977)
- [26] C. Kunz, [Photoemission in Solids II](#), chap. Synchrotron Radiation: Overview (Springer-Verlag Berlin, 1979)
- [27] W. Gerlach and O. Stern, «Der experimentelle Nachweis der Richtungsquantelung im Magnetfeld», [Zeitschrift für Physik](#) **9**, 349 (1922)
- [28] G. Uhlenbeck and S. Goudsmit, «Ersetzung der Hypothese vom unmechanischen Zwang durch eine Forderung bezüglich des inneren Verhaltens jedes einzelnen Elektrons», [Naturwissenschaften](#) **13**, 953 (1925)
- [29] J. Kessler, [Polarized Electrons](#) (Springer-Verlag Berlin Heidelberg, 1985)
- [30] J. Kirschner, [Polarized Electrons at Surfaces](#) (Springer-Verlag Berlin Heidelberg New York Tokyo, 1985)
- [31] K. Koike and K. Hayakawa, «Scanning electron-microscope observation of magnetic domains using spin-polarized secondary electrons», [Japanese Journal of Applied Physics](#) **23**, L187 (1984)
- [32] M. Scheinfein, D. Pierce, J. Unguris, J. McClelland, R. Celotta, and M. Kelley, «Improved low-energy diffuse scattering electron-spin polarization analyzer», [Review of Scientific Instruments](#) **60**, 1 (1989)
- [33] H. Oepen and J. Kirschner, «Imaging of magnetic microstructures at surfaces: The scanning electron microscope with spin polarization analysis», [Scanning Microscopy](#) **5**, 1 (1991)
- [34] A. Takayama, [High-Resolution Spin-Resolved Photoemission Spectrometer and the Rashba Effect in Bismuth Thin Films](#), chap. Basic Principle of Photoemission Spectroscopy and Spin Detector, pp. 15–30 (Springer Japan, Tokyo, 2015)
- [35] D. Pierce and R. Celotta, «Spin Polarization in Electron Scattering from Surfaces», pp. 219 – 289 (Academic Press, 1981)

-
- [36] J. Unguris, D. T. Pierce, and R. J. Celotta, «Low-energy diffuse scattering electron-spin polarization analyzer», [Review of Scientific Instruments](#) **57**, 1314 (1986)
- [37] M. M. Matthias Escher, Nils B. Weber, «FERRUM: A new highly efficient spin detector for electron spectroscopy», [e-Journal of Surface Science and Nanotechnology](#) **9**, 340 (2011)
- [38] W. Demtröder, *Experimentalphysik 3: Atome, Moleküle und Festkörper*, chap. Das Wasserstoffatom, pp. 141–176 (Springer Berlin Heidelberg, Berlin, Heidelberg, 2016)
- [39] N. F. Mott and N. H. D. Bohr, «The scattering of fast electrons by atomic nuclei», [Proceedings of the Royal Society of London. Series A, Containing Papers of a Mathematical and Physical Character](#) **124**, 425 (1929)
- [40] J. Kirschner and R. Feder, «Spin polarization in double diffraction of low-energy electrons from W(001): Experiment and theory», [Physical Review Letters](#) **42** (1979)
- [41] R. Frömter, H. Oepen, and J. Kirschner, «A miniaturized detector for high-resolution SEMPA», [Applied Physics A](#) **76**, 869 (2003)
- [42] W. Weinberg and R. Merrill, «A LEED investigation of the chemisorption of nitrous oxide on a tungsten (100) surface», [Surface Science](#) **32**, 317 (1972)
- [43] S. Rößler, «Magnetic imaging of static and dynamic states in systems of reduced dimensions», (talk at University Hamburg, 2015), PhD defense
- [44] S. Rößler, *Magnetic imaging of static and dynamic states in systems of reduced dimensions*, Ph.D. thesis, Universität Hamburg (2015)
- [45] Z. Qui and S. Bader, «Surface magneto-optic Kerr effect», [Review of Scientific Instruments](#) **71**, 1243 (2000)
- [46] M. Grimsditch and P. Vavassori, «The diffracted magneto-optic Kerr effect: what does it tell you?», [Journal of Physics: Condensed Matter](#) **16**, R275 (2004)
- [47] A. Barman, S. Wang, J. D. Maas, A. R. Hawkins, S. Kwon, A. Liddle, J. Bokor, and H. Schmidt, «Magneto-optical observation of picosecond dynamics of single nanomagnets», [Nano Letters](#) **6**, 2939 (2006)
-

References

- [48] A. Neudert, J. McCord, D. Chumakov, R. Schäfer, and L. Schultz, «Small-amplitude magnetization dynamics in permalloy elements investigated by time-resolved wide-field Kerr microscopy», *Physical Review B* **71**, 134405 (2005)
- [49] A. Petford-Long and J. Chapman, *Lorentz Microscopy*, pp. 67–86 (Springer Berlin Heidelberg, Berlin, Heidelberg, 2005)
- [50] A. T. N'diaye and A. Quesada, *Spin-Polarized Low-Energy Electron Microscopy (SPLEEM)*, pp. 1–14 (American Cancer Society, 2012)
- [51] P. A. Midgley and R. E. Dunin-Borkowski, «Electron tomography and holography in materials science», *Nature Materials* (2009)
- [52] R. Frömter, F. Klodt, S. Röfler, A. Frauen, P. Staeck, D. R. Cavicchia, L. Bocklage, V. Röbisch, E. Quandt, and H. P. Oepen, «Time-resolved scanning electron microscopy with polarization analysis», *Applied Physics Letters* **108**, 142401 (2016)
- [53] N. R. da Silva, M. Möller, A. Feist, H. Ulrichs, C. Ropers, , and S. Schäfer, «Nanoscale mapping of ultrafast magnetization dynamics with femtosecond Lorentz microscopy», *Physical Review X* **8**, 031052 (2018)
- [54] H. Hopster and H. P. Oepen, *Magnetic Microscopy of Nanostructures* (Springer Berlin Heidelberg, 2005)
- [55] A. Schwarz, M. Bode, and R. Wiesendanger, *Scanning Probe Techniques: MFM and SP-STM* (American Cancer Society, 2007)
- [56] A. Gruber, A. Dräbenstedt, C. Tietz, L. Fleury, J. Wrachtrup, and C. von Borczyskowski, «Scanning confocal optical microscopy and magnetic resonance on single defect centers», *Science* **276**, 2012 (1997)
- [57] P. Maletinsky, S. Hong, M. Grinolds, B. Hausmann, M.D.Lukin, R.L.Walsworth, M.Loncar, and A. Yacoby, «A robust scanning diamond sensor for nanoscale imaging with single nitrogen-vacancy centres», *Nature Nanotechnology* (2012)
- [58] D. Caldwell, J. M. Thorne, and H. Eyring, «Magnetic circular dichroism», *Annual Review of Physical Chemistry* **22**, 259 (1971)
- [59] P. J. Stephens, «Magnetic circular dichroism», *Annual Review of Physical Chemistry* **25**, 201 (1974)

-
- [60] W. Kuch, *Magnetic Imaging*, pp. 275–320 (Springer Berlin Heidelberg, Berlin, Heidelberg, 2006)
- [61] B. Pfau and S. Eisebitt, *Synchrotron Light Sources and Free-Electron Lasers: Accelerator Physics, Instrumentation and Science Applications*, chap. X-Ray holography (Springer, 2014)
- [62] P. Aitchison, J. Chapman, V. Gehanno, I. Weir, M. Scheinfein, S. McVitie, and A. Marty, «High resolution measurement and modelling of magnetic domain structures in epitaxial FePd (001) L10 films with perpendicular magnetisation», *Journal of Magnetism and Magnetic Materials* **223**, 138 (2001)
- [63] D. Cooper, J.-P. Barnes, J.-M. Hartmann, A. Béché, and J.-L. Rouviere, «Dark field electron holography for quantitative strain measurements with nanometer-scale spatial resolution», *Applied Physics Letters* **95**, 053501 (2009)
- [64] T. Niermann, M. Lehmann, and T. Wagner, «Gated interference for time-resolved electron holography», *Ultramicroscopy* **182**, 54 (2017)
- [65] S. Loth, M. Etzkorn, C. P. Lutz, D. M. Eigler, and A. J. Heinrich, «Measurement of fast electron spin relaxation times with atomic resolution», *Science* **329**, 1628 (2010)
- [66] J. Jeske, D. W. M. Lau, X. Vidal, L. P. McGuinness, P. Reineck, B. C. Johnson, M. W. Doherty, J. C. McCallum, S. Onoda, F. Jelezko, T. Ohshima, T. Volz, J. H. Cole, B. C. Gibson, and A. D. Greentree, «Stimulated emission from nitrogen-vacancy centres in diamond», *Nature Communications* (2017)
- [67] R. Tromp, J. Hannon, A. Ellis, W. Wan, A. Berghaus, and O. Schaff, «A new aberration-corrected, energy-filtered LEEM/PEEM instrument. I. Principles and design», *Ultramicroscopy* **110**, 852 (2010)
- [68] W. Chao, B. D. Harteneck, J. A. Liddle, E. H. Anderson, and D. T. Attwood, «Soft x-ray microscopy at a spatial resolution better than 15 nm», *Nature* **435**, 1210 (2005)
- [69] J. Wagner, *The magnetic properties of ultrathin cobalt multilayers symmetrically and antisymmetrically sandwiched between layers of platinum and iridium*, Ph.D. thesis, Universität Hamburg (expected 2019)
-

References

- [70] R. Wiesendanger, *Scanning Probe Microscopy and Spectroscopy: Methods and Applications* (Cambridge University Press, 1994)
- [71] R. M. Reeve, H.-J. Elmers, F. Büttner, and M. Kläui, «Magnetic imaging and microscopy», [arXiv 1806.07767v2](#) (2018)
- [72] A. Hubert and R. Schäfer, *Magnetic Domains* (Springer Berlin Heidelberg, 1998)
- [73] S. Blundell, *Magnetism in Condensed Matter* (Oxford University Press, 2001)
- [74] R. O'Handley, *Modern magnetic materials: Principles and applications* (John Wiley & Sohns, 2000)
- [75] H. Kronmüller and S. Parkin, *Handbook of magnetism and advanced magnetic materials* (John Wiley & Sons, Hoboken, N.J., 2007)
- [76] C. Kittel, *Introduction to solid state physics* (John Wiley & Sons, 1976)
- [77] A. Aharoni, *Introduction to the Theory of Ferromagnetism* (Oxford University Press, 1996)
- [78] H. A. Alperin, O. Steinsvoll, G. Shirane, and R. Nathans, «Observation of the dispersion relation for spin waves in hexagonal cobalt», [Journal of Applied Physics](#) **37**, 1052 (1966)
- [79] S. P. Vernon, S. M. Lindsay, and M. B. Stearns, «Brillouin scattering from thermal magnons in a thin Co film», [Physical Review B](#) **29**, 4439 (1984)
- [80] J. Osborn, «Demagnetizing factors of the general ellipsoid», [Physical review](#) **67**, 351 (1945)
- [81] M. B. Stearns, *Landolt-Börnstein New Series III/19a*, Vol. 19a (Springer-Verlag Berlin, 1986)
- [82] H. J. G. Draaisma, F. J. A. den Broeder, and W. J. M. de Jonge, «Perpendicular anisotropy in Pd/Co multilayers», [Journal of Applied Physics](#) **63**, 3479 (1988)
- [83] S. Hashimoto, Y. Ochiai, and K. Aso, «Perpendicular magnetic anisotropy and magnetostriction of sputtered Co/Pd and Co/Pt multilayered films», [Journal of Applied Physics](#) **66**, 4909 (1989)

-
- [84] G. A. Bertero, R. Sinclair, C. Park, and Z. X. Shen, «Interface structure and perpendicular magnetic anisotropy in Pt/Co multilayers», *Journal of Applied Physics* **77**, 3953 (1995)
- [85] D. Sander, «The magnetic anisotropy and spin reorientation of nanostructures and nanoscale films», *Journal of Physics: Condensed Matter* **16**, R603 (2004)
- [86] M. T. Johnson, P. J. H. Bloemen, F. J. A. den Broedery, and J. J. de Vries, «Magnetic anisotropy in metallic multilayers», *Reports on Progress in Physics*. **59**, 1409 (1996)
- [87] L. Néel, «Anisotropie magnétique superficielle et surstructures d'orientation», *Journal de Physique et le Radium* **15**, 225 (1954)
- [88] U. Gradmann and J. Müller, «Flat ferromagnetic, epitaxial 48Ni/52Fe (111) films of few atomic layers», *Physica Status Solidi* **27**, 313 (1968)
- [89] N. Kurti, *Selected Works of Louis Neel: Translations from the first French edition* (CRC Press, 1988)
- [90] P. F. Carcia, «Perpendicular magnetic anisotropy in Pd/Co and Pt/Co thin-film layered structures», *Journal of Applied Physics* **63**, 5066 (1988)
- [91] F. J. A. den Broeder, W. Hoving, and P. J. H. Bloemen, «Magnetic anisotropy of multilayers», *Journal of Magnetism and Magnetic Materials* **93**, 562 (1991)
- [92] F. J. A. den Broeder, D. Kuiper, A. P. van de Mosselaer, and W. Hoving, «Perpendicular magnetic anisotropy of Co-Au multilayers induced by interface sharpening», *Physical Review Letters* **60**, 2769 (1988)
- [93] H. P. Oepen, Y. T. Millev, and J. Kirschner, «The reorientation transition in Co/Au(111)», *Journal of Applied Physics* **81**, 5044 (1997)
- [94] T. Kingetsu, «Molecular-beam-epitaxial growth and magnetic properties of (111) Pt/Co/Ag, Pt/Co, and Ag/Co/Pt superlattices», *Journal of applied physics* **76**, 4267 (1994)
- [95] I. E. Dzialoshinskii, «Thermodynamic theory of "weak" ferromagnetism in antiferromagnetic substances», *Soviet Physics JETP* **5**, 1259 (1957)
- [96] T. Moriya, «Anisotropic superexchange interaction and weak ferromagnetism», *Physical Review* **120**, 91 (1960)
-

References

- [97] I. Dzyaloshinsky, «A thermodynamic theory of “weak” ferromagnetism of antiferromagnetics», *Journal of Physics and Chemistry of Solids* **4**, 241 (1958)
- [98] P. Grünberg, R. Schreiber, Y. Pang, U. Walz, M. B. Brodsky, and H. Sowers, «Layered magnetic structures: Evidence for antiferromagnetic coupling of Fe layers across Cr interlayers», *Journal of Applied Physics* **61**, 3750 (1987)
- [99] C. F. Majkrzak, J. W. Cable, J. Kwo, M. Hong, D. B. McWhan, Y. Yafet, J. V. Waszczak, and C. Vettier, «Observation of a magnetic antiphase domain structure with long-range order in a synthetic Gd-Y superlattice», *Physical Review Letters* **56**, 2700 (1986)
- [100] M. B. Salamon, S. Sinha, J. J. Rhyne, J. E. Cunningham, R. W. Erwin, J. Borchers, and C. P. Flynn, «Long-range incommensurate magnetic order in a Dy-Y multilayer», *Physical Review Letters* **56**, 259 (1986)
- [101] G. Binasch, P. Grünberg, F. Saurenbach, and W. Zinn, «Enhanced magnetoresistance in layered magnetic structures with antiferromagnetic interlayer exchange», *Physical Review B* **39**, 4828 (1989)
- [102] S. Blizak, G. Bihlmayer, S. Blügel, and S. Abaidia, «Interlayer exchange coupling between FeCo and Co ultrathin films through Rh(001) spacers», *Physical Review B* **91**, 014408 (2015)
- [103] M. Stiles, «Interlayer exchange coupling», *Journal of Magnetism and Magnetic Materials* **200**, 322 (1999)
- [104] P. Bruno and C. Chappert, «Oscillatory coupling between ferromagnetic layers separated by a nonmagnetic metal spacer», *Physical Review Letters* **67**, 1602 (1991)
- [105] D. M. Edwards, J. Mathon, R. B. Muniz, and M. S. Phan, «Oscillations of the exchange in magnetic multilayers as an analog of de Haas–van Alphen effect», *Physical Review Letters* **67**, 493 (1991)
- [106] J. R. Cullen and K. B. Hathaway, «A phenomenological theory for the temperature dependence of the antiferromagnetic coupling in thin-film sandwiches and multilayers», *Journal of Applied Physics* **70**, 5879 (1991)

-
- [107] J. Barnaś, «Coupling between two ferromagnetic films through a non-magnetic metallic layer», *Journal of Magnetism and Magnetic Materials* **111**, L215 (1992)
- [108] P. Bruno, «Interlayer exchange coupling: a unified physical picture», *Journal of Magnetism and Magnetic Materials* **121**, 248 (1993), proceedings of the International Symposium on Magnetic Ultrathin Films, Multilayers and Surfaces
- [109] M. D. Stiles, «Exchange coupling in magnetic heterostructures», *Physical Review B* **48**, 7238 (1993)
- [110] M. Stiles, *Interlayer Exchange Coupling*, pp. 99–142 (Springer Berlin Heidelberg, Berlin, Heidelberg, 2005)
- [111] P. Bloemen, H. van Kersteren, H. Swagten, and W. de Jonge, «Oscillatory interlayer exchange coupling in Co/Ru multilayers bilayers», *Phys. Rev. B* **50** (1994)
- [112] M. J. Benitez, A. Hrabec, A. P. Mihai, T. A. Moore, G. Burnell, D. McGrouther, C. H. Marrows, and S. McVitie, «Magnetic microscopy and topological stability of homochiral Néel domain walls in a Pt/Co/AlO_x trilayer», *Nature Communications* **6**, 8957 (2015)
- [113] A. Thiaville, S. Rohart, É. Jué, V. Cros, and A. Fert, «Dynamics of Dzyaloshinskii domain walls in ultrathin magnetic films», *Europhysics Letters* **100**, 57002 (2012)
- [114] M. Heide, G. Bihlmayer, and S. Blügel, «Dzyaloshinskii-Moriya interaction accounting for the orientation of magnetic domains in ultrathin films: Fe/W(110)», *Physical Review B* **78** (2008)
- [115] E. C. Corredor, S. Kuhrau, F. Klodt-Twesten, R. Frömter, and H. P. Oepen, «SEMPA investigation of the Dzyaloshinskii-Moriya interaction in the single, ideally grown Co/Pt(111) interface», *Physical Review B* **96**, 060410(R) (2017)
- [116] F. Klodt-Twesten, S. Kuhrau, H. Oepen, and R. Frömter, «Measuring the Dzyaloshinskii-Moriya interaction of the epitaxial Co/Ir(111) interface.», *Physical Review B* **100**, 100402(R) (2019)

References

- [117] R. Frömter, S. Hankemeier, H. P. Oepen, and J. Kirschner, «Optimizing a low-energy electron diffraction spin-polarization analyzer for imaging of magnetic surface structures», [Review of Scientific Instruments](#) **82**, 033704 (2011)
- [118] S. Hankemeier, *The Magnetic Fine Structure of Thin-Film Elements*, Ph.D. thesis, Universität Hamburg (2010)
- [119] T. VanZandt, R. Browning, and M. Landolt, «Iron overlayer polarization enhancement technique for spin polarized electron microscopy», [Journal of Applied Physics](#) **69**, 1564 (1991)
- [120] A. Gaul, S. Hankemeier, D. Holzinger, N. D. Möglich, P. Staeck, R. Frömter, H. P. Oepen, and A. Ehresmann, «Engineered magnetic domain textures in exchange bias bilayer systems», [Journal of Applied Physics](#) **120**, 033902 (2016)
- [121] J. Lucassen, F. Kloodt-Twesten, R. Frömter, H. P. Oepen, R. A. Duine, H. J. M. Swagten, B. Koopmans, and R. Lavrijsen, «Scanning electron microscopy with polarization analysis for multilayered chiral spin textures», [Applied Physics Letters](#) **111**, 132403 (2017)
- [122] F. Kloodt-Twesten, S. Kuhrau, P. Staeck, D. R. Cavicchia, F. Lofink, H. P. Oepen, and R. Frömter, «Coupling between vortices and antivortices in a cross-tie wall studied by time-resolved SEMPA», [Physical Review B](#) **97**, 024426 (2018)
- [123] F. Lofink, *Oberflächensensitive Abbildung magnetischer Feinstrukturen des Domänenmusters von Ni(111) und geknickter Nanodrähte*, Ph.D. thesis, Universität Hamburg (2014)
- [124] H. P. Oepen, Private Communication
- [125] T. Green, «Beam formation and space charge neutralisation», [IEEE Transactions on Nuclear Science](#) **23** (1976)
- [126] A. A. El-Saftawy, A. Elfalaky, M. S. Ragheb, and S. G. Zakhary, «Investigation of Beam Performance Parameters in a Pierce-Type Electron Gun», [Science and Technology](#) **2**, 191 (2012)
- [127] C. C. Farnell, C. C. Farnell, S. C. Farnell, and J. D. Williams, «Electrostatic Analyzers with Application to Electric Propulsion Testing», in *The 33rd International Electric Propulsion Conference* (2013)

-
- [128] <https://www.photonis.com/sites/default/files/uploads/Products/Channeltron/4822D.gif>
- [129] <https://www.ni.com>
- [130] C. Elliot, V. Vijayakumar, W. Zink, and R. Hansen, «National Instruments LabVIEW: A Programming Environment for Laboratory Automation and Measurement», [SLAS TECHNOLOGY: Translating Life Sciences Innovation](#) **12**, 17 (2007)
- [131] D. A. King and G. Thomas, «Displacive surface phases formed by hydrogen chemisorption on W(001)», [Surface Science](#) **92**, 201 (1980)
- [132] F. Lofink, S. Hankemeier, R. Frömter, J. Kirschner, and H. P. Oepen, «Long-time stability of a low-energy electron diffraction spin polarization analyzer for magnetic imaging», [Review of Scientific Instruments](#) **83**, 023708 (2012)
- [133] R. Cortenraad, S. Ermolov, V. Semenov, A. D. van der Gon, V. Glebovsky, S. Bozhko, and H. Brongersma, «Growth, characterisation and surface cleaning procedures for high-purity tungsten single crystals», [Journal of Crystal Growth](#) **222**, 154 (2001)
- [134] P. Simmons, *Electrical Grounding and Bonding* (Cengage Learning, 2014), 4 edn.
- [135] M. A. Salam and Q. M. Rahman, *Power Systems Grounding* (Springer Singapore, 2016)
- [136] D. Vasilyev, C. Tusche, F. Giebels, H. Gollisch, R. Feder, and J. Kirschner, «Low-energy electron reflection from Au-passivated Ir(001) for application in imaging spin-filters», [Journal of Electron Spectroscopy and Related Phenomena](#) **199**, 10 (2015)
- [137] J. Kirschner, F. Giebels, H. Gollisch, and R. Feder, «Spin-polarized electron scattering from pseudomorphic Au on Ir(001)», [Physical Review B](#) **88** (2013)
- [138] Y.-F. Liew and G.-C. Wang, «High resolution low energy electron diffraction characterization of reconstructed Au(001) surfaces», [Surface Science](#) **227**, 190 (1990)
-

References

- [139] M. Pfeiffer, «Konstruktion eines Au/Ir(001) SPLEED-Detektors für die Rasterelektronenmikroskopie mit Polarisationsanalyse», Universität Hamburg (2017), Bachelor's Thesis
- [140] J. Kirschner, Private Communications
- [141] J. W. Arblaster, «Crystallographic properties of iridium», [Platinum Metals Review](#) **54**, 93 (2010)
- [142] D. Manura, «Simion 8.0 User Manual», Scientific Instrument Services (2008)
- [143] R. Buß, Ph.D. thesis, Universität Hamburg (expected 2021)
- [144] A. N. Bogdanov and D. A. Yablonskii, «Thermodynamically stable "vortices" in magnetically ordered crystals. The mixed state of magnets», [Soviet Physics JETP](#) **68** (1989)
- [145] A. Bogdanov and U. Rößler, «Chiral symmetry breaking in magnetic thin films and multilayers», [Physical review letters](#) **87**, 037203 (2001)
- [146] U. Rößler, A. Bogdanov, and C. Pfeleiderer, «Spontaneous skyrmion ground states in magnetic metals», [Nature](#) **442**, 797 (2006)
- [147] B. Dupé, M. Hoffmann, C. Paillard, and S. Heinze, «Tailoring magnetic skyrmions in ultra-thin transition metal films», [Nature communications](#) **5**, 4030 (2014)
- [148] S. Mühlbauer, B. Binz, F. Jonietz, C. Pfeleiderer, A. Rosch, A. Neubauer, R. Georgii, and P. Böni, «Skyrmion lattice in a chiral magnet», [Science](#) **323**, 915 (2009)
- [149] S. Seki, X. Z. Yu, S. Ishiwata, and Y. Tokura, «Observation of Skyrmions in a Multiferroic Material», [Science](#) **336**, 198 (2012)
- [150] C. Moreau-Luchaire, C. Moutafis, N. Reyren, J. Sampaio, C. A. F. Vaz, N. V. Horne, K. Bouzouhane, K. Garcia, C. Deranlot, P. Warnicke, P. Wohlhüter, J.-M. George, M. Weigand, J. Raabe, V. Cros, and A. Fert, «Additive interfacial chiral interaction in multilayers for stabilization of small individual skyrmions at room temperature», [Nature nanotechnology](#) **11**, 444 (2016)

-
- [151] P.-J. Hsu, A. Kubetzka, A. Finco, N. Romming, K. von Bergmann, and R. Wiesendanger, «Electric-field-driven switching of individual magnetic skyrmions», *Nature nanotechnology* **12**, 123 (2017)
- [152] M. DeJong and K. Livesey, «Domain walls in finite-width nanowires with interfacial Dzyaloshinskii-Moriya interaction», *Physical Review B* **95**, 054424 (2017)
- [153] F. Kloodt-Twesten, Ph.D. thesis, Universität Hamburg (expected 2020)
- [154] A. Soumyanarayanan, M. Raju, A. G. Oyarce, A. K. Tan, M.-Y. Im, A. P. Petrović, P. Ho, K. Khoo, M. Tran, C. Gan *et al.*, «Tunable room-temperature magnetic skyrmions in Ir/Fe/Co/Pt multilayers», *Nature materials* **16**, 898 (2017)
- [155] O. Boulle, J. Vogel, H. Yang, S. Pizzini, D. de Souza Chaves, A. Locatelli, T. O. Menteş, A. Sala, L. D. Buda-Prejbeanu, O. Klein, M. Belmeguenai, Y. Roussigné, A. Stashkevich, S. M. Chérif, L. Aballe, M. Foerster, M. Chshiev, S. Auffret, I. M. Miron, and G. Gaudin, «Room-temperature chiral magnetic skyrmions in ultrathin magnetic nanostructures», *Nature Nanotechnology* **11**, 449 (2016)
- [156] S. Woo, K. Litzius, B. Krüger, M.-Y. Im, L. Caretta, K. Richter, M. Mann, A. Krone, R. M. Reeve, M. Weigand, P. Agrawal, I. Lemesh, M.-A. Mawass, P. Fischer, M. Kläui, and G. S. D. Beach, «Observation of room-temperature magnetic skyrmions and their current-driven dynamics in ultrathin metallic ferromagnets», *Nature Materials* **15**, 501 (2016)
- [157] W. Jiang, X. Zhang, G. Yu, W. Zhang, X. Wang, M. B. Jungfleisch, J. E. Pearson, X. Cheng, O. Heinonen, K. L. Wang, Y. Zhou, A. Hoffmann, and S. G. E. te Velthuis, «Direct observation of the skyrmion Hall effect», *Nature Nanotechnology* **11**, 449 (2016)
- [158] H. Yang, A. Thiaville, S. Rohart, A. Fert, and M. Chshiev, «Anatomy of Dzyaloshinskii-Moriya Interaction at Co/Pt Interfaces», *Physical Review Letters* **115** (2015)
- [159] G. J. Vida, E. Simon, L. Rózsa, K. Palotás, and L. Szunyogh, «Domain-wall profiles in Co/Ir_n/Pt(111) ultrathin films: Influence of the Dzyaloshinskii-Moriya interaction», *Physical Review B* **94**, 214422 (2016)
-

References

- [160] F. Freimuth, S. Blügel, and Y. Mokrousov, «Berry phase theory of Dzyaloshinskii–Moriya interaction and spin–orbit torques», *Journal of physics: Condensed matter* **26**, 104202 (2014)
- [161] H. Yang, A. Thiaville, S. Rohart, A. Fert, and M. Chshiev, «Erratum: Anatomy of Dzyaloshinskii-Moriya Interaction at Co/Pt Interfaces», *Physical Review Letters* **118**, 219901 (2017)
- [162] A. Hrabec, N. A. Porter, A. Wells, M. J. Benitez, G. Burnell, S. McVitie, D. McGrouther, T. A. Moore, and C. H. Marrows, «Measuring and tailoring the Dzyaloshinskii-Moriya interaction in perpendicularly magnetized thin films», *Physical Review B* **90** (2014)
- [163] M. Bacani, M. A. Marioni, J. Schwenk, and H. J. Hug, «How to measure the local Dzyaloshinskii-Moriya interaction in skyrmion thin-film multilayers», *Scientific Reports* **9** (2016)
- [164] A. W. J. Wells, P. M. Shepley, C. H. Marrows, and T. A. Moore, «Effect of interfacial intermixing on the Dzyaloshinskii-Moriya interaction in Pt/Co/Pt», *Physical Review B* **95**, 054428 (2017)
- [165] D.-S. Han, N.-H. Kim, J.-S. Kim, Y. Yin, J.-W. Koo, J. Cho, S. Lee, M. Kläui, H. J. M. Swagten, B. Koopmans, and C.-Y. You, «Asymmetric hysteresis for probing Dzyaloshinskii-Moriya interaction», *Nano Letters* **16**, 4438 (2016)
- [166] R. Lavrijsen, D. M. F. Hartmann, A. van den Brink, Y. Yin, B. Barcones, R. A. Duine, M. A. Verheijen, H. J. M. Swagten, and B. Koopmans, «Asymmetric magnetic bubble expansion under in-plane field in Pt/Co/Pt: Effect of interface engineering», *Physical Review B* **91**, 104414 (2015)
- [167] B. Zimmermann, W. Legrand, D. Maccariello, N. Reyren, V. Cros, S. Blügel, and A. Fert, «Dzyaloshinskii-Moriya interaction at disordered interfaces from ab initio theory: Robustness against intermixing and tunability through dusting», *Applied Physics Letters* **113**, 232403 (2018)
- [168] H. Yang, O. Boulle, V. Cros, A. Fert, and M. Chshiev, «Controlling Dzyaloshinskii-Moriya Interaction via chirality dependent atomic-layer stacking, insulator capping and electric field», *Scientific reports* **8** (2018)
- [169] A. Finco, M. Perini, A. Kubetzka, K. von Bergmann, and R. Wiesendanger, «Magnetic domain walls in strain-patterned ultrathin films», *Physical Review B* **98**, 174435 (2018)

-
- [170] W. Haynes (Ed.), *Handbook of Chemistry and Physics* (CRC Press, 2011), 92 edn.
- [171] R. Tran, Z. Xu, B. Radhakrishnan, D. Winston, W. Sun, K. A. Persson, and S. P. Ong, «Surface energies of elemental crystals», *Scientific Data* **3**, 160080 (2016)
- [172] <http://crystalium.materialsvirtuallab.org/>
- [173] E. Lundgren, B. Stanka, M. Schmid, and P. Varga, «Thin films of Co on Pt(111): Strain relaxation and growth», *Physical Review B* **62**, 2843 (2000)
- [174] D. Drouin, A. Couture, D. Joly, X. Tastet, V. Aimez, and R. Gauvin, «CASINO V2.42 — A Fast and Easy-to-use Modeling Tool for Scanning Electron Microscopy and Microanalysis Users», *Scanning* **29**, 92 (2007)
- [175] J. Tsay and C. Shern, «Structure evolution for annealing Co ultrathin films on Pt(111)», *Surface Science* **396**, 313 (1998)
- [176] P. Grütter and U. T. Dürig, «Growth of vapor-deposited cobalt films on Pt(111) studied by scanning tunneling microscopy», *Physical Review B* **49**, 2021 (1994)
- [177] M. Perini, *Nanoscale non-collinear magnetic structures in Co-based epitaxial ultrathin films*, Ph.D. thesis, Universität Hamburg (2019)
- [178] R. Bodenberger and A. Hubert, «Zur Bestimmung der Blochwandenergie von einachsigen Ferromagneten», *physica status solidi (a)* **44**, K7 (1977)
- [179] K. Bagschik, R. Frömter, J. Bach, B. Beyersdorff, L. Müller, S. Schleiter, M. H. Bernsten, C. Weier, R. Adam, J. Viefhaus, C. M. Schneider, G. Grübel, and H. P. Oepen, «Employing soft x-ray resonant magnetic scattering to study domain sizes and anisotropy in Co/Pd multilayers», *Physical Review B* **94**, 134413 (2016)
- [180] B. Kaplan and G. Gehring, «The domain structure in ultrathin magnetic films», *JMMM* **128**, 111 (1993)
- [181] H. J. G. Draaisma and W. J. M. de Jonge, «Magnetization curves of Pd/Co multilayers with perpendicular anisotropy», *Journal of Applied Physics* **62**, 3318 (1987)
-

References

- [182] I. Lemesh, F. Büttner, and G. S. D. Beach, «Accurate model of the stripe domain phase of perpendicularly magnetized multilayers», [Physical Review B](#) **95**, 174423 (2017)
- [183] Y. Millev, «Bose-Einstein integrals and domain morphology in ultrathin ferromagnetic films with perpendicular magnetization», [Journal of Physics: Condensed Matter](#) **8**, 3671 (1996)
- [184] O. Hellwig, G. Denbeaux, J. Kortright, and E. E. Fullerton, «X-ray studies of aligned magnetic stripe domains in perpendicular multilayers», [Physica B: Condensed Matter](#) **336**, 136 (2003), proceedings of the Seventh International Conference on Surface X-ray and Neutron Scattering
- [185] S. Tarasenko, A. Stankiewicz, V. Tarasenko, and J. Ferré, «Bloch wall dynamics in ultrathin ferromagnetic films», [Journal of Magnetism and Magnetic Materials](#) **189**, 19 (1998)
- [186] N. W. E. McGee, M. T. Johnson, J. J. de Vries, and J. aan de Stegge, «Localized Kerr study of the magnetic properties of an ultrathin epitaxial Co wedge grown on Pt(111)», [Journal of Applied Physics](#) **73**, 3418 (1993)
- [187] T. Suzuki, D. Weller, C.-A. Chang, R. Savoy, T. Huang, B. Gurney, and V. Speriosu, «Magnetic and magneto-optic properties of thick face-centered-cubic Co single-crystal films», [Applied Physics Letters](#) **64**, 2736 (1994)
- [188] D. Paige, B. Szpunar, and B. Tanner, «The magnetocrystalline anisotropy of cobalt», [Journal of Magnetism and magnetic Materials](#) **44**, 239 (1984)
- [189] D. Stickler, R. Frömter, H. Stillrich, C. Menk, H. P. Oepen, C. Gutt, S. Streit-Nierobisch, L.-M. Stadler, G. Grübel, C. Tieg *et al.*, «Domain size in systems with canted magnetization», [Physical Review B](#) **84**, 104412 (2011)
- [190] B. Miao, Y. Millev, L. Sun, B. You, W. Zhang, and H. Ding, «Thickness-driven spin reorientation transition in ultrathin films», [Science China Physics, Mechanics and Astronomy](#) **56**, 70 (2013)
- [191] M. Belmeguenai, J.-P. Adam, Y. Roussigné, S. Eimer, T. Devolder, J.-V. Kim, S. M. Cherif, A. Stashkevich, , and A. Thiaville, «Interfacial Dzyaloshinskii-Moriya interaction in perpendicularly magnetized

- Pt/Co/AlO_x ultrathin films measured by Brillouin light spectroscopy», *Physical Review B (R)* **91**, 180405 (2015)
- [192] S. Rohart and A. Thiaville, «Skyrmion confinement in ultrathin film nanostructures in the presence of Dzyaloshinskii-Moriya interaction», *Physical Review B* **88**, 184422 (2013)
- [193] S. Meckler, N. Mikuszeit, A. Preßler, E. Y. Vedmedenko, O. Pietzsch, and R. Wiesendanger, «Real-Space Observation of a Right-Rotating Inhomogeneous Cycloidal Spin Spiral by Spin-Polarized Scanning Tunneling Microscopy in a Triple Axes Vector Magnet», *Physical Review Letters* **103**, 157201 (2009)
- [194] W. P. Davey, «Precision measurements of the lattice constants of twelve common metals», *Physical Review* **25**, 753 (1925)
- [195] M. Speckmann, H. Oepen, and H. Ibach, «Magnetic Domain Structures in Ultrathin Co/Au(111): On the influence of Film Morphology», *Physical Review Letters* **75** (1995)
- [196] S. Kuhrau, F. Kloodt-Twesten, C. Heyn, H. P. Oepen, and R. Frömter, «Cap-layer-dependent oxidation of ultrathin cobalt films and its effect on the magnetic contrast in scanning electron microscopy with polarization analysis», *Applied Physics Letters* **113**, 172403 (2018)
- [197] G. Winkler, *Korrelation zwischen Strukturellen und magnetogalvanischen Eigenschaften von Pt/Co/Pt- und Pd/Co/Pd-Schichtsystemen*, Ph.D. thesis, Universität Hamburg (2015)
- [198] A. Kobs, *Magnetogalvanic effects in ferromagnets of reduced dimensions*, Ph.D. thesis, Universität Hamburg (2013)
- [199] É. Trémolet de Lacheisserie, M. Schlenker, and D. Gignoux, *Magnetism*, chap. Magnetic thin films and multilayers, pp. 255–304 (Springer, 2005)
- [200] H. Stillrich, C. Menk, R. Frömter, and H. P. Oepen, «Magnetic anisotropy and spin reorientation in Co/Pt multilayers: Influence of preparation», *Journal of Magnetism and Magnetic Materials* **322**, 1353 (2010)
- [201] M. Wellhöfer, M. Weißenborn, R. Anton, S. Pütter, and H. P. Oepen, «Morphology and magnetic properties of ECR ion beam sputtered Co/Pt films», *Journal of Magnetism and Magnetic Materials* **292**, 345 (2005)

References

- [202] G. Winkler, A. Kobs, A. Chuvilin, D. Lott, A. Schreyer, and H. P. Oepen, «On the variation of magnetic anisotropy in Co/Pt(111) on silicon oxide», *Journal of Applied Physics* **117**, 105306 (2015)
- [203] L. G. Parratt, «Surface Studies of Solids by Total Reflection of X-Rays», *Physical Review* **95**, 359 (1954)
- [204] K. N. Stoev and K. Sakurai, «Review on grazing incidence X-ray spectrometry and reflectometry», *Spectrochimica Acta Part B* **54**, 41 (1999)
- [205] J. Daillant and A. G. (Eds.), *X-ray and Neutron Reflectivity: Principles and Applications*, Vol. Lect. Notes Phys. 770 (Springer-Verlag Berlin Heidelberg, 2009)
- [206] A. Nelson, «Co-refinement of multiple-contrast neutron/X-ray reflectivity data using MOTOFIT», *Journal of Applied Crystallography* **39**, 273 (2006)
- [207] <https://www.wavemetrics.com/>
- [208] F. Abeles, «La théorie générale des couches minces», *Journal de Physique et Le Radium* **11**, 307 (1950)
- [209] H. Kiessig, «Interferenz von Röntgenstrahlen an dünnen Schichten», *Annalen der Physik* **402**, 769 (1931)
- [210] http://henke.lbl.gov/optical_constants/atten2.html
- [211] A. E. Ennos, «The origin of specimen contamination in the electron microscope», *British Journal of Applied Physics* **4**, 101 (1953)
- [212] J. Hren, *Principles of Analytical Electron Microscopy*, chap. 10: Barriers to AEM: Contamination and Etching (Springer, Boston, MA, 1986)
- [213] G. Schönhense and H. Siegmann, «Transmission of electrons through ferromagnetic material and applications to detection of electron spin polarization», *Annalen der Physik* **2**, 465 (1993)
- [214] J. Kerr, «On rotation of the plane of polarization by reflection from the pole of a magnet», *The London, Edinburgh, and Dublin Philosophical Magazine and Journal of Science* **3**, 321 (1877)
- [215] P. Weinberger, «John Kerr and his effects found in 1877 and 1878», *Philosophical Magazine Letters* **88**, 897 (2008)

- [216] B. El-Kareh, *Fundamentals of Semiconductor Processing Technologies* (Springer US, 1995)
- [217] H. G. Tompkins and J. A. Augis, «The oxidation of cobalt in air from room temperature to 467°C», *Oxidation of Metals* **16**, 355 (1981)
- [218] H. S. Hsu and G. J. Yurek, «Kinetics and mechanisms of the oxidation of cobalt at 600–800°C», *Oxidation of Metals* **17**, 55 (1982)
- [219] M. Getzlaff, J. Bansmann, and G. Schönhense, «Magnetic interactions in different oxidation states of thin cobalt films», *Journal of Magnetism and Magnetic Materials*. **131**, 304 (1994)
- [220] W. Clemens, E. Vescovo, T. Kachel, C. Carbone, and W. Eberhardt, «Spin-resolved photoemission study of the reaction of O₂ with fcc Co(100)», *Physical Review B* **46**, 4198 (1992)
- [221] T. Takada, Y. Bando, M. Kiyama, and H. Miyamoto, «The magnetic property of β -Co(OH)₂», *Journal of the Physical Society of Japan* **21**, 2726 (1996)
- [222] L. Smardz, U. Köbler, and W. Zinn, «Oxidation kinetics of thin and ultra-thin cobalt films», *Journal of Applied Physics* **71**, 5199 (1992)
- [223] A. Atrei, U. Bardi, G. Rovida, M. Torrini, E. Zanazzi, and M. Maglietta, «EELFS study of oxygen chemisorption on cobalt», *Surface Science* **189/190**, 459 (1987)
- [224] M. Hille, *Magnetotransport-Untersuchungen in Co/Pt-Drähten unter Berücksichtigung der Domänenstruktur*, Ph.D. thesis, Universität Hamburg (2013)

Acknowledgements

Within my time as a PhD student, I got support from several people who contributed in various ways to the completion of this thesis. I owe them my gratitude, in particular I would like to thank:

- Prof. Hans Peter Oepen for the continuous support of my PhD study, sharing his knowledge about the OOP SEMPA setup and experience in handling technical issues which arose during the process of bringing the setup back to operation, as well as the inquiring discussions on experimental results.
- Prof. Ralf Röhlberger for refereeing this thesis as a second assessor.
- Robert Frömter for the general supervision of the thesis, support and aid in terms of technical issues in the lab, fruitful scientific discussions and brainstorming sessions as well as proof reading of this manuscript.
- Fabian Kloodt-Twesten for the multitudinous shared hours in the SEMPA labs, sharing his experimental and theoretical knowledge on SEMPA and magnetism, the support in LabView associated issues, countless discussion on scientific and non-scientific topics as well as proof reading of this thesis.
- Edna Corredor Vega for the joint work in the lab and lending a helping hand while fixing parts of the OOP SEMPA.
- Maurice Pfeiffer for implementing the idea of the new spin detector into CAD and his reliable assistance/ lending a hand while setting up new parts at the OOP SEMPA chamber.
- Jochen Wagner for the discussions on the antiferromagnetically coupled Pt/Co/Ir sputter systems and MOKE measurements.
- Sonja Hesselmann for the general organization of the lab infrastructure of our group and for helping me preparing the sputtered Pt/Co/Ir samples.
- Horst Biedermann and Michael Brand of the electronics workshop for the aid during the first years when the OOP SEMPA was brought back to op-

- eration. I highly appreciated their open door policy and their engagement.
- Jens Path and Tim Erke of the mechanical workshop for the constructive discussions on realization possibilities for reconstruction works at the OOP SEMPA and the new spin detector.
 - Prof. Roland Wiesendanger for his leading work in respect to the SFB 668 as well as supporting my application for a scholarship. Additionally, I would like to thank Andrea Beese for the reliable execution of administrative duties as well as her constructive aid with bureaucratic issues.
 - Andre Kubetzka und Kirsten von Bergmann for the fruitful discussions and sharing their knowlege on the Co/Pt(111) and the Au/Ir(001) system.
 - Christian Heyn for the AFM measurements on the Pt/Co/Ir samples.
 - Gerd Neuber for the support during ellipsometry measurements.
 - Jonathan Jacobson for teaching me how to perform XRR measurements and his years of work on the sputter chamber.
 - Dieter Lott for the technical support during the XRR measurements.
 - Eva-Sophie Wilhelm, Stephan Freercks and Ralph Buß for general scientific discussions on magnetism and aid with everyday lab problems.
 - Brigitte Muhlack and Stephanie Baer for the organization of financial and bureaucratic issues for our work group.
 - Torben Steenbock for the organization of meetings of the PhD students of the SFB 668.
 - All previous members of the work group G.
 - My friends and family for their support over the years of studying.

Publications

Publication List

[P1] F. Kloodt-Twesten, S. Kuhrau, H.P. Oepen, and R. Frömter. "*Measuring the Dzyaloshinskii-Moriya interaction of the epitaxial Co/Ir(111) interface*". submitted (2019)

[P2] R. Frömter, E.C. Corredor, S. Hankemeier, F. Kloodt-Twesten, S. Kuhrau, F. Lofink, S. Rößler, and H.P. Oepen. "*Imaging the interaction of electrical currents with magnetization distributions*" in "Atomic- and Nanoscale Magnetism" ed. R. Wiesendanger, pp 343-358, Springer, Cham (2018)

[P3] S. Kuhrau, F. Kloodt-Twesten, C. Heyn, H.P. Oepen, and R. Frömter. "*Cap-layer-dependent oxidation of ultrathin cobalt films and its effect on the magnetic contrast in scanning electron microscopy with polarization analysis*". Applied Physics Letters **113**, 172403 (2018)

[P4] F. Kloodt-Twesten, S. Kuhrau, P. Staeck, D.R. Cavicchia, F. Lofink, H.P. Oepen, and R. Frömter. "*Coupling between vortices and antivortices in a cross-tie wall studied by time-resolved SEMPA*". Physical Review B **97**, 024426 (2018)

[P5] E.C. Corredor, S. Kuhrau, F. Kloodt-Twesten, R. Frömter, and H.P. Oepen. "*SEMPA investigation of the Dzyaloshinskii-Moriya interaction in the single, ideally grown Co/Pt(111) interface*". Physical Review B **96**, 060410(R) (2017)

Conference Submissions

Speaker marked with ●

[C1] ●R. Frömter, E.C. Corredor, S. Kuhrau, F. Kloodt-Twesten, H.P. Oepen. "*SEMPA investigation of the Dzyaloshinskii-Moriya interaction in the single, ideally grown Co/Pt(111) interface*". 9th Joint European Magnetic Symposia, Mainz, Germany (2018)

[C2] S. Kuhrau, F. Kloodt-Twesten, C. Heyn, ●R. Frömter, P. Staeck, H.P. Oepen. "*Scanning electron microscopy with polarization analysis on ex-situ sputter-deposited ultrathin Ir/Co/Pt films*". 9th Joint European Magnetic Symposia, Mainz, Germany (2018)

[C3] F. Kloodt-Twesten, S. Kuhrau, R. Frömter and •H. P. Oepen. "*Lateral and Temporal High-resolution Scanning Electron Microscopy with Polarization Analysis*". 5th International Conference of Asian Union of Magnetics Societies, Jeju, Korea (2018).

[C4] •S. Kuhrau, F. Kloodt-Twesten, J. Wagner, R. Frömter, H.P. Oepen. "*Scanning electron microscopy with polarization analysis on ex-situ sputter-deposited ultrathin Ir/Co/Pt films*". Springmeeting of the German Physical Society DPG, Berlin, Germany (2018)

[C5] •F. Kloodt-Twesten, S. Kuhrau, P. Staeck, H. P. Oepen and R. Frömter. "*Coupling between vortices and antivortices in a cross-tie wall studied by time-resolved SEMPA*". Springmeeting of the German Physical Society DPG, Berlin, Germany (2018).

[C6] •S. Kuhrau, E.C. Corredor, F. Kloodt-Twesten, R. Frömter, H.P. Oepen. "*SEMPA investigation of the Dzyaloshinskii-Moriya interaction in the single, ideally grown Co/Pt(111) interface*". Springmeeting of the German Physical Society DPG, Berlin, Germany (2018)

[C7] •F. Kloodt-Twesten, R. Frömter, P. Staeck, S. Kuhrau, H.P. Oepen. "*Coupled Vortex-Antivortex Oscillation Studied by Time-Resolved Scanning Electron Microscopy with Polarization Analysis*". Intermag Conference, Dublin, Ireland (2017)

[C8] •F. Kloodt, R. Frömter, P. Staeck, A. Frauen, S. Kuhrau, and H. P. Oepen. "*Time-resolved scanning electron microscopy with polarization analysis*", Springmeeting of the German Physical Society DPG, Dresden, Germany (2017)

[C9] •F. Kloodt, R. Frömter, P. Staeck, S. Kuhrau, and H. P. Oepen. "*Coupled vortex-antivortex oscillation studied by Time-resolved Scanning Electron Microscopy with Polarization Analysis*", Springmeeting of the German Physical Society DPG, Dresden, Germany (2017)

[C10] •F. Kloodt, R. Frömter, P. Staeck, S. Kuhrau, and H. P. Oepen. "*Dynamics of coupled topological Solitons*", Springmeeting of the German Physical Society DPG, Dresden, Germany (2017)

Publications

[C11] E.C. Corredor, • S. Kuhrau, F. Kloodt, R. Frömter, H.P. Oepen. "*Anticlockwise Néel domain walls in ultrathin cobalt films on Pt(111)*". Springmeeting of the German Physical Society DPG, Dresden, Germany (2017)

[C12] F. Kloodt, • R. Frömter, S. Kuhrau, P. Staeck, and H.P. Oepen. "*Coupled vortex gyration in the diamond state, studied by Time-Resolved Scanning Electron Microscopy with Polarization Analysis*". 61st Annual Conference on Magnetism and Magnetic Materials, New Orleans, USA (2016)

[C13] F. Kloodt, • R. Frömter, S. Kuhrau, P. Staeck, and H.P. Oepen. "*Coupled vortex gyration in the diamond state studied by Time-Resolved Scanning Electron Microscopy with Polarization Analysis*". 9th International Symposium on Metallic Multilayers, Uppsala, Sweden (2016)

[C14] • F. Kloodt, R. Frömter, S. Kuhrau, P. Staeck und H. P. Oepen. "*Incorporating Nanosecond Time Resolution into Scanning Electron Microscopy with Polarization Analysis*", Springmeeting of the German Physical Society DPG, Regensburg, Germany (2016)

Eidesstattliche Erklärung/ Declaration of oath

Hiermit versichere ich an Eides statt, die vorliegende Dissertationsschrift selbst verfasst und keine anderen als die angegebenen Hilfsmittel und Quellen benutzt zu haben. Die eingereichte schriftliche Fassung entspricht der auf dem elektronischen Speichermedium. Die Dissertation wurde in der vorgelegten oder einer ähnlichen Form nicht schon einmal in einem früheren Promotionsverfahren angenommen oder als ungenügend beurteilt.

I hereby declare on oath that I have written the present dissertation myself and that I have not used any other than the acknowledged resources and aids. The submitted written version of the thesis is identical to the one on the electronic storage medium. This thesis has previously neither in the same nor in a similar form been accepted in another doctorate procedure or has been graded as inadequate.

Unterschrift/Signature

Datum/Date

Ort/Place